Seismic modelling of the stratigraphic architecture of syn-rift deep-water channel complexes in the Corinth Rift, Greece

Master Thesis in Earth Science

Ina Tårup

Department of Earth Science

University of Bergen

July, 2022

Acknowledgements

This thesis is the project part of my MSc degree in Earth Science, carried out in the Geodynamics and Basin Studies research group at the Department of Earth Science, University of Bergen, as a contribution to the DeepRift project led by UiB.

There are several people and contributors I would like to show my greatest gratitude to for making this thesis possible. Firstly, my main supervisor Robert Gawthorpe (UiB) is thanked for developing the original project for the thesis, and for valuable guidance. A special thanks to co-supervisors Martin Muravchik (UiB), Tim Cullen (UiB) and Isabelle Lecomte (UiB), for great assistance throughout all stages of the project, and for good discussions and valuable, constructive feedback.

This project could not have been completed without the integrated deployment of several software tools. NORCE is thanked for the academic license of the software LIME; NORSAR Innovation AS is thanked for the academic use of SeisRoX part of the NORSAR Software Suite. MathWorks is thanked for the academic license to MATLAB.

Additionally, Leo Zijerveld is thanked for technical support in the lab, and Simon Buckley (NORCE) is thanked for great assistance with panel projections in LIME. I also wish to express great gratitude to Sanne Lorentzen for proof-reading the thesis and providing valuable feedback.

To all my fellow students at GEO, thank you for making the past five years so memorable. Finally, I wish to express special gratitude toward my friends and family for always being supportive and believing in me.

Ina Tårup
Bergen, June 2022

Abstract

Deep-water systems in rift basins lack extensive research because they tend to be buried in the subsurface making them hard to study directly. Rare, exhumed deep-water syn-rift depositional systems can therefore provide valuable insight into their stratigraphic architecture. Understanding the evolution, stratigraphic architecture and geometries of syn-rift deep-water deposits is valuable knowledge regarding energy resources, CO_2 sequestration as well as understanding past climate, environmental and tectonic change. As syn-rift deep-water deposits in the subsurface are typically studied using seismic reflection data, generating synthetic seismic images based on outcrop analogues is a good way of gaining more knowledge about the detectability and imaging of such deposits. In this study, a 2D Point-Spread Function (PSF) based convolution modelling approach was applied to generate synthetic seismic images of syn-rift deep-water channel complexes in the Corinth Rift, based on geological models created from virtual outcrop models and cross-sections. The study further analyses the impact of variable geophysical parameters, such as the dominant frequency, maximum illumination angle, incident angle and level of noise. The resulting 2D seismic images revealed that stratigraphic architecture and rock body geometries can be detected at different scales dependent on the input parameters of the seismic modelling, and reflectivity is dependent on dominant lithologies and complexity of the stratigraphic architecture. The lateral and vertical resolution and seismic detectability is most impacted by dominant frequencies, illumination, and noise levels. The resultant synthetic seismic images simulating conventional seismic images showed that on a general basis, syn-rift deep-water channel complexes can be detected, but individual channel forms and stratigraphic architecture may fall under seismic resolution or only produce subtle amplitude variabilities and can therefore not always be resolved.

Contents

Nomenclature:

AI - Acoustic impedance

Vp - Compressional Wave Velocity

Vs - Shear Wave Velocity

ISR - Illumination Vector

PSF - Point-Spread Function

SR - Source-Receiver

FT - Fourier Transformation

PSDM - Prestack Depth Migration

RB - Ray Based

FW - Full Wavefield

RHO – Density

MD - Measured Depth

MIA – Maximum Illumination Angle

f – Frequency

VOM – Virtual Outcrop Model

RDF – Rethi-Dendro Formation

θ – Incident angle

1. Introduction

1.1 Rationale

Deep-water depositional systems are some of the largest on earth and are responsible for transportation of significant sediment volumes toward the basin floor. Processes like sediment gravity flows have created some of the greatest sediment accumulations on the planet, and these deposits can comprise large oil and gas reservoirs (Talling et al. 2012). However, deep-water systems in rift basins are noted typically to be smaller, coarser grained, and more complex in their interactions with tectonics and climate than deep-water systems on passive margins (e.g. Strachan et al., 2013). Understanding the evolution, stratigraphic architecture and geometries of the deposits is valuable knowledge regarding energy resources, CO_2 sequestration as well as understanding past climate, environmental and tectonic change.

Syn-rift deep-water systems lack extensive research because they tend to be buried in the subsurface making them hard to study directly. The Corinth Rift, Greece represents one of the few places in the world where syn-rift deep-water deposits are exposed on the surface, providing opportunities to study the original geometries and stratigraphic architectures of deep-water deposits. The Rethi-Dendro Formation (RDF) represents the Plio-Pleistocene sub-lacustrine part of the syn-rift succession of the Corinth Rift, which is well exposed in outcrops in several locations due to tilted and uplifted fault blocks (Gawthorpe et al., 2018). This includes the Stylia outcrop, which comprises a coarse-grained channel complex in a syn-rift deep-water setting.

As syn-rift deep-water deposits in the subsurface are typically studied using seismic reflection data, generating synthetic seismic sections based on outcrop analogues is a good way of gaining more knowledge about the seismic expression, detectability and imaging of such deposits (Rabbel et al., 2018). Sensitivity testing of variable geophysical parameters and their impact on synthetic seismic images allows for greater understanding of different seismic stratigraphic techniques which can be used to investigate stratigraphic architecture, and the impact of natural variability of seismic signature in resolving stratigraphic heterogeneity.

1.2 Aims and objectives

This study aims to improve the understanding of the seismic signature of syn-rift deep-water deposits with a focus on stratigraphic architecture and rock body geometries and investigate the impact of geophysical parameters on seismic images of deep-water channel complexes. The following objectives were set to achieve these aims:

1. Construct a 3D virtual outcrop model (VOM) of the Stylia outcrop and develop a realistic geological model encompassing stratigraphic architecture and rock body geometries based on geological interpretation of the VOM.

2. Use 2D Point Spread Function (PSF) based convolution modelling approach to generate synthetic seismic images of the Stylia outcrop model and regional cross-sections from the Corinth Rift calibrated with elastic properties derived from suitable subsurface analogues.

3. Perform a sensitivity analysis to investigate the impact of geophysical parameters on seismic images of syn-rift deep-water deposits. Parameters considered in this study include the dominant frequency, maximum illumination angle, incident angle and level of noise. Geological variations and variations of elastic properties from two different wells will also be investigated.

4. Compare the synthetic seismic images and results of the sensitivity analyses to other seismic modelling case studies and subsurface conventional and high-frequency studies of similar geological settings.

2. Geological setting

2.1 The Corinth Rift

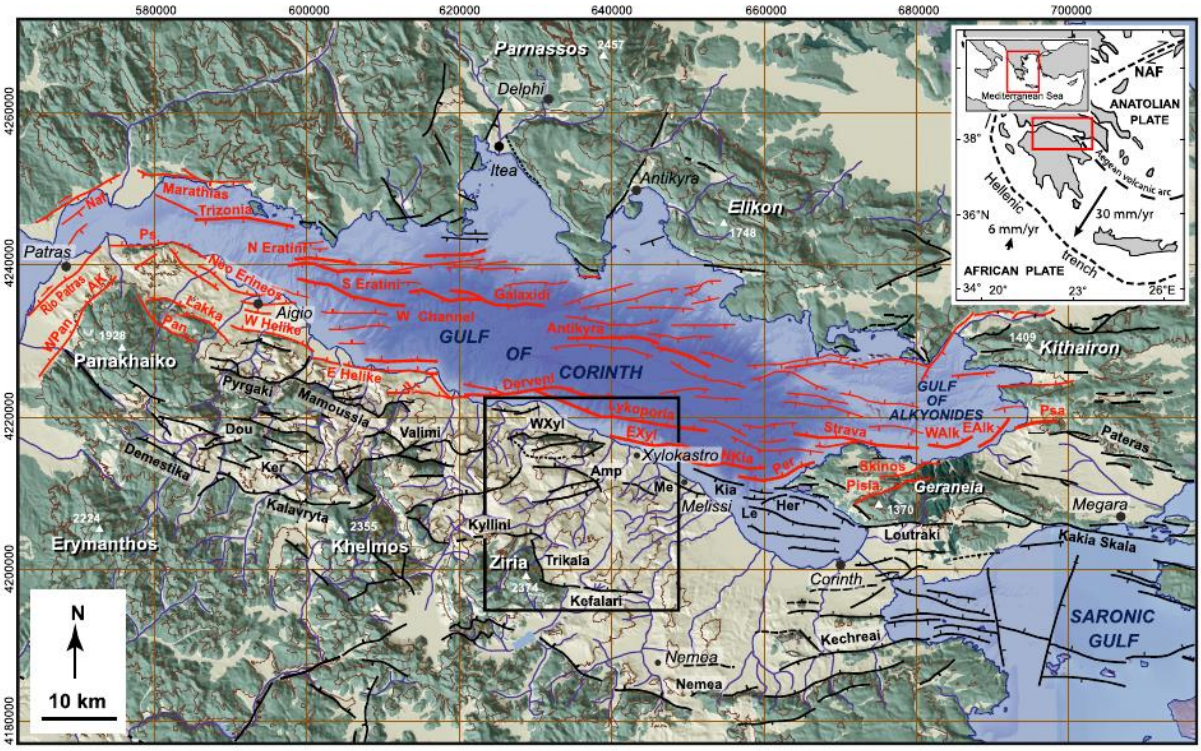

Figure 2.1: Topography and geology of the Corinth Rift. Study area of the central southern margin is marked on the map with a black square. Green areas correspond to pre-rift Hellenide Basement and tan areas correspond to Plio-Pleistocene syn-rift sediments. Red lines represent active normal faults, and black lines represent inactive normal faults. Modified from Gawthorpe et al. (2018).

Regional tectonic framework

The Gulf of Corinth is an approximately 120 km long and maximum 30 km wide zone of N-S extension and active rifting, situated between the North Anatolian fault to the north and the Hellenic trench to the south (fig. 2.1) (Muravchik et al., 2020, Gawthorpe et al., 2018, Cullen et al., 2020, Nixon et al., 2016). Based on radiometric dating, rifting began ~5 Ma in late-Pliocene, early Pleistocene, initiating as a result of back-arc extension related to the Hellenic subduction zone where subduction of the African plate under the Anatolian plate occurred (Leeder et al., 2008, Collier and Dart, 1991). The history of rift activity can be divided into two main phases of active rifting (Collier and Dart, 1991, Ford et al., 2013, Gawthorpe et al., 2018, Leeder et al., 2008). Rift 1 lasted from 5.0-3.5 to 2.2-1.8 Ma and comprised a 30 km wide zone of normal faulting located on the northern Peloponnese. Initial deposits from Rift 1 are characterized by fluvial and shallow lacustrine environments, but by 3.6 Ma, deepening of the

environment resulted in the development of a central "Lake Corinth" over most of the rift (Gawthorpe et al., 2018). Phase 2 initiated 2.2-1.8 Ma and is associated with a northward shift in fault activity, resulted in uplift and erosion of Rift 1 fault blocks (Ford et al., 2013). Phase 2 rifting is active to this day, with major normal faulting along E-W striking and N-dipping faults along southern Gulf of Corinth (Gawthorpe et al., 2018).

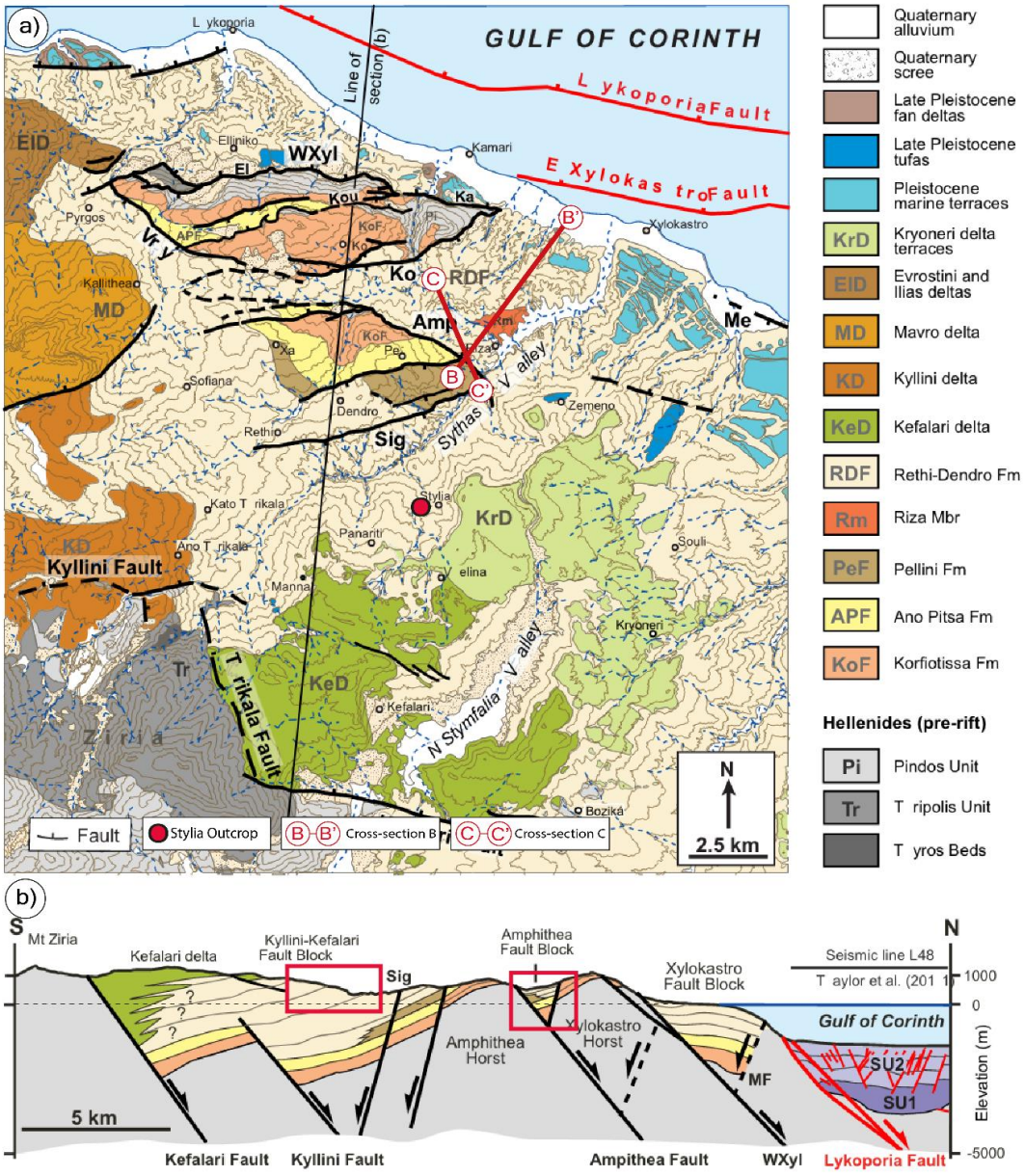

Figure 2.2: a) Geological map of the central southern margin, with the location of the Stylia Outcrop and regional cross-sections marked on the map. b) S-N cross-section of the study area. Fault abbreviations: Amp, Amphithea fault; Ko, Koutsa fault; Me, Melissi fault; Sig, Sigeritsa fault; Vry, Vryssoules fault; WXyl, West-Xylokastro fault. Modified from Gawthorpe et al. (2018)

Structural configuration and lithostratigraphy of the central southern margin

The area of interest for this thesis is located on the central southern margin of the Corinth Rift in exposures south of the town of Xylokastro (figures 2.1 and 2.2). The central southern margin reflects the early Rift Phase 1 through its structural configuration and lithostratigraphy. The Corinth rift is separated from the northern Peloponnesus Hellenic basement by a linkage of three E-W to NW-SE striking faults, i.e., Kyllini, Trikala and Kefalari faults (fig 2.2) (Gawthorpe et al., 2018). Further north, the onshore southern margin of the Gulf of Corinth consists of a series of tilted fault blocks, containing deposits of Rift Phase 1. The main normal faults bounding the fault blocks include the Amphithea and West-Xylokastro faults (fig 2.2). The >3 km thick syn-rift succession deposited in the fault blocks is divided by Gawthorpe et al. (2018) into four lithostratigraphic formations representing an overall upward deepening succession (fig 2.2), from the fluvial Korfiotissa formation, into the palustrine Ano Pitsa formation and lower slope to pro-delta Pellini formation, and finally into the deep-lacustrine Rethi-Dendro formation. These deposits are unconformably overlain by Late Quaternary deltaic and shallow marine deposits that typically form a series of marine terraces (Gawthorpe et al., 2018)

Rethi-Dendro Formation in the study area

Rethi-Dendro Formation

This study focuses on the lower part of the Rethi-Dendro formation (RDF), the youngest of the Rift Phase 1 lithostratigraphic units exposed south of the town of Xylokastro. The formation represents a sub-lacustrine channel/lobe complex in a basin floor setting, alternating between three main facies associations: (1) marlstones and siltstones,
(2) sandstones and conglomerates, and (3) conglomerates (Gawthorpe et al., 2018). The fine-grained dominated facies association (1) consists of white marlstone units interbedded with thin centimetre-thick parallel bedded sandstones and light grey siltstone beds, and occasional conglomerate lenses <1 m thick. The coarser beds often show sharp, planar bases and partial Bouma-sequences. Facies association 2 comprises locally channelized fine- to coarse-grained sandstone sheets, with subordinate conglomerates. Soft-sediment deformation comprising horizons of isoclinal folds and thrusts, and ball-and-pillow structures may also be present. Facies association 3 is dominated by laterally extensive (<2 km), 3-20 m thick conglomerate bodies with clasts of 1-15 cm (Gawthorpe et al., 2018).

RDF in the Stylia Outcrop

The RDF is exposed several places along the southern margin of the Gulf of Corinth. The Stylia-outcrop studied in this thesis sits within the Kyllini-Kefalari fault block (Fig. 2.2) and mainly comprises channelized conglomerates, sandstones and mudstones.

Muravchik et al. (2020) performed a clast composition analysis of metamorphic clasts to better constrain the provenance of the RDF deposits and investigate the possibility of multiple sediment sources (Fig. 2.3). The Kyllini delta deposits show a proportion of phyllites, but no sign of low-grade metamorphic rocks, whereas the Kefalari delta deposit show no phyllites, but rather a proportion of low-grade metamorphic rocks. The samples derived from the Stylia outcrop show both clast lithologies, but in a lower proportion. This clast composition along with the laterally equivalent position of the outcrop gives reason to suppose the Kyllini and Kefalari deltas as the source of the RDF deposits in the Stylia outcrop (Muravchik et al., 2020).

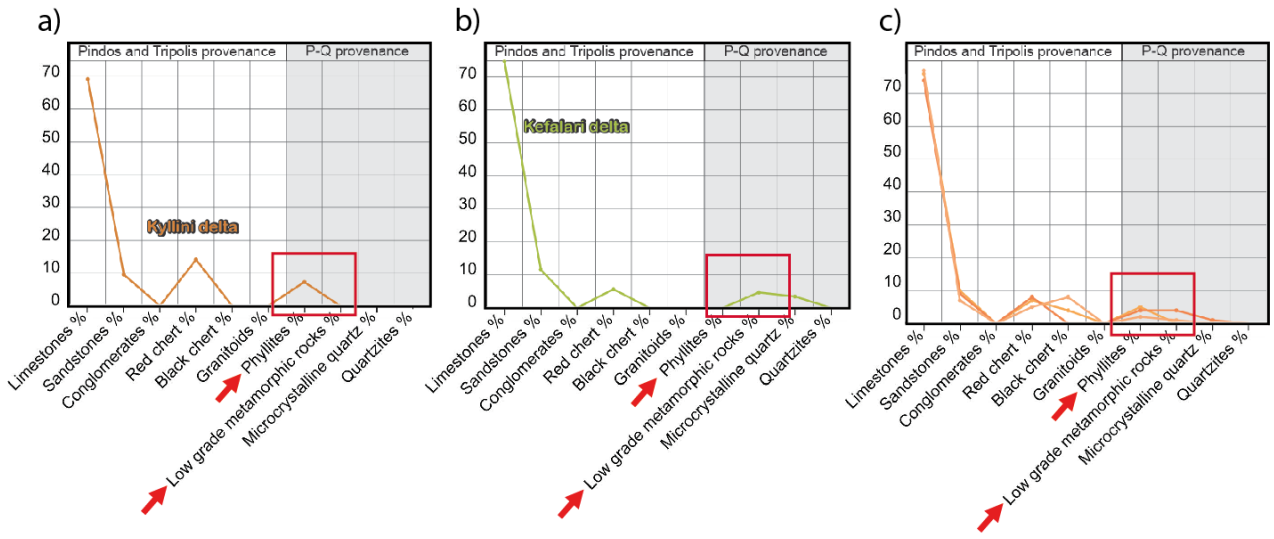

Figure 2.3: Clast composition analysis. The diagrams show the proportions of different clast lithologies in various deposits. a) illustrates the provenance of Kyllini delta deposits, b) shows the provenance of Kefalari deposits, and c) shows the provenance of RDF deposits from the Stylia outcrop. Modified from Muravchik et al. (2020).

RDF in the Amphithea fault block

In addition to the Stylia Outcrop, two larger-scale cross-sections from Muravchik et al. 2020 were used in this thesis to perform seismic modelling (fig 2.4). The cross-sections are located in the Amphithea fault block (fig 2.2) and contain deposits from the 16 stratigraphic units within the RDF described by Muravchik et al. (2020).

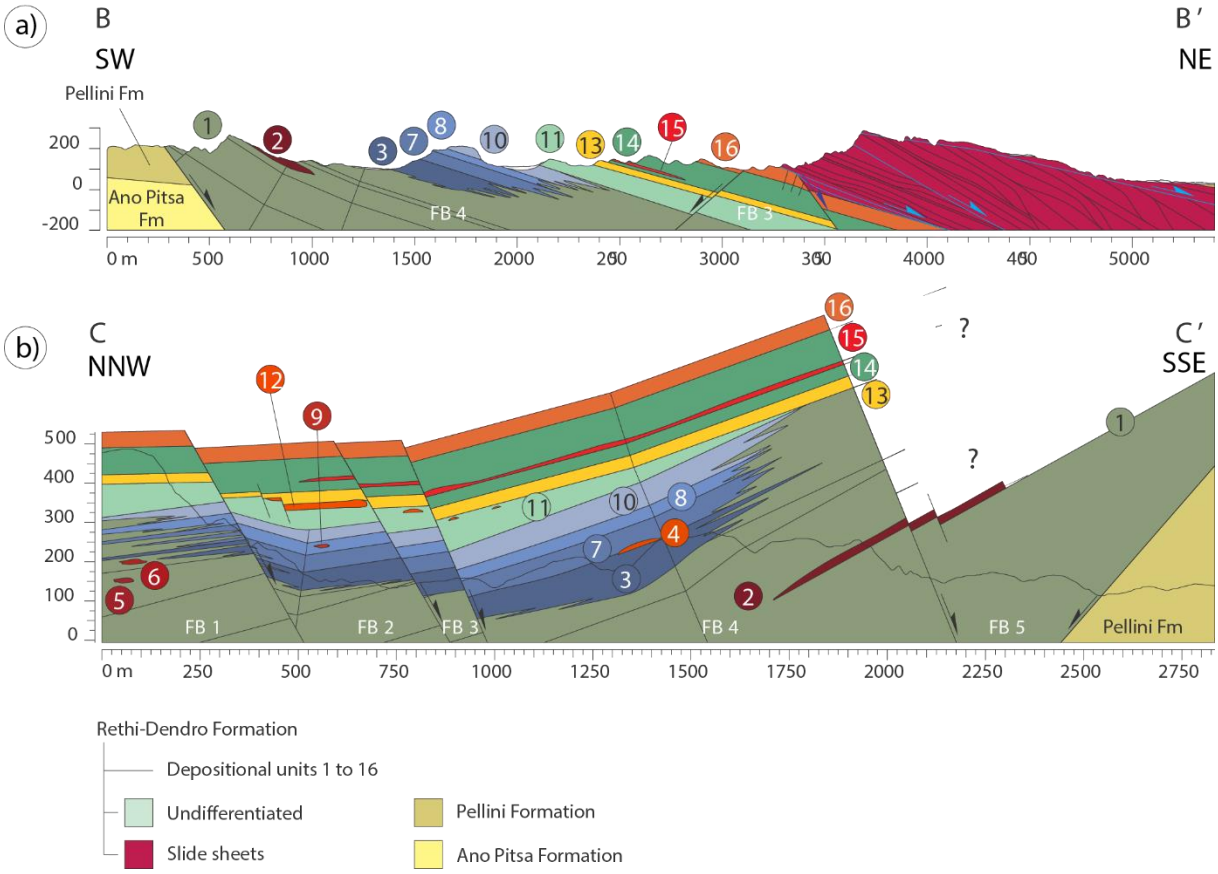

Figure 2.4: Cross-sections in the Amphithea fault block (See Fig. 2.3 for location). (a) Cross-section B-B'. (b) Cross-section C-C' with reconstructed overlying stratigraphy. Normal faults define internal fault blocks (FB) 1, 2, 3, 4 and 5. The different stratigraphic units of the RDF are marked with coloured circles. Modified from Muravchik et al. (2020).

2.2 The Fenja field

In study, the elastic properties used to generate synthetic seismic images of the syn-rift deep-water deposits of the Corinth Rift were derived from two separate wells in the Fenja field, offshore Norway. The Fenja field is located on the Southern Halten terrace within the hanging wall of the Vingleia fault complex in the Northern North Sea, and comprises a small, confined, syn-rift basin sourced from the Frøya High (Jones et al., 2020). The Upper Jurassic stratigraphy and syn-rift succession share similarities with the deep-water stratigraphy of the Corinth rift, with comparable scales and basin physiography including a 2-6 km wide and 10s of kilometres long depocentre in the immediate hanging wall of a major basin bounding fault, feeding a deep-water fan system. The Fenja field therefore makes for a suitable subsurface analogue for the outcrop deposits studied in this thesis.

The early-rift succession mainly consists of mud and siltstone with small fine-grained sandstones deposited by gravity flows. The peak-rift phase comprises more coarse-grained gravity flow deposits sourced from the uplifting footwall and deposited in a submarine fan system in the hanging wall. The late-rift succession mainly comprises mud-rich deposits with minor coarse-grained apron fans (Jones et al., 2020).

Several wells have been drilled targeting the Upper Jurassic syn-rift succession, including the 6406/12-3S and 6406/12-3B wells from which core-photos and well-data have been utilized in this thesis. Both wells are located fairly close to the Vingleia fault in the central hanging wall, the only difference being the more proximal position of 12-3S and the more distal position of 12-3B (Fig. 2.5) (Jones et al., 2020).

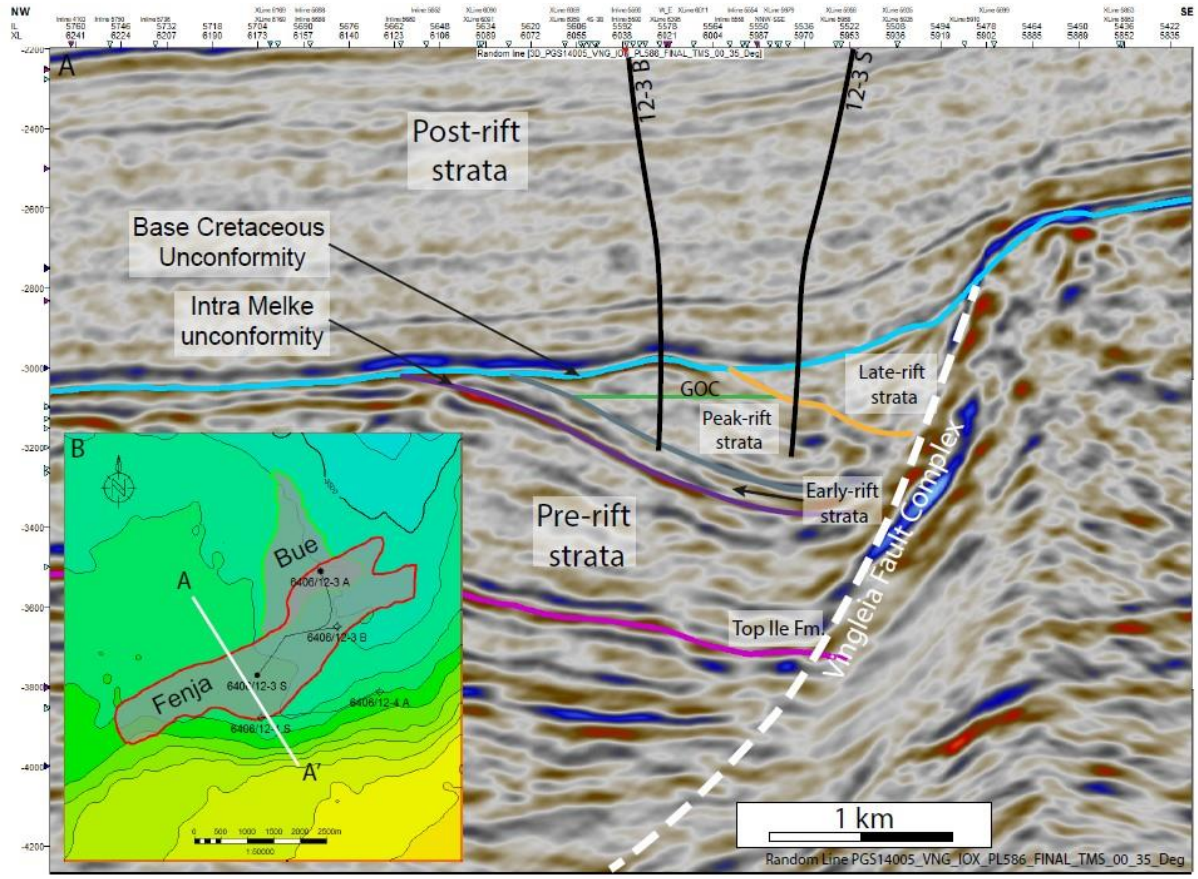

Figure 2.5: Seismic section through the Fenja field, showing the location of the two wells used in this thesis for the calculation of elastic properties for seismic forward modelling. Modified from Jones et al. (2020)

3. Deep-water processes and sedimentary environments

This chapter examines the previous literature on deep-water processes and sedimentary environments and discuss their associated deposits, geomorphology, and stratigraphic architecture in outcrops and seismic sections.

Sedimentation in the deep water is driven by four groups of processes – subaqueous sediment gravity flows, mass transport processes, hemipelagic sedimentation and bottom currents (Fig. 3.1). The focus for this thesis will be on the primary three.

Regarding deep water sedimentation, various definitions and terms exist for the equivalent types of processes. In this thesis, the term " subaqueous sediment gravity flow" (Middleton and Hampton, 1973), shortened to "gravity flow" for simplicity, will cover debris flows and turbidity flows. Another suggested term for the corresponding processes is "subaqueous sedimentary density flow" (Mulder and Alexander, 2001). The term "mass transport" will cover processes like slides and slumps.

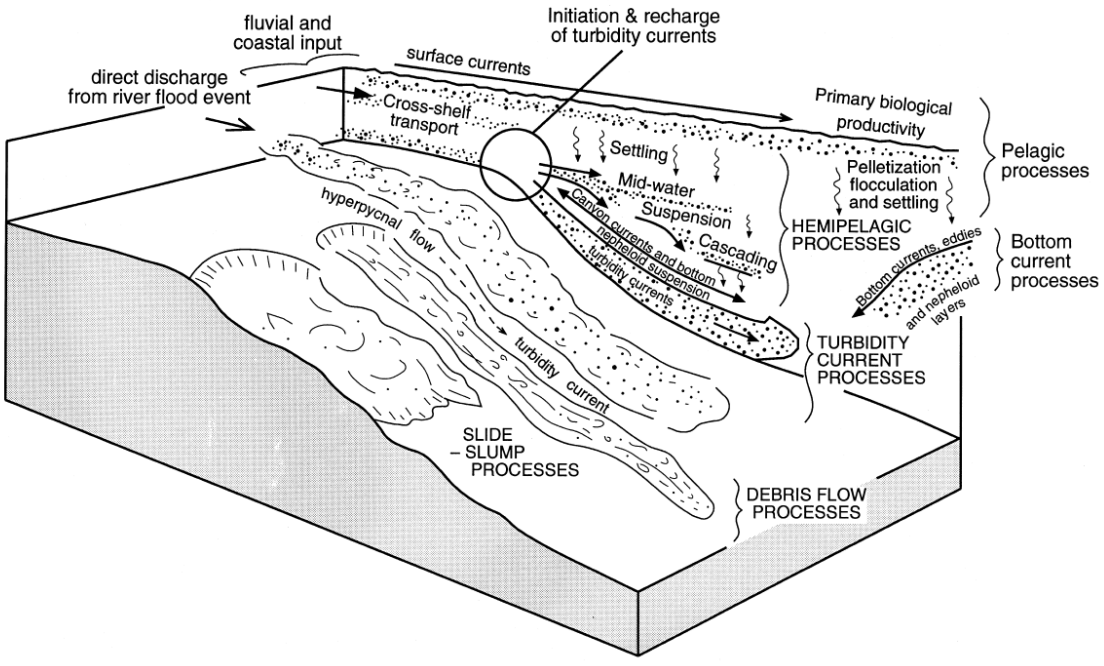

Figure 3.1: Diagram illustrating the range of deep-water sedimentary processes. Modified from Stow and Mayall (2000)

3.1 Deep-water sedimentary processes

As suggested by Middleton and Hampton (1973), a subaqueous sediment gravity flow is a flow of sediment or sediment-fluid mixture that moves under the influence of gravity. Gravity flows move rapidly as detached independent grains, because of high shear-strain rate causing the particles to disengage from their initial coherent bulk of grains (Nemec, 1990).

Mass transport processes are moving bodies of sediment with a 100% volumetric sediment concentration that are also subjects to the influence of gravity. However, in sedimentological terminology, these modes of sediment movement are not regarded as "flow", as they move slowly downslope as one coherent mass of sediment due to low strain-rate (Nemec, 1990, Shanmugam, 2016).

Hemipelagic sedimentation is a process by which sediment particles of clay and silt settle from the water column (Talling et al., 2012).

Classification of sediment gravity flows

Gravity flows fall under a broad scheme of classification which amongst others is discussed by Talling et al. (2012) and Lowe (1982). Gravity flows can be characterized by flow state (turbulent or laminar) (Iverson, 1997, Iverson et al., 2010, Iverson and Vallance, 2001, Mulder and Alexander, 2001), the dominant mechanism(s) for sediment support (Mulder and Alexander, 2001, Middleton and Hampton, 1973) or on the basis of flow rheology (Shanmugam, 2016, Gani, 2004). What these approaches have in common is that the factors needed for characterisation are difficult to measure directly and are rarely observed as features in a deposit/field observation. Talling et al. (2012) proposed a deposit-based classification intended for instances where the only available information regarding the flow comes from its subsequent sediment deposit. This classification interprets flow processes on the basis of recognisable facies types (e.g. elements of the bouma sequence Ta,Tb etc). Figure 3.2 illustrates this approach, using the term "subaqueous sediment density flow" for the processes defined in this thesis as gravity flows.

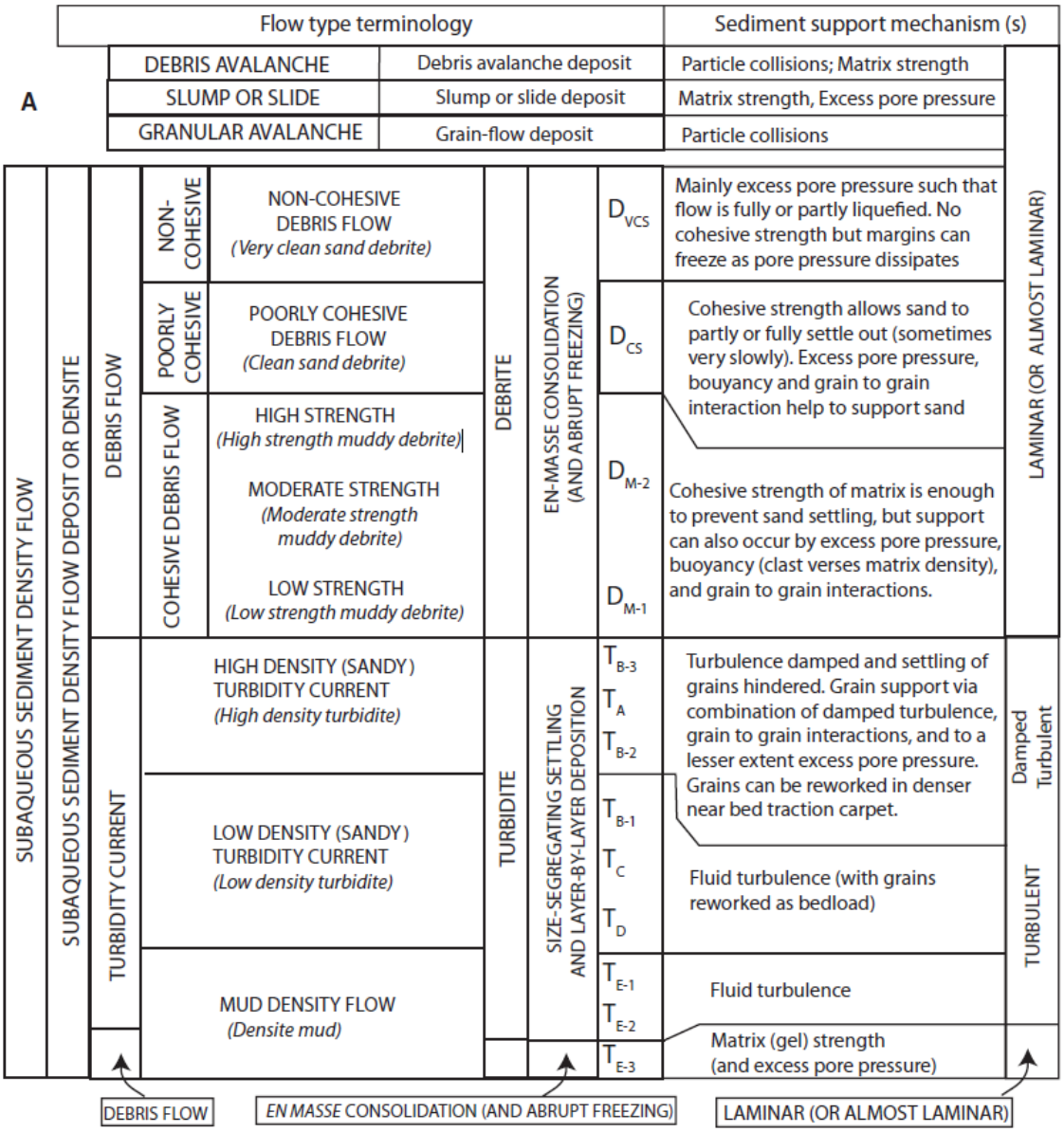

Figure 3.2: Classification scheme of subaqueous density flows (here: gravity flows) developed by Talling et al. (2012).

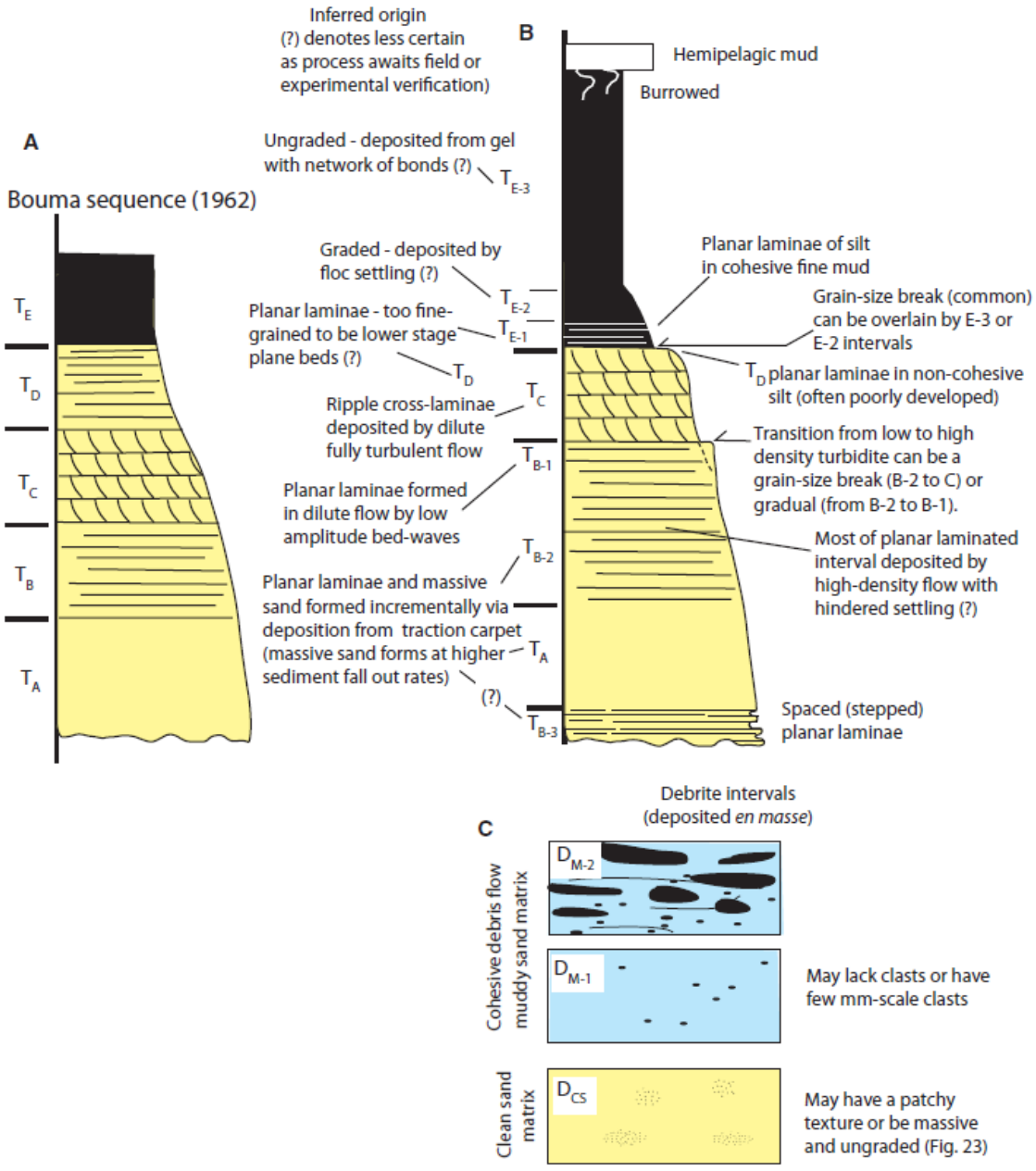

Figure 3.3: (A) The turbidite division sequence as described by Bouma (1962). (B) The turbidite division sequence outlined by Talling et al. (2012), illustrating differences from the Bouma sequence. (C) Generalized debrite intervals described by Talling et al. (2012). Figure modified from Talling et al. (2012).

Processes and their deposits

Debris flows and debrites

Debris flows are laminar flows with plastic behaviour, depositing sediments by sudden *en masse* settling and abrupt freezing (Iverson, 1997, Talling et al., 2012). The deposit left behind by debris flows are commonly called "debrites". Debrites commonly show a lack of segregation between smaller and bigger grain sizes in the matrix, leaving the debrite often poorly sorted and predominantly ungraded (Nemec, 1990, Talling et al., 2012). Some grading may still occur in the debrite, as very large (outsized) clast can settle at the top or base of the deposit even though the adjacent matrix lithifies without segregation. Whether settling of outsized clasts occur near the top or base is dependent on the clast density relative to the density of the surrounding matrix and the degree of variable matrix concentration and fluid content within the debris flow during deposition. Due to the abrupt *en masse* freezing, the thickness of the debrite often reflects the approximate thickness of the flow itself (Iverson, 1997).

Other debrite characteristics include – a lack of sedimentary structures by bedload reworking, a sharp grain-size break at the upper boundary of the debrite interval, chaotically distributed mud clasts (if present) and abrupt pinch-out of the deposit at their margins (Talling et al., 2012).

According to the classification by Talling et al. (2012) debris flows can be recognized as either cohesive, poorly cohesive, or non-cohesive, as a result of variability of mud content in the matrix. The associated subdivision includes debrites with mud-rich sand matrix (D_M cohesive flow), poorly sorted clean-sand matrix (D_{CS}, poorly cohesive flow) and clean sand matrix with no cohesive mud (D_{VCS}, non-cohesive flow) (Fig. 3.2 and 3.3). In natural debris flows however, all types tend to occur continuously by the increasing cohesive mud-content, making it difficult to distinguish the exact boundary between one and the other (Talling et al., 2012).

Turbidity currents and turbidites

Turbidity currents are generally fluidal gravity flows with grains suspended by turbulence, depositing sediments incrementally (Lowe, 1982, Talling et al., 2012). The term "turbidite" defines the subsequent sediment deposit, which is recognized by normal grading, as larger grains preferentially settle. However, in the case of fully steady flow speed and sediment concentration, or the flow consisting of only one grain size, normal grading can be absent

(Kneller and Branney, 1995, Kuenen and Sengupta, 1970). Two types of normal grading typically occur in turbidites, i.e. coarse-tail grading and distribution grading (Middleton, 1967). Coarse-tail grading refers to a decrease in only the coarser grains upwards, whilst distribution grading involves progressive fining upwards of all grain sizes (Lowe, 1982, Middleton, 1967). Unlike debrites, turbidite thickness is not as simply related to flow thickness (Talling et al., 2012).

The subdivision of incrementally deposited turbidites is based on features indicating flow velocity and concentration (Bouma, 1964, Lowe, 1982, Talling et al., 2012). Accordingly, the deposit-based classification by Talling et al. (2012) splits the flow into high- and low-density turbidity currents. Low density turbidity currents have fully turbulent flow conditions with sediment support independent of particle concentration (Lowe, 1982). Low density turbidites often contain ripple-cross laminated intervals, and beds tend to have a tapering shape, reflecting un-hindered settling (Baas et al., 2011, Talling et al., 2012). High-density turbidity currents are characterized by hindered settling and more rapid bed aggradation than in low-density turbidity currents through episodic traction and collapse of sediment layers at the base of flows in "traction carpets" (Sohn, 1997, Talling et al., 2012). The sediment support is also dominated by collisional/frictional grain to grain interactions, excess pore pressure, reduced density difference between particles and fluid, and increased fluid viscosity (Kuenen, 1951, Lowe, 1982). As hindered settling causes more rapid deposition and damping of turbulence, bedforms do not usually form from high-density turbidity currents (Talling et al., 2012).

The vertical succession of a turbidite reveals a size-segregated layering with associated sedimentary structures, reflecting the progressively changing conditions at the location of deposition through time. It commonly consists of mudstones, siltstones and sandstones which can be massive or graded, and include structures like planar laminae and ripple-cross laminae (Bouma, 1964, Lowe, 1982, Talling et al., 2012). This division was first described by Bouma (1962), hence the well-known name “Bouma sequence”. Talling et al. (2012) suggested a more detailed variation of the sequence, with additional intervals and surfaces (Fig. 3.3). Variations of the preservation of different turbidite bed sequences can be related to spatial and temporal changes in the depositional processes of a given flow.

Mass transport processes - slides and slumps

Mass transport processes, which in this thesis includes slides and slumps, occur when stress (and low strain rate) is applied to a static, coherent material, and the material consequently yield along a plane (Nemec, 1990, Savage, 1979).

If the coherent mass of sediments moves along one major slip surface and experience little to no internal deformation, it can be termed a *slide*. If the coherent mass has many slip surfaces and substantial internal deformation, it can be termed a *slump* (Nemec, 1990). Slides typically take place on slopes of 1-4° and can have run-out distances of hundreds of kilometers (Bull et al., 2009, Postma, 1984). These modes of sediment movement often occur continuously, as a slide may turn into a slump (Strachan, 2008).

Hemipelagic sedimentation

Hemipelagic sedimentation is a process by which clay- and silt-sized grains settle from suspension in the water column, typically in between gravity flow events (Talling et al., 2012). Hemipelagic mud is important to recognize in order to distinguish the deposit from turbidite-mud, and further recognize turbidites. The main difference between the two is the presence of calcareous organism-remains. Hemipelagic mud often contains remnants of coccoliths and foraminifera if deposited over the ocean's carbon compensation depth. Turbidite mud usually lacks calcareous content, is better sorted and has a higher organic carbon content and remnant of terrigenous material (Brunner and Ledbetter, 1987, Hesse, 1975, Piper, 1978, Talling et al., 2012).

3.2 Deep-water sedimentary systems, geomorphology, and stratigraphic architecture

Deep-water sedimentary systems are complex, highly variable, and complex to monitor and observe directly. Despite their great variation, deep-water sedimentary systems have many architectural and geomorphic elements in common. These elements may have a higher degree of predictability as they are often observed and can be included in an exemplifying model describing such a system. Which architectural elements are most fundamental and what hierarchy and scale are most appropriate for their description is however a subject of debate (Stow and Mayall, 2000).

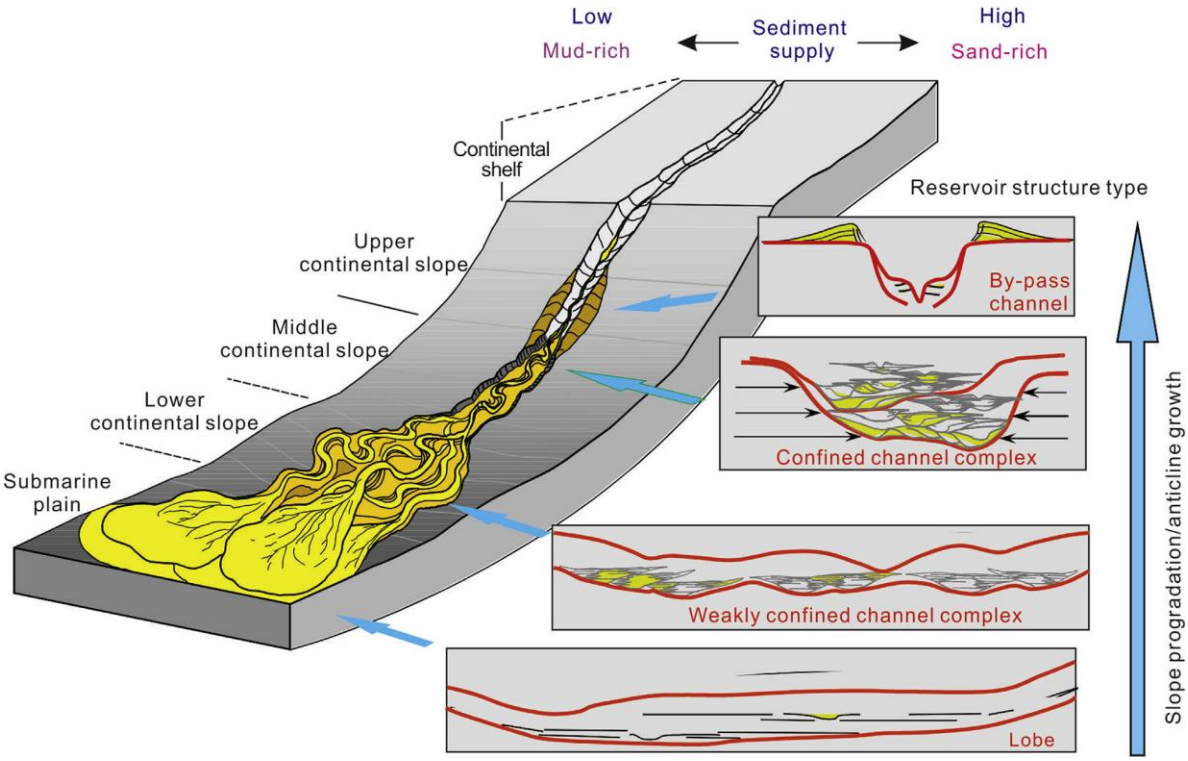

Figure 3.4: Illustrative model of a deep-water sedimentary system from source to sink, with an incised valley and by-pass channel on the continental shelf and upper slope, confined and weakly confined channel complexes in the mid- and lower slope, and lobe development on the submarine plain. Modified from Huang (2018)

The sediment-routing system from non- and shallow-marine environments into the deep-water basin floor settings can include submarine canyon-channel systems, progressing from V-shaped canyons incised into the shelf and upper slope, into more U-shaped channels with overbank deposits on the lower slope. At their terminal area of deposition, channelized or non-channelized submarine fan and lobe systems may form (Huang, 2018, Menard Jr, 1955) (Fig. 3.4).

The geomorphic elements which will be discussed in this chapter includes canyons, channels and channel-levee systems, submarine fans and lobes. Their subsequent sediment deposits will be reviewed, as well as their geomorphology and stratigraphic architecture in both outcrops and seismic sections (Table 1).

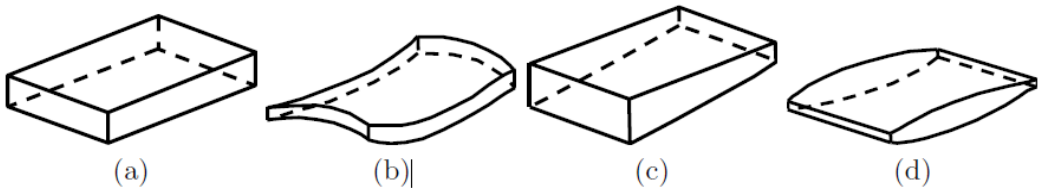

Figure 3.5: External shapes of architectural elements. (a) sheet, (b) sheet drape, (c) wedge, and (d) lens. Modified from Schlaf et al. (2005).

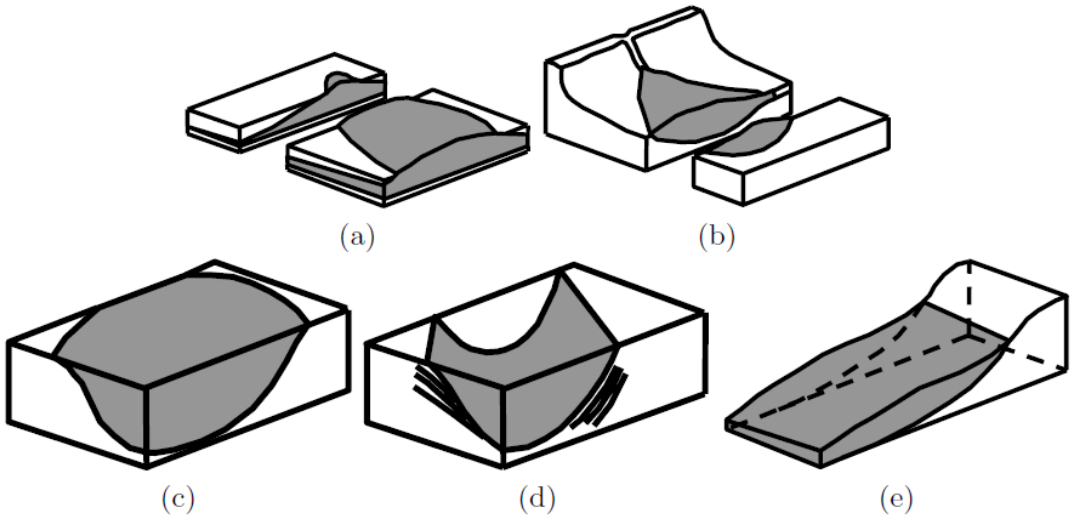

Figure 3.6: External shapes of architectural and geomorphic elements. (a) mound, (b) fan, (c) basin fill, (d) channel fill, and (e) slope front fill. Modified from Schlaf et al. (2005).

Canyons

A canyon is a steep-sided, often V-shaped valley that incises into the continental shelf and slope, and acts as conduits for the transfer of sediments into the deep-water (Fisher et al., 2021, Harris and Whiteway, 2011). The formation of canyons is caused by erosion from gravity flows and other mass transport processes into the shelf and slope. In terms of lithofacies, deposits such as turbidites, debrites, mass-transport deposits, and hemipelagites, are capable of accumulating within submarine canyons (Shanmugam, 2016).

Harris and Whiteway (2011) classified canyons into three types based on their morphology - Type 1 shelf-incising canyons bathymetrically connected to a major river system, Type 2 shelf-incising canyons with no bathymetric connection to a major river system; and Type 3 blind canyons incised onto the continental slope. Canyons/channel on active margins are documented to be steeper, shorter and more dendritic than those on passive margins (Harris and Whiteway, 2011).

In a cross-sectional profile, submarine canyons are most commonly V-shaped, although U-shapes have also been observed on occasion (Shanmugam, 2016). In a longitudinal profile, the majority of submarine canyons are concave-up. The degree of concavity depends on the interaction between erosion and uplift, reflecting a record of environmental and tectonic processes through development. In areas of high tectonic activity, submarine canyons tend to have a more linear longitudinal profile compared to the more concave shapes of canyons in areas of low tectonic activity (Soutter et al., 2021).

In a seismic section, canyons are best recognized by their sharp and erosive steep-walled base commonly identified as a high amplitude reflection. As they are often filled by mass-transport deposits and gravity flow deposits, canyons tend to have chaotic, discontinuous internal reflectors.

Channels and channel-levee systems

Deep-water channels are subaqueous, elongated depressions which form conduits actively traverse by gravity flows and mass transport (Mutti and Normark, 1987, Normark, 1970, Tek et al., 2022). Submarine channels appear in various parts of the deep-water sedimentary system from source to sink, for instance as bypass-channels at the base of shelf canyons, in mid-slope channel-complexes or in upper- or mid-fans on the basin floor (Stow and Mayall, 2000).

The stratigraphy of submarine channels can progress as either erosional or aggradational, and geomorphological features may be meandering, braided, sinuous or straight, converging, or diverging (Belderson et al., 1984, Damuth et al., 1988, Hesse, 1989, Normark, 1970, Shanmugam, 2016).

Overbank deposition on the sides of a channel can cause the formation of levees, which are wedge shaped deposits that typically dip away from the channel. Aggradational channels with genetically linked levees are defined as a channel-levee system. Aggradational submarine channels are typically highly sinuous unlike dominantly erosional channels (Kane et al., 2007). Sinuous channel complexes with their subsequent banks and overbanks often sit within larger channels, valleys or canyons flanked by large overbanks, so-called “master-overbanks” (Kolla et al., 2007). Similar to canyons, the strata of deep-water channel-fill can include a variety of facies, including muddy, sandy or gravelly sediments deposited by turbidity currents, debris flows, mass-transport and hemipelagic sedimentation, dependent on flow conditions (Stow and Mayall, 2000).

McHargue et al. (2011) suggested a hierarchical scheme for the organization of architectural and geomorphic observations from deep-water channels. The fundamental architectural unit is titled a “channel element”, which includes the surface of a channel-form and its subsequent sediment-fill. Channel elements are distinguished from each other by an abrupt lateral or vertical offset of depositional facies. One individual channel element can consist of several smaller channel-forms stacking vertically with no significant lateral offset of depositional facies. These smaller channel-forms are called “channel-stories”. The stacking of several channel-elements in a consistent pattern makes up a single “channel-complex”. The presence

of multiple related channel-complexes can be sorted into a “complex-set” (McHargue et al., 2011).

In a cross-section, the geometry of deep-water channels are mostly U-shaped, but can also be V-shaped and saucer-shaped, whilst they in a longitudinal profile may look either smooth, abrupt or stepped (Stow and Mayall, 2000). Internal geometries include e.g. tabular sheets, lenses, ribbons and mounds (Fig. 3.5 & Fig. 3.6)

The seismic signature of deep-water channels reflects a variety of different architectural elements and textures. Typical channel-fill deposits are characterized by high-amplitude, discontinuous reflections indicating interbedded coarse sands and gravels with muddier horizons. In the case of channel-fill with a singular lithology without distinct interbeds, the deposit may be acoustically transparent, with low-amplitude and discontinuous reflections. These deposits may consist of sand or mud deposited after channel abandonment (Walker, 1992). In channel-levee systems with channel aggradation, the high-amplitude discontinuous reflections may stack vertically (Walker, 1992). Many banks and overbanks have relatively low-amplitude but continuous reflectors (Kolla et al., 2007). The levees themselves are typically characterized by low-amplitude discontinuous to low-amplitude continuous reflections within the wedge-shaped form (Walker, 1992).

Fans and lobes

Submarine fans are accumulations of sediment deposited at the distal part of a deep-water sedimentary system, forming a variety of shapes across the sea-floor, such as radial-, cone- or fan-like morphologies (Huang, 2018, Menard Jr, 1955, Shanmugam and Moiola, 1988, Walker, 1978). Submarine fan systems typically consist of several deep-water components like canyons, channels and lobes. Consequently, submarine fans can be both channelized and non-channelized (Shanmugam and Moiola, 1988). The most volumetrically important process for deposition of sediments in submarine fans are gravity flows, whilst slumps and liquefied flows are of less importance (Middleton and Hampton, 1973).

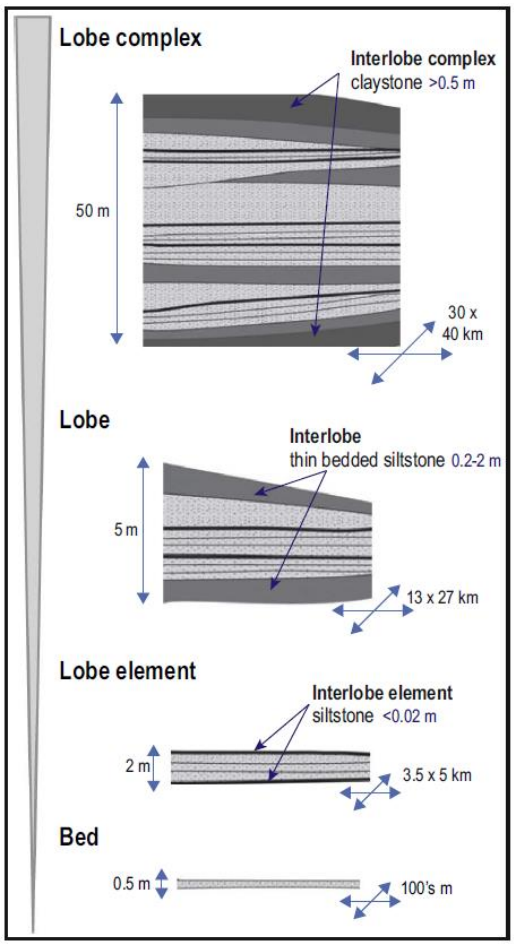

Figure 3.7: Hierarchical classification of Prélat et al. (2009). Modified from Cullis et al. (2018) after Prélat et al. (2009).

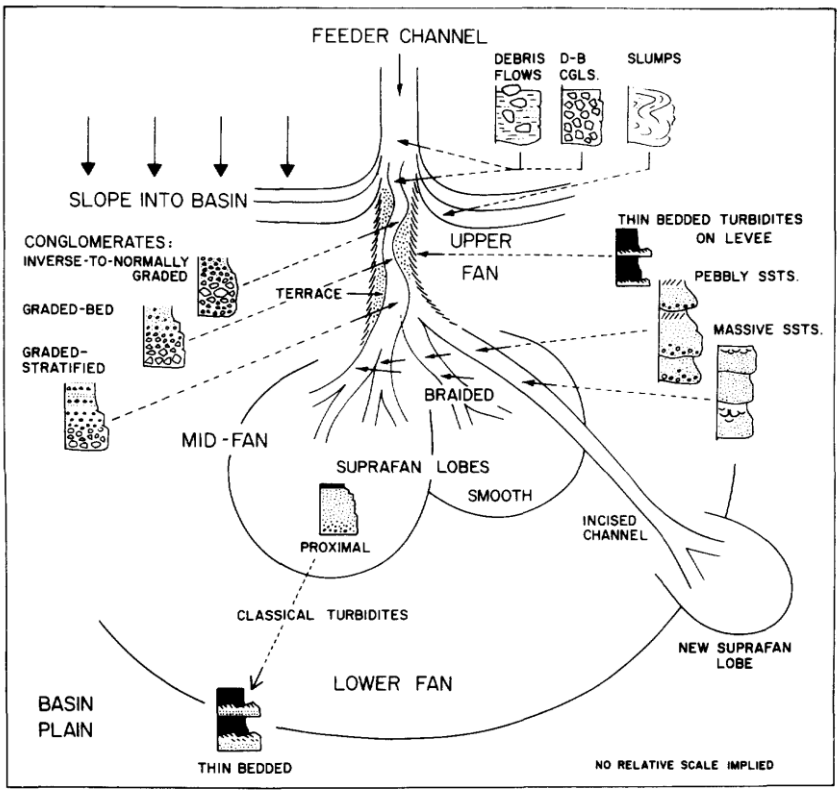

Figure 3.8: Model of submarine-fan deposition, relating facies, fan morphology and depositional sub-environment. Modified from Walker (1978).

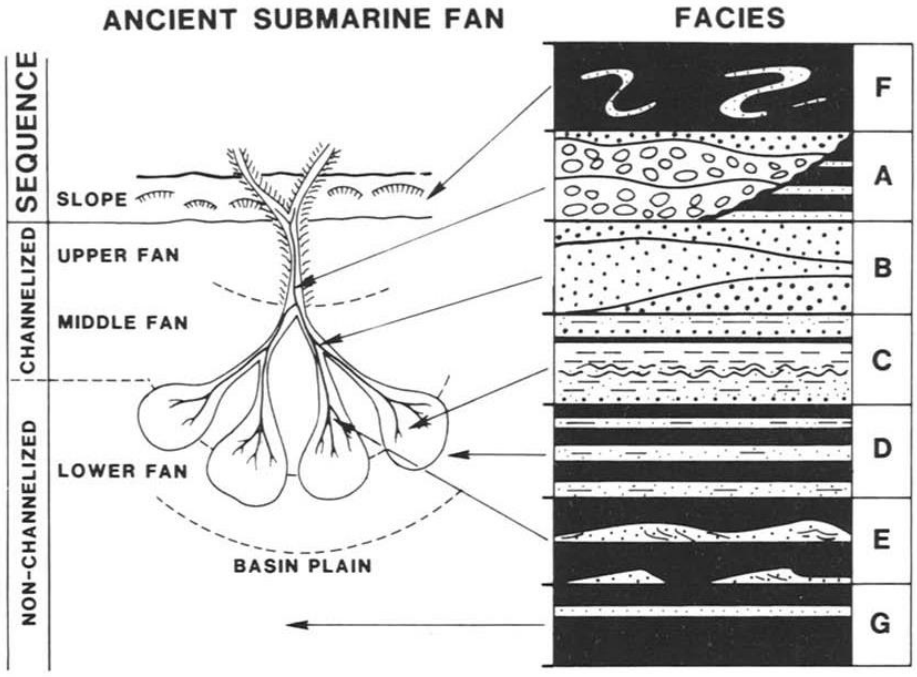

Figure 3.9: Components of an ancient submarine fan and related distribution of facies. Facies nomenclature is from Mutti and Ricci Lucchi (1972, 1975). Modified from Shanmugan and Moiola (1988)

Submarine depositional lobes are defined as lobate sediment-bodies developing at or near the mouths of submarine channels, most commonly deposited by turbidity currents. Lobes are characterized by laterally continuous, sheet-like beds with thickening upwards successions (Lowe, 1982, Mutti and Normark, 1987, Mutti and Ricci Lucchi, 1978, Spychala et al., 2017).

Several hierarchical classification schemes have been proposed for lobes, including a four-tiered facies-based classification suggested by (Prélat et al., 2009), which from smallest to largest scale include “bed”, “lobe element”, “lobe” and “lobe complex” and their subsequent sedimentary components (Cullis et al., 2018)

Submarine fan morphology is commonly subdivided into an upper fan, a middle fan and a lower fan (Barnes and Normark, 1985, Normark, 1978, Walker, 1978). However, the application of these terms is not agreed upon. Walker (1978) described a model with an upper fan (suprafan) characterized by a single leveed deep channel, a middle fan built up by suprafan lobes shifting position, and a lower fan that is more bathymetrically smooth and non-channelized (Normark, 1978, Walker, 1978) (Fig. 3.8). In reality, factors like the absence of channels in the lower fan or the presence of lobes in the middle fan may apply for many submarine fans but might not for others. Shanmugam and Moiola (1988) proposed a more general description with an upper fan recognized by the presence of a major feeder channel (canyon), a middle fan consisting of a network of distributary channels and associated overbank deposits, and a lower fan built up by lobes and sheet sands (Fig. 3.9).

The external form and seismic signature of submarine fans is dependent on which sub-environment of the fan is imaged and what geomorphic elements are present. Each element and their corresponding seismic signature and geomorphological architecture is described and summed up in Table 1.

3.3 Deep-water deposits in rift basins

Much of the work on deep-water sedimentary systems, processes and architectures is heavily focused on finer grained systems, typically on passive margins which are often large in size. However, deep-water systems in rift basins are noted typically to be smaller, coarser grained, and more complex in their interactions with tectonics and climate than deep-water systems on passive margins (e.g. Strachan et al., 2013). As rift basins form in extensional tectonic settings,

faulting is a major controlling factor when it comes to driving sedimentation, fluid-flow and gravity-flow pathways and creating depositional sites (e.g. Leeder and Gawthorpe, 1987; Gawthorpe and Leeder, 2000; Mack et al., 2009). Active rift systems have the potential to form deep and narrow depocenters characterized by complex high topographic relief, and a variety of sediment sources and active sedimentary processes. Syn-rift deposits may therefore produce important hydrocarbon targets.

Table 1: A selection of architectural elements and their corresponding outcrop- and seismic architecture.

Architectural element	**Outcrop architecture**				**Seismic architecture**		
	External form		Internal		Seismic Character		
	Strike	Dip	Deposits	Geometries	Amplitude	Continuity	Internal Configuration
Canyons	V-shaped	66% concave up, 34% linear	Mass transport deposits, debrites, turbidites, hemipelagites	Sheets, lenses, ribbons, mounds etc.	High	Low	Subparallel
Channels	U-shaped	Smooth, abrupt, stepped	Slumps, debrites, turbidites	Sheets, lenses, ribbons, mounds etc.	High	Low	Subparallel
Levees	Wedge			Sheets	Low/Fair	Moderate	Subparallel, divergent to channel
Lobes	Concave	Concave	Turbidites	Sheets	High	Moderate	Mounded
Mass-transport complex	Mound	Mound	Slides, slumps	Chaotic	Low/Fair	Poor	Mounded, hummocky
Non-channelized lower fan	Sheet	Sheet	Sand bypassed through mid-fan channels		Low-High	Fair	Subparallel

4. Seismic modelling

Seismic modelling comprises various methods by which synthetic seismic is generated in order to better understand elastic wave propagation in the subsurface (Lecomte et al., 2016). It allows investigating at which level of detail geological models can be imaged in seismic data and the impact of various geological and geophysical parameters on seismic images.

4.1 Main modelling approaches

Three key approaches exist for the modelling of synthetic seismic images – 1D convolution modelling, 2(3)D full-wavefield (FW) modelling and 2(3)D ray-based (RB) modelling. The most ideal strategy is based on FW modelling methods to generate complete synthetic seismograms followed by processing to produce migrated images. This method is however time-consuming and requires extensive resources (Lecomte et al., 2015). The simplest and most cost-effective method is 1D convolution modelling, which is especially beneficial for well-calibration and seismic inversion. The drawback with this method is that it only accounts for horizontally stratified structures without lateral variation in velocity. Other methods are therefore needed for realistic modelling of complex and detailed targets. Ray-based modelling methods are more adaptable in that they allow for variations of different parameters which ultimately affects the resolution and illumination of seismic data (Lecomte et al., 2015).

4.2 2(3)D PSF-based convolution modelling

The approach used in this thesis is a 2(3)D convolution version of RB modelling, utilizing a so-called Point-Spread Function (PSF) to simulate 2(3)D seismic prestack depth-migration (PSDM) images. PSFs are 2(3)D seismic responses of diffraction points after a PSDM; knowing such elementary responses allows modelling PSDM-alike images. Here, the PSF used for modelling 2D seismic sections from outcrops is generated via so-called PSDM filters pre-designed based on a few key parameters; applying a Fourier Transform (FT) to the PSDM filter yields the desired PSF (Fig. 4.1). The latter is then convolved with an input reflectivity model to simulate angle-dependent depth images resembling seismic images in the subsurface (Fig. 4.2) (Lecomte et al., 2015).

4.2.1 Geophysical parameters

A key factor in PSF-based convolution modelling is the illumination vector (I_{SR}; Lecomte, 2008). The I_{SR} is characterized by its orientation and length and can be generated at a reference point in the target for a given velocity model and seismic survey with a set of shot and receiver pairs. When not having access to a velocity model and a given survey, which is the case for the present work, a generic I_{SR} span can be generated by giving an average velocity, the maximum illumination angle, an incident angle and a wavelet (Lecomte et al., 2016), and noise. These parameters can be altered in the modelling method to simulate and investigate different imaging outcomes (sensitivity analyses).

Maximum illumination angle

The maximum illumination angle (MIA) is defined as the maximum (geological) dip of imageable strata during seismic acquisition. Seismic surveys are indeed limited in their spatial extent as well as the recording at receivers is limited in time, which in turn prevent steep dips to be imaged in seismic, even if the corresponding reflectivity is non-zero. A standard 3D acquisition over a rather horizontally stratified overburden will thus seldom illuminate geological dips steeper than 50-60°, hence generating seismic images where steep structures (e.g., faults) only appear indirectly.

Incident angle

The incident angle θ of a seismic wave is dependent on the (seismic) offset, i.e., the distance between the source and the receiver. For instance, a 0° incident angle indicates zero offset. Larger incident angles and subsequently wider offset typically cause poorer vertical and lateral resolution, hence the importance of that parameter (Rabbel et al., 2018). In addition, the incident angle controls the reflectivity coefficient, thus also constraining the input reflectivity grid for the seismic modelling.

Wavelet

Different wavelet types like Ormsby-, Ricker-, Klauder- and Butterworth-wavelets may also influence the synthetic seismic images. For simplicity, only the Ricker wavelet will be used for seismic modelling in this thesis. Ricker wavelets are zero-phase wavelets with a central peak

and two smaller side lobes and are defined based solely on the frequency parameter (Ryan, 1994).

Noise

A level of coloured random noise can be added to synthetic seismic images to mimic a more realistic seismic effect (e.g. Lubrano-Lavadera et al., 2019), as true seismic data combines both signal and noise. The noise-level is defined by percentage.

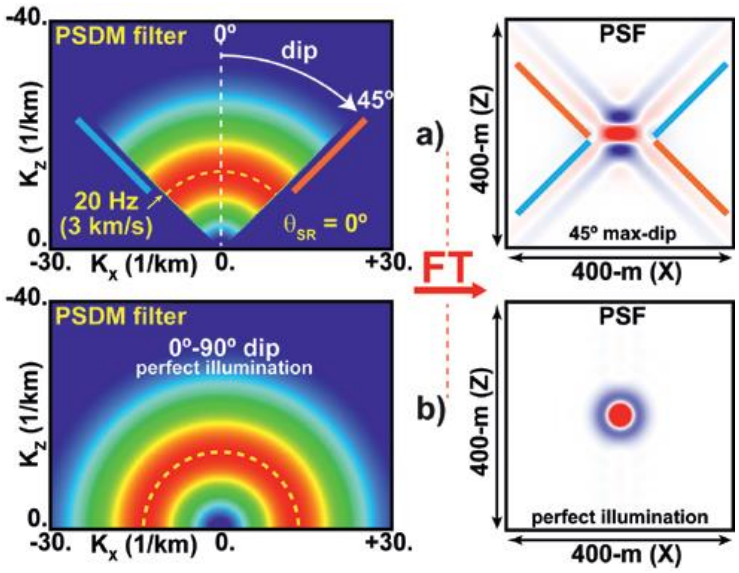

Figure 4.1: PSF produced by Fourier transform based on a PSDM filter with a set average velocity, incident angle (θ), wavelet frequency (f) and maximum illumination angle (MIA). The figure illustrates two options. (a) shows a PSDM filter where Vp: 3 km/s, θ: 0°, f: 20Hz, and MIA: 45°, generating a PSF with resolution and cross-pattern from MIA. (b) illustrates a PSDM filter and PSF with perfect illumination (MIA: 90°) Modified from Lecomte et al. (2016)

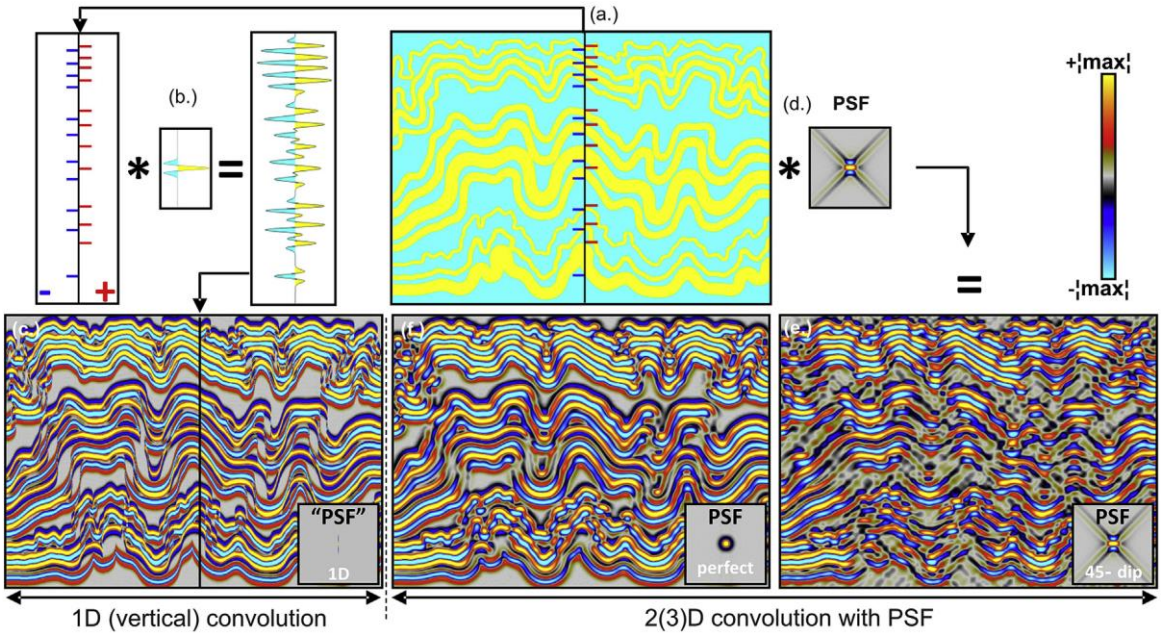

Figure 4.2: 1D and 2(3)D convolution modelling. (a.) Acoustic impedance input model. (b.) 1D convolution modelling where vertical reflectivity logs are convolved with a wavelet to produce a seismic trace. (c.) synthetic seismic section produced by gathering the seismic traces. (d.) PSF-based convolution modelling, where the PSF is convolved with the 2D reflectivity model. (e.) synthetic seismic section from PSF-based convolution modelling with a 45º MIA. (f.) synthetic seismic section from PSF-based convolution modelling with perfect illumination (90º MIA). Modified from Anell et al. (2016)

4.2.2 Seismic resolution and detectability

Seismic resolution determines the smallest detectable features in the subsurface, for instance the top and base of a rock layer. The seismic resolution is controlled by wavelet properties, primarily the dominant wavelength (λ) (Kearey et al., 2002, Simm and Bacon, 2014). Wavelength is a function of velocity (v) and frequency (f):

$$\lambda = \frac{v}{f} \qquad \text{(Eq. 4.1)}$$

Generally, seismic velocity increases with depth whilst high frequencies are absorbed downwards, resulting in a vertical resolution that decreases with depth (Simm and Bacon, 2014). According to Widess (1973), vertical resolution is normally a quarter of a wavelength ($\lambda/4$).

Lateral resolution is dependent on the size of the so-called *Fresnel zone*, meaning the area of constructive reflection accumulation surrounding the point of reflection (Lindsey, 1989). If a change in reflection occurs in an area smaller than the extent of the Fresnel zone, it can typically not be detected in the seismic expression. To help reducing the impact of the Fresnel zone, migration is used, thus reducing that resolution to half of a wavelength ($\lambda/2$) at best in standard 3D acquisition. In a perfect illumination case, the lateral resolution would be reduced to $\lambda/4$, as for the vertical resolution. Lateral resolution is especially significant when it comes to detecting lateral changes in facies, or geomorphic elements such as channel cuts and levee wedges (Lindsey, 1989).

Seismic detectability refers to the minimum thickness of a rock unit visible in reflection seismic data, and typically corresponds to the vertical and lateral resolution. However, even small features below the theoretical resolution can be detectable if they are “reflectivity-strong” and/or not aligned with the surrounding material (discordance).

5. Data and methodology

This chapter provides an overview of the data and methods used in this thesis to produce a 3D virtual outcrop model (VOM) and generate 2D synthetic seismic models. The synthetic seismic images produced in this study are based on the Stylia outcrop in the Kyllini-Kefalari fault block, and two regional large-scale cross-sections in the Amphithea fault block of the Corinth Rift, Greece.

5.1 Data acquisition and software

The outcrop data used in this thesis includes drone photographs and videos as well as sedimentary observations obtained in the field by Martin Muravchik (UiB). Well data used to define elastic properties for seismic modelling derives from the 6406/12-3S and 6406/12-3B wells in the Fenja field, offshore Norway. The software utilized in the photogrammetry process includes Exifftool, ffmpeg, in-house scripts written in Python, Agisoft Metashape, CloudCompare and Meshlab. The purpose of each software is explained in figure 5.1. Geological interpretation was done in LIME, and data preparation for seismic modelling was done in Adobe Illustrator, Paint.net and MATLAB. The actual seismic modelling was performed in NORSAR SeisRoX.

5.2 3D Virtual outcrop model from photogrammetry

The first stage of data processing included frame extraction from the drone videos at every 2 second in order to ensure sufficient coverage of the outcrop. This was done by running a code in the Windows Command Prompt. The extracted frames were then geotagged and the correct variable and constant camera parameters were assigned to the corresponding frames using a combination of Exiftool and ffmpeg libraries in in-house python scripts. The final step of the data preparations included filtering of all the photos based on quality and relevance, so that no photos of low resolution or irrelevant coverage were included in building the VOM. All photos were then processed in Agisoft Metashape, and a 3D photogrammetric outcrop model was generated, following the workflow described in Figure 5.1.

Figure 5.1.: Workflow explaining the making of a Virtual Outcrop Model by photogrammetry.

5.3 Geological models

5.3.1 Geological interpretation in LIME

The Stylia VOM was thereafter exported to LIME software for geological interpretation. The goal of the interpretation was to capture the main stratigraphic architecture, boundary surfaces and rock-body geometries of the exposure by recognizing e.g., changes in lithology, vertical and lateral colour differences, or major erosional features. The primary interpretation was divided into three scales of observations:

1. "Major surfaces" representing a significant change in lithology or a sharp erosional surface between major depositional elements.
2. "Minor surfaces" representing smaller scale architectural elements like e.g., conglomerate or sandstone lobes and lenses.
3. "Details" representing smaller scale structures, bedding or lamination features etc.

The interpretations were mapped out using polylines and supported by comparison with high-resolution drone footage and still pictures from the field. Measurements of channel dimensions such as widths and thicknesses were also obtained from the Stylia VOM.

5.3.2 Preparation of geological input model for seismic modelling

The input data for seismic modelling comprises a rectangular 2D section of the geological model as a bitmap where each pixel corresponds to a colour representing a certain lithology to be populated with elastic properties. Because outcrops never have smooth, fully vertical surfaces, a 2D panel was created in LIME to project the polylines onto a vertical plane similar to that of a seismic section through stratigraphy. The panel was then exported to the graphics editing software Adobe Illustrator to complete the geological input model by extrapolating and interpolating interpretations where data were insufficient, and defining lithologies as either mudstone, sandstone, or conglomerate. Strata above and below the outcrop were added based on the observed lithology and stratigraphy of the surrounding area. The model was then converted to greyscale in Paint.net, resulting in a 2D geological input model ready to be assigned elastic properties.

5.3.3 Regional cross-sections

In addition to the Stylia Outcrop, two cross-sections from Muravchik et al. 2020 (fig 2.4) were used to produce larger scale seismic models. The geological input models for seismic modelling were produced by determining the dominant lithology of each stratigraphic unit based on descriptions of the 16 stratigraphic units of the RDF in the Amphithea fault block by Muravchik et al. (2020) (fig 5.2).

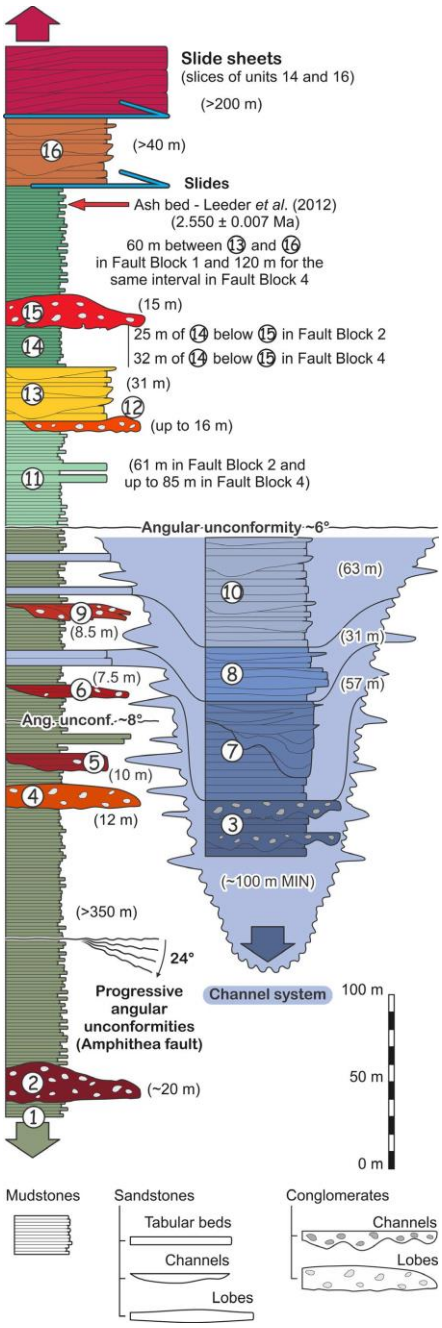

Figure 5.2: Stratigraphic column of the RDF in the Amphithea fault block. The different units are numbered from 1 to 16 following their stratigraphic order. From Muravchik et al. (2020).

5.4 2D synthetic seismic from seismic modelling

5.4.1 Elastic properties

P- and S-wave velocity and density-values for mudstones, sandstones and conglomerates were collected from the 6406/12-3S and 6406/12-3B wells from the Fenja oil- and gas-field in the Northern North Sea (Table 5.1). The area was chosen because of its similarity to the sedimentary environment of the Corinth Rift. Intervals for each lithology were picked based on core photos and sonic-log data. All elastic properties were extracted from intervals below the oil-water contact (OWC) to avoid an issue with different fluids.

Table 5.1: Input elastic properties for different lithologies present in the Stylia outcrop and regional cross-sections, calculated based on well-data from the Fenja field.

Well	Lithology	Interval (m-MD)	Vp (km/s)	Vs (km/s)	Den (g/cm^3)	AI (km/s g/cm^3)
6406/12-3S	Mudstone 1	3765.3-3766.3	4.1	2.4	2.3	9.4
	Mudstone 2	3794.7-3797.1	3.8	2.3	2.5	9.6
	Sandstone	3709.1-3710.9	4.1	2.5	2.4	9.8
	Conglomerate	3712.1-3713.1	3.9	2.3	2.4	9.4
6406/12-3B	Mudstone 1	4253.3-4254.7	3.7	2.2	2.6	9.6
	Mudstone 2	4208.8-4211.5	3.9	2.2	2.6	10.1
	Sandstone	3862.0-3865.0	4.3	2.6	2.4	10.3
	Conglomerate	3844.5-3845.5	4.1	2.5	2.4	10.0

5.4.2 Seismic forward modelling using the 2D PSF-based convolution method

After creating the complete 2D input geomodel, MATLAB was used to run a script assigning the correct Vp-, Vs- and density-values to unique greyscale codes representing the corresponding lithology. The results comprised five different property grids (block, density, Vs, Vp, and noise) stored as SEG-Y files. The final stage of the process was done in SeisRoX, where 2D PSF-based convolution modelling was performed to produce synthetic seismic of the different input models. This was done following the workflow described in Figure 5.3. The theory behind this method was explained in Chapter 4.

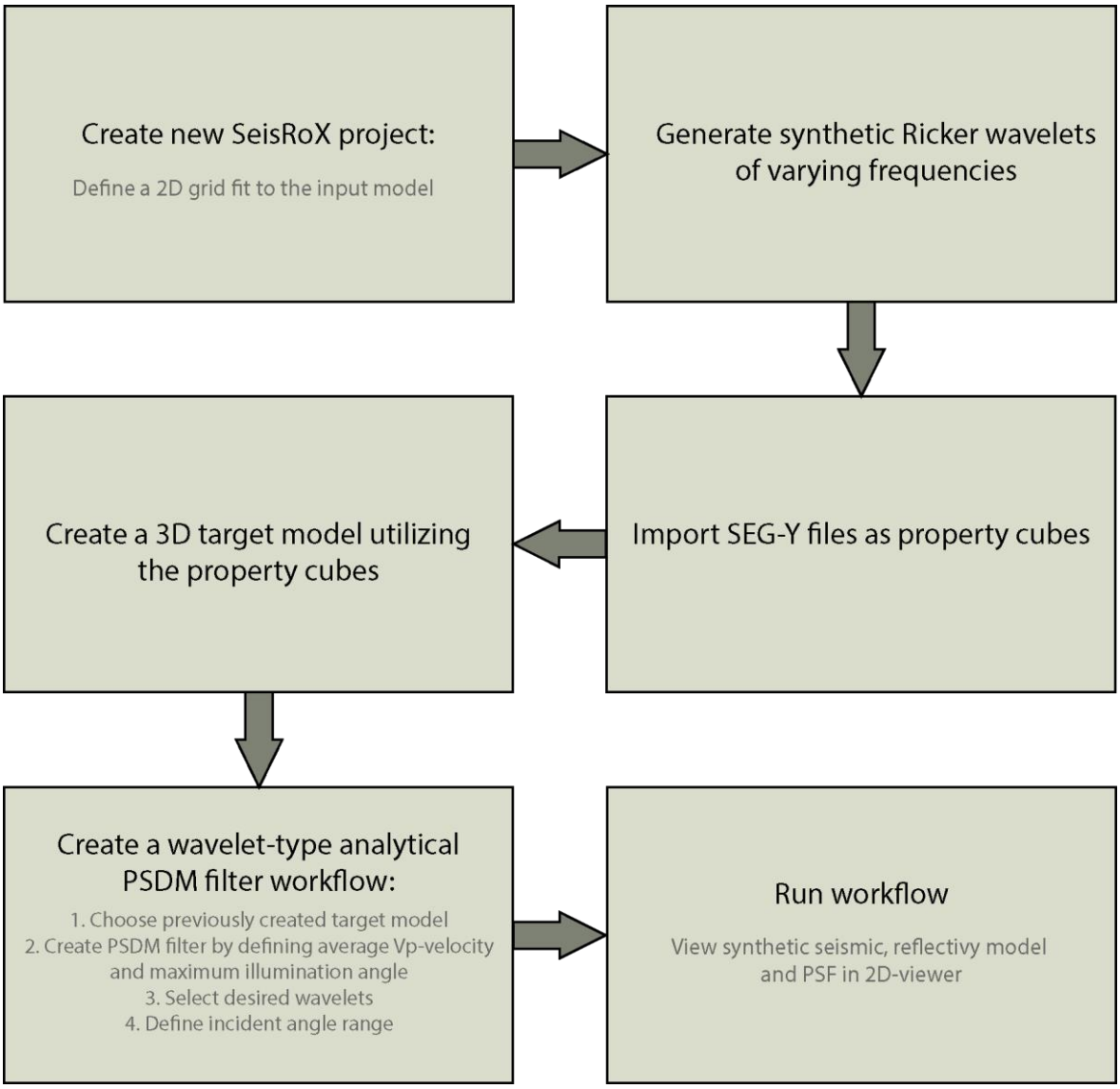

Figure 5.3: 2(3)D PSF-based convolution modelling workflow in SeisRoX ("*Analytical PSDM Filter*" type, i.e., for cases without seismic survey specification and overburden model).

5.5 Sensitivity study

To investigate the impact of various geophysical and geological parameters on seismic images, various sensitivity analyses were conducted. This included different geological interpretations of the input model, along with varying the dominant frequency of the input wavelet (f), the incident angle (θ), maximum illumination angle (MIA) and level of noise. The different compositions of input models, varying parameters and constant parameters are described in Table 5.2.

Table 5.2: Ranges of varying and constant parameters for each input model. The parameters in white boxes are constant for each of the varying parameters. e.g.: when modelling the Stylia Outcrop model with varying dominant frequencies, a constant maximum illumination angle of 45º and incident angle of 20º are used to better visualize the direct effects of different frequencies.

Model	**Geological Variations:**	**Frequency (Hz): 20, 40, 60, 140**	**Incident Angle (º): 0, 10, 20, 30**	**Maximum Illumination Angle (º): 10, 20, 45**	**Level of Noise (%): 25, 50, 100**
Stylia Outcrop	f: 20 Hz, 40 Hz MIA: 45º θ: 20º	MIA: 45º θ: 20º	MIA: 45º f: 20 Hz	θ: 20º f: 20 Hz	θ: 20º MIA: 45º f: 20 Hz
Cross-Section (B)	None	MIA: 45º θ: 20º	MIA: 45º f: 20 Hz	θ: 20º f: 20 Hz	θ: 20º MIA: 45º f: 20 Hz
Cross-Section (C)	None	MIA: 45º θ: 20º	MIA: 45º f: 20 Hz	θ: 20º f: 20 Hz	θ: 20º MIA: 45º f: 20 Hz

A total of four variations of the geological model were modelled to investigate the impact of different interpretations and scales (Fig. 5.3):

- Stylia 1A (fig 5.3a) represents the base case of the seismic modelling study, and the full extent of the Stylia outcrop.

- Stylia 1B (fig 5.3b) represents the Stylia outcrop focused on the channel-complex, modelled for comparison with Stylia 2 and Stylia 3

- Stylia 2 (Fig. 5.3c) represents a case in which tabular, laterally extensive conglomerate-sheets similar to those observed below the channel-complex also occur above the channel-complex, to investigate the impact of a more complex surrounding stratigraphy.

- Stylia 3 (Fig. 5.3c) represents an interpretive case where the upper two conglomerate units of the channel-complex show a gradual transition into mudstones rather than the pinching-out trend illustrated in the base case. The reasoning behind this case was the uncertainty of the primary interpretation because of extensive coverage of vegetation and a lack of exposed outcrop in the specific area. Stylia 3 was modelled to investigate how small variations in stratigraphic architecture may affect seismic images.

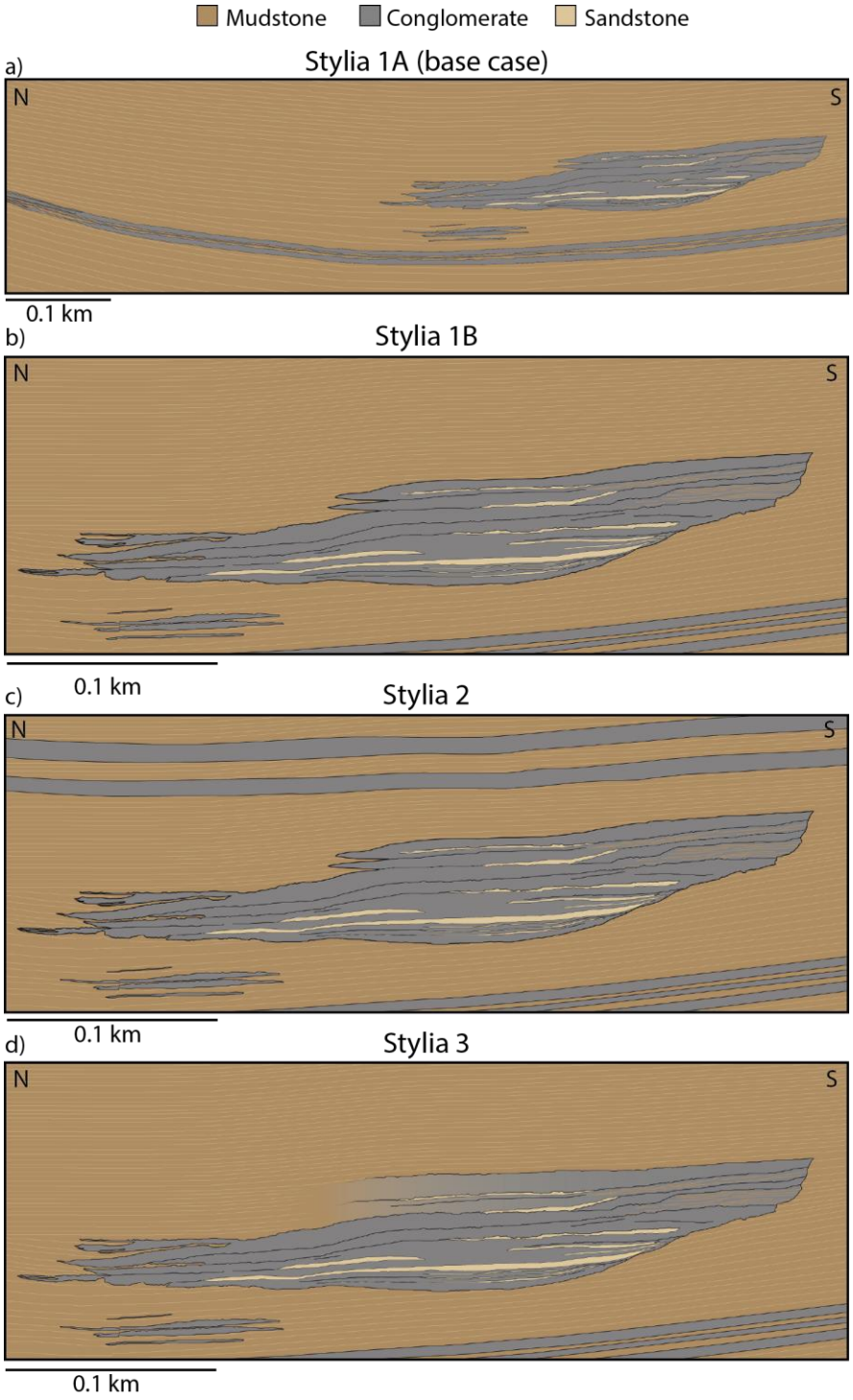

Figure 5.4: Variations of the Stylia outcrop geological model.

6. Results

This chapter presents the results from the photogrammetric virtual outcrop modelling, geological interpretation and sensitivity analyses on modelled seismic. Firstly, the VOM and geological interpretation will be presented, followed by the geological models for regional cross-sections. Finally, a selection of the synthetic seismic images generated for various sensitivity analyses will be presented.

6.1 Regional cross-sections

Cross-section B and C illustrate a Rethi-Dendro formation channel system in a significantly larger-scale setting compared to that of the Stylia model. To create geological models fit for input in seismic modelling, each depositional unit of the RDF described by Muravchik et al. (2020) had to be assigned a dominant lithology of either mudstone, sandstone or conglomerate. Based on information from fig 5.2, the following was determined:

- Pellini Fm, Ano Pitsa Fm and Unit 7, 8, 10, 13 & 16 are dominantly sandstones
- Unit 3 is dominantly sandstones with conglomerate channel belts
- Slide sheets are dominantly sandstones, with thin mudstone beds along slip surfaces
- Unit 2, 4, 5, 6, 9, 12 & 15 are dominantly conglomerates
- Unit 1, 11 & 14 are dominantly mudstones

To emphasize the stratigraphy within unit 1, two different mudstone variations were defined. The complete geological models for cross-section B and cross-section C are illustrated in fig. 6.6 and 6.7

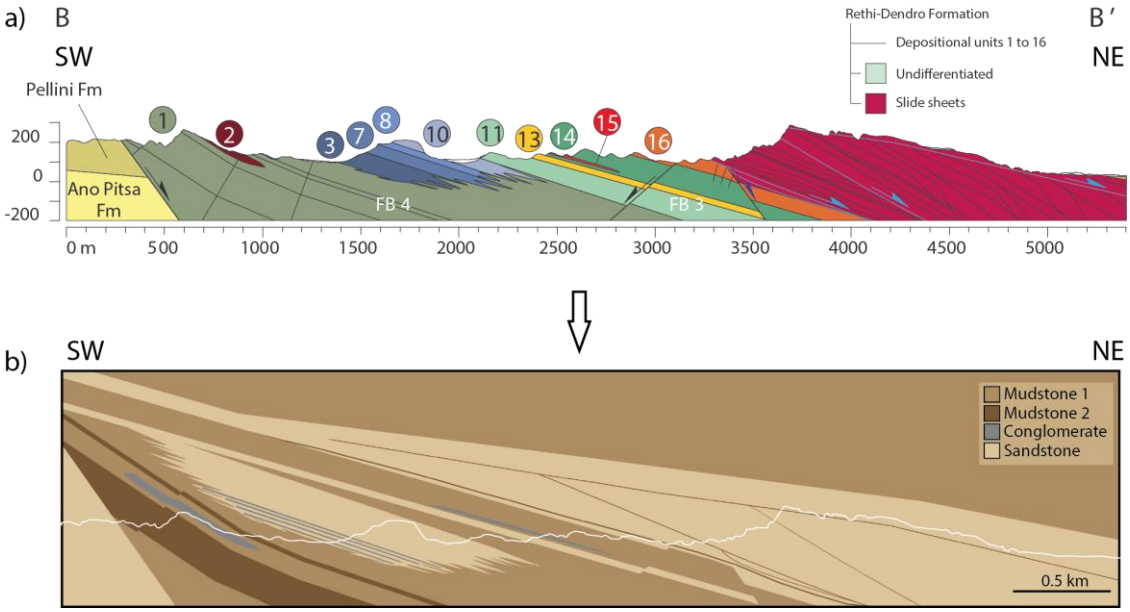

Figure 6.6: Cross-section B. a) Original cross-section from Muravchik et al. (2020). b) Geological model populated with dominant lithologies from each depositional unit. White line marks the topography to illustrate where extrapolation starts.

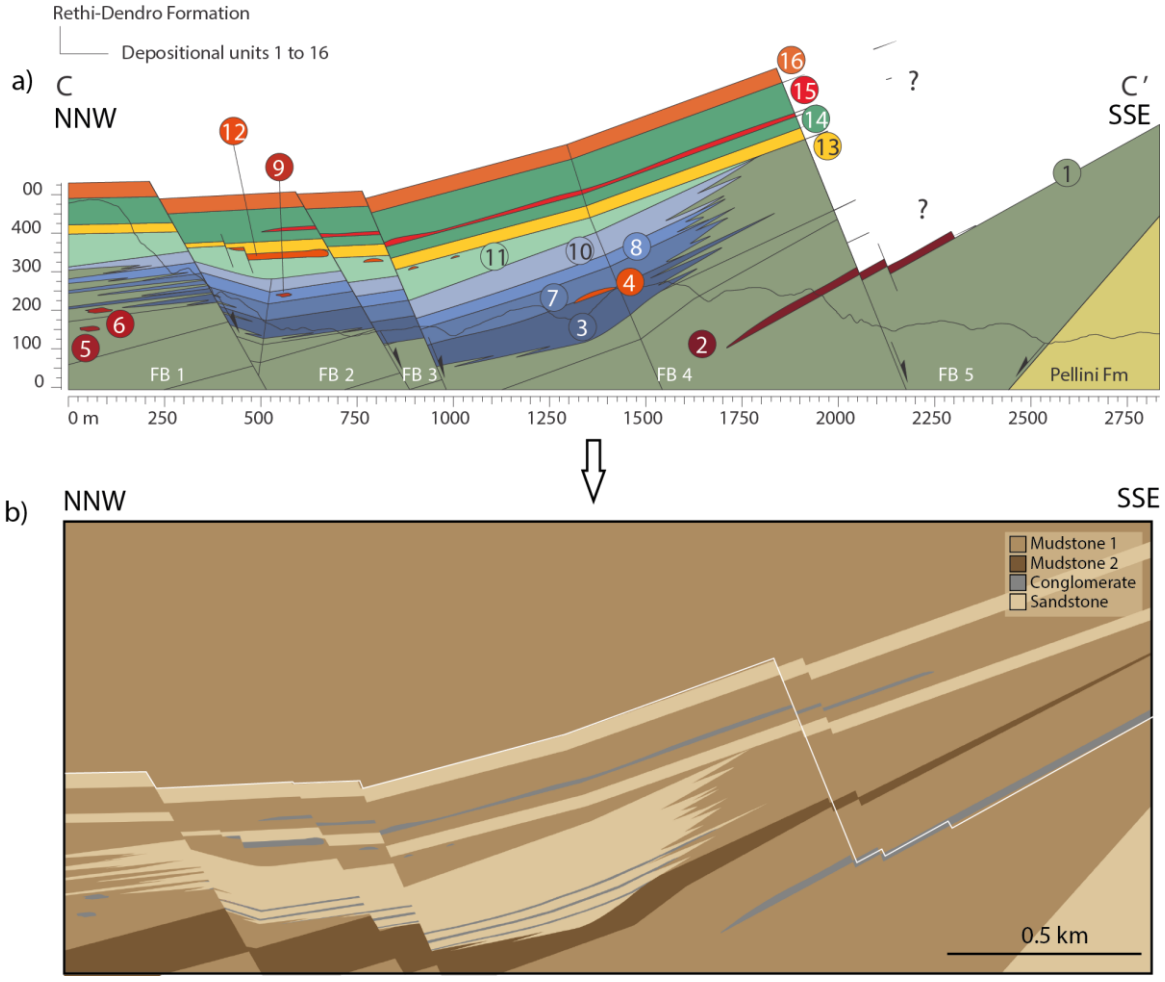

Figure 6.7: Cross-section C. a) Original cross-section from Muravchik et al. (2020). b) Geological model populated with dominant lithologies from each depositional unit. White line marks the outline of the original cross-section to illustrate where extrapolation starts.

6.2 Geological interpretation of the Stylia VOM

In this study, a VOM was constructed for the Stylia outcrop using photogrammetry. The workflow behind this process was presented in chapter 5. Due to its large file size, the VOM was split into two separate LIME projects for the subsequent geological interpretation. The northern and the southern half were then interpreted individually. The purpose of the interpretation was to create a detailed geological model including stratigraphic architecture, rock-body geometries and boundary surfaces to use as input for 2D PSF-based convolution modelling.

Fig. 6.1 and 6.2 illustrates the process from VOM to geological model for the northern (6.1) and southern (6.2) part of the Stylia outcrop. Primary observations in LIME included mapping out major surfaces marked in red, minor surfaces marked in blue, and other significant details marked in yellow, following the workflow as described in chapter 5.3. Where the outcrop was covered by vegetation, or the aerial extent of the outcrop hindered further observations, extrapolation and interpolation of the surfaces was carried out and lithologies were assigned to produce a complete geological model.

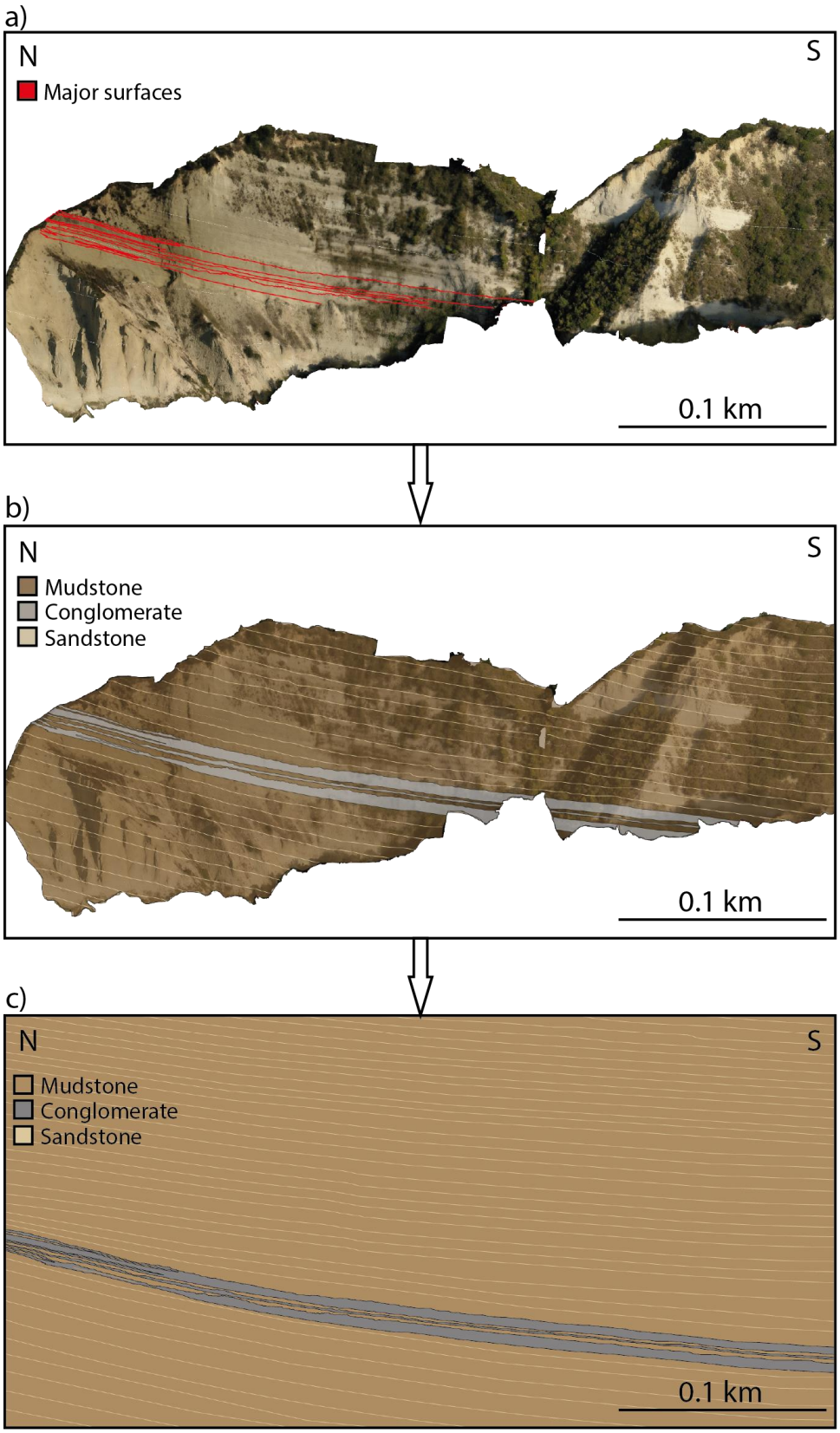

Figure 6.1: From VOM to geological model of the northern Stylia outcrop. a) VOM with primary observations only comprising major surfaces. b) Interpolation of observational surfaces to produce the outcrop interpretation. Lithologies have been assigned to the corresponding rock bodies. c) Complete geological model extrapolated to fit the rectangular frame needed for seismic modelling.

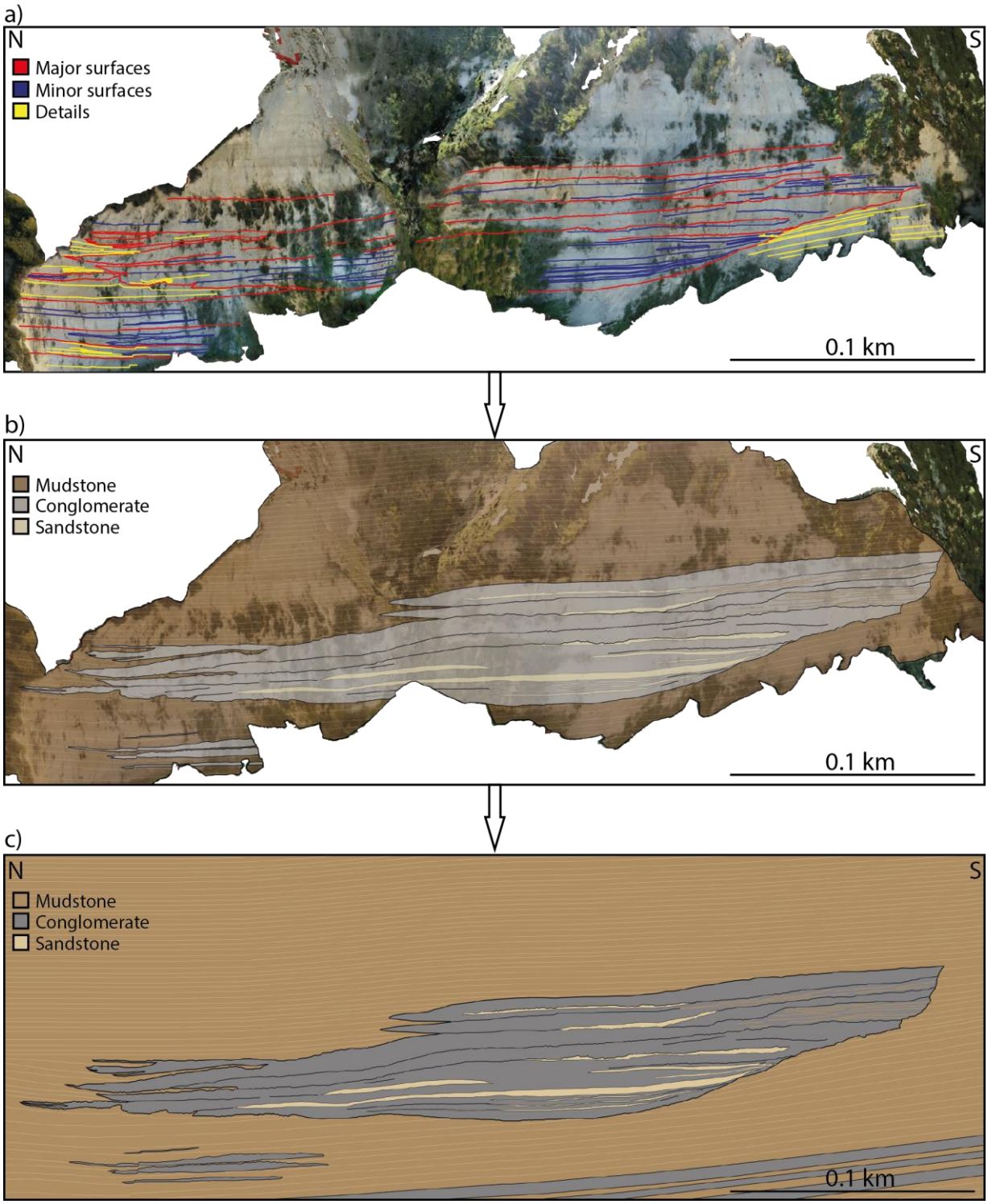

Figure 6.2: From VOM to geological mode of the southern Stylia outcrop. a) Primary observations comprising major surfaces (red), minor surfaces (blue) and details (yellow). b) Interpolation of observational surfaces to produce the outcrop interpretation. Lithologies have been assigned to the corresponding rock bodies. c) Complete geological model extrapolated to fit the rectangular frame needed for seismic modelling.

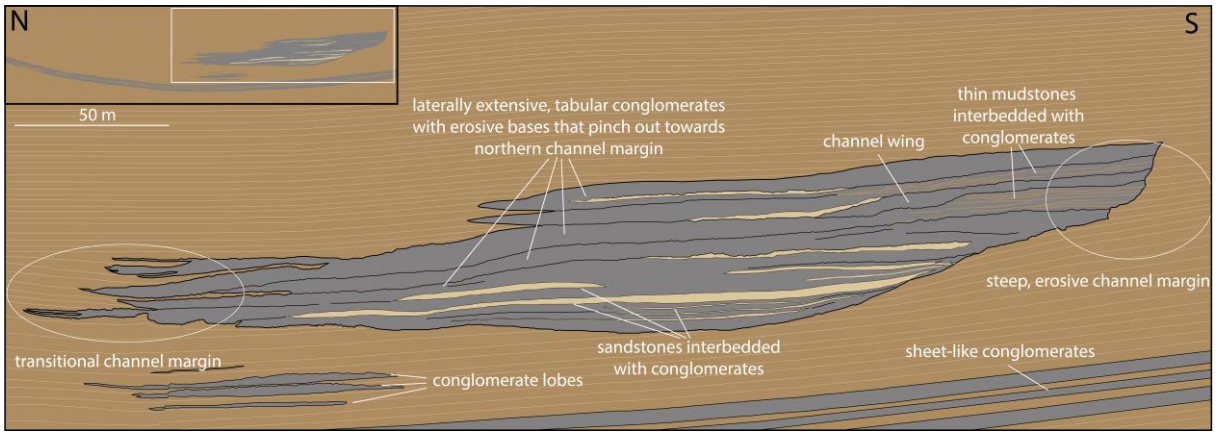

Figure 6.3: Final interpretation of the Stylia VOM.

6.2.1 Description of architectural framework

The key observation of the Stylia VOM comprises a coarse-grained channel complex dominated by conglomerates that are either vertically stacked, amalgamated or interbedded with finer grained units (Fig. 6.3). External features include an overall concave up shape and flat top, with a maximum width of ~375 m and a maximum thickness of ~45 m.

The channel complex is asymmetrical channel margins of different architectures. The southern margin is sharp, steep-sided and unconformable, whereas the northern margin has a more transitional character where individual conglomerate beds pinch out towards north and interlayer with mudstones.

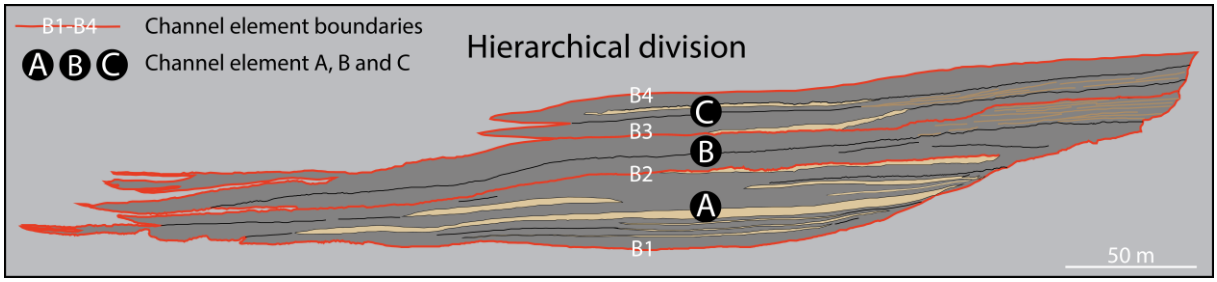

Figure 6.4: Hierarchical division of the channel complex. Black circles mark the three channel elements (A), (B) and (C), and red lines correspond to channel element boundaries.

The channel complex was sorted into a hierarchy of 3 separate channel elements comprising a number of channel stories as illustrated in fig. 6.4. (McHargue et al., 2011). The hierarchical division was determined based on major vertical changes in stratigraphic architecture and lithologies.

Channel element (A) has a lenticular shape, maximum width of 335 m and a maximum thickness of 25 m. The internal stratigraphic architecture comprises laterally extensive conglomerate beds that are mostly tabular in shape, have irregular bases in some areas and pinch out towards the northern channel margin. The conglomerates are interbedded with 0.3- to 3-m thick sandstone beds that tend to pinch out in both directions (Fig. 6.5a). In the northern part of the base surface (B1), tight folded structures are observed between mudstones and conglomerates (Fig. 6.5d). Channel element (B) has a maximum width of 370 m and a maximum thickness of 17 m. It is dominated by the same conglomerate beds as in (A), but sandstone beds are absent. One channel storey in the far southern end contains thin mudstones of <30 cm thickness interbedded with the conglomerates and have an erosive top. The uppermost channel element (C) is narrower, with a maximum width of 217 m and a maximum thickness of 14 m. Channel element (C) comprises a stratigraphic architecture more complex than in (A) and (B), which from north to south can be distinguished by two major conglomerate units interbedded with thinner sandstone lenses, which splits into three units in the south. The southern units comprise an asymmetrical channel wing at the base which is thin in the south and erodes down into underlying stratigraphy getting progressively thicker toward north before it pinches out (fig 6.5e). The middle unit comprises the same thin <30 cm mudstones intercalated with conglomerates as in (B), and the top unit comprise a tabular laterally extensive conglomerate bed.

The surrounding stratigraphy of the channel complex is dominated by parallel laminated mudstones interbedded with thin sandstone layers of <30 cm. Below the channel complex, isolated and narrow conglomerate lobes and more laterally extensive tabular conglomerate sheets are observed. The conglomerate lobes have flat bases and slightly convex tops, and have a maximum thickness of 3.7 m. The conglomerate sheets have a maximum thickness of 6 m, whereas the width is unidentified as it exceeds the lateral extent of the outcrop.

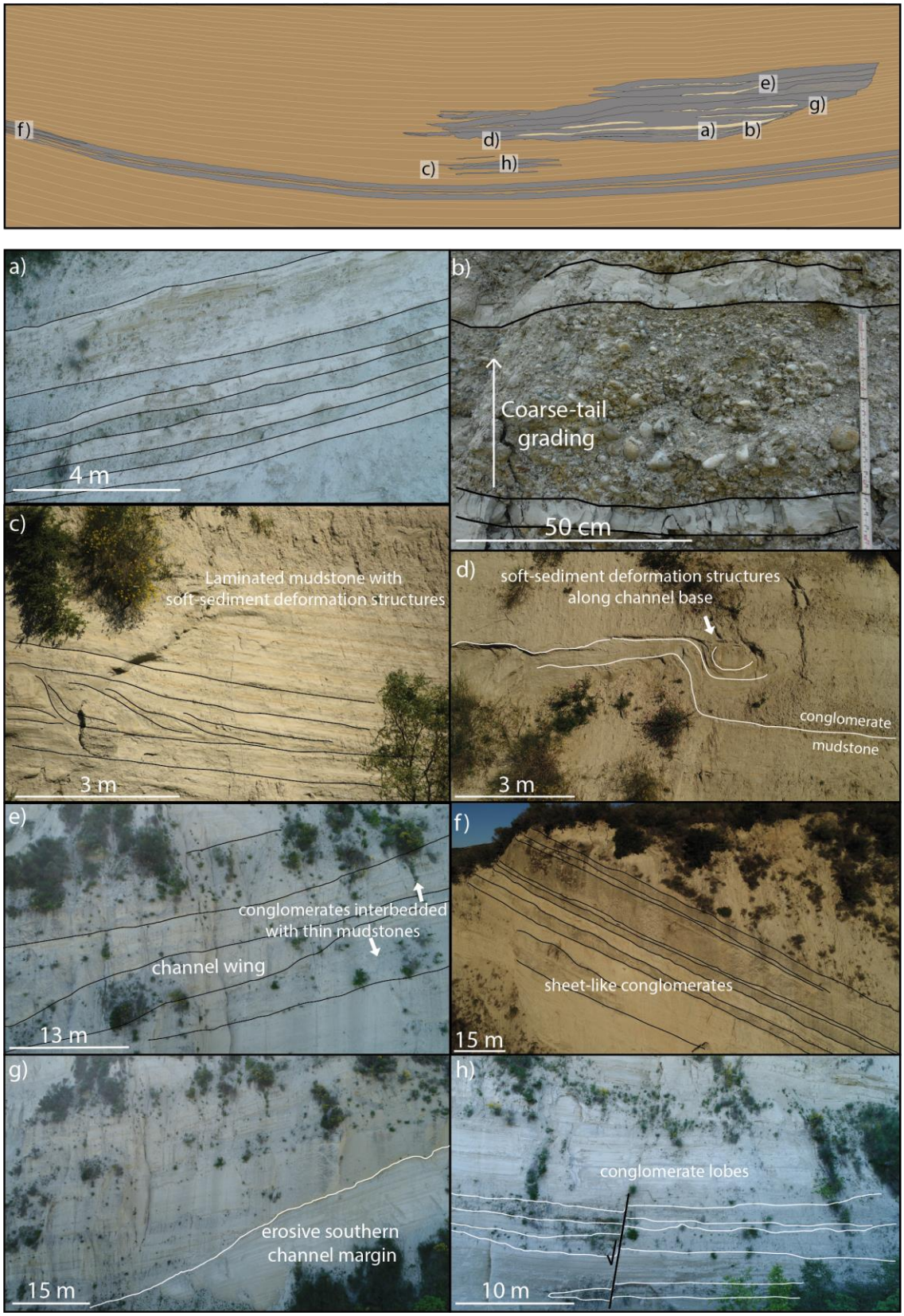

Figure 6.5: Photographs of the lithologies, structures and architectural elements found in the Stylia outcrop. a) sandstone beds within channel element (A), b) Sandy-matrix supported conglomerate with coarse-tail normal grading, c) laminated mudstones with soft-sediment deformation structures, d) soft-sediment deformation structures along channel base, e) stratigraphic architecture of upper southern channel complex, f) sheet-like conglomerates below the channel complex, g) steep-sided erosional southern channel margin, h) conglomerate lobes below the channel complex.

6.2.2 Lithological framework: observation and interpretation

Due to restricted sedimentological details available from the outcrop model, the lithological framework defined for the Stylia VOM is confined to three simplified lithologies, i.e., conglomerates, mudstones, and sandstones. The limited information makes it difficult to determine the exact type of processes responsible for deposition. However, based on previous literature concerning deep-water sedimentation, it is safe to assume that the coarse-grained channel fill could have been deposited by e.g., sediment gravity flows or mass transport processes, and the surrounding mudstones are likely to be deposited by hemipelagic sedimentation (e.g. Nemec, 1990, Normark, 1970, Stow and Mayall, 2000, Talling et al., 2012).

Some sedimentological details from the VOM can still be observed, which can enhance the understanding of the flow state of the depositional processes. The channel complex fill is mainly dominated by conglomerates supported by a sand-rich matrix (Fig. 6.5b). The lack of mud in the conglomerate matrix makes it non-cohesive, implying that if deposited by a debris flow it would be a non-cohesive debrite (Talling et al., 2012). The individual conglomerate beds also show a slight fining upwards trend. Normal grading is typical for turbidites but could also occur in debrites when outsizes clasts settle at the base of the deposit (Nemec, 1990, Talling et al., 2012). The type of normal grading observed in this case is similar to coarse-tail grading, where only the larger clasts tend to fine upwards (Middleton and Hampton, 1973). No traction structures such as cross bedding was observed in the VOM, indicating that the flow most likely was not fully turbulent. The more plausible interpretation is an intermediate between turbulent and laminar flow state.

Plane-parallel laminated mudstones interbedded with thin <30-cm sandstone beds dominate above and below the channel (Fig. 6.5c). The mudstones are often observed containing tightly folded structures, interpreted as soft-sediment deformation structures like e.g. water escape structures (Lowe, 1982). These deposits are interpreted as hemipelagic mud deposited by grains settling from suspension in the water column, and the thin sandstones can be interpreted as Tc/Td or Te division turbidites (Talling et al., 2012). Mud in the deep water can also derive from the most dilute part of a turbidite deposit. In this case, this is unlikely due to the great thicknesses of the mudstone deposits. However, the two are hard to distinguish without further field investigation. Thinner mudstones <50 cm also appear interbedded with thicker conglomerates in channel element (B) and (C). These are more difficult to define as either hemipelagic- or turbidite mud due to their thickness and lack of detail in the VOM. In addition

to the thin sandstones interbedded with mudstone, thicker sandstone beds between 0.3 and 3 m appear in channel element (A) and (C) (Fig. 6.5a). They mostly have lenticular and lobate shapes and tend to follow the underlying topography, indicating non-erosive conditions in the flow.

6.2.3 Final interpretation of the Stylia VOM

The stratigraphic architecture described for the Stylia outcrop model indicates a multi-episodic coarse-grained channel complex switching between erosion and deposition. The asymmetrical external shape of the channel complex along with the two different margin architectures could imply some level of sinuosity within the channel, where the southern outer bend was more erosive whereas the northern inner bend was more depositional (Kolla et al., 2007). The channel elements are generally aggrading, but the lateral extension and architecture of the upper channel element (C) also implies a slight lateral migration of the channel. The channel fill comprises gravity flow deposited sandy-matrix conglomerates that are either vertically stacked, amalgamated, or interlayered with finer grained units of sandstone or mudstone. Surrounding the channel complex, hemipelagic mudstones interbedded with thin sandy turbidites dominate, with occasional narrow conglomerate lobes and laterally extensive tabular conglomerate sheets occurring below the channel (Fig. 6.3).

6.3 Seismic modelling results

In this subchapter, the results the sensitivity study performed on synthetic seismic will be presented. The intentions of the seismic modelling experiment were to investigate the seismic signature of syn-rift deep-water channel complexes, and to determine the impact of various geophysical parameters as well as various geological models on the 2D seismic images. A total of 60 synthetic seismic images were generated using 2D PSF-based convolution modelling, testing the impact of the following parameters:

1. Dominant frequency
2. Level of noise
3. Maximum illumination angle (MIA)
4. Incident angle (θ)
5. Elastic properties from wells at different locations

6 different geological models were produced for input models in the sensitivity analyses, including 4 versions of the Stylia outcrop (fig 5.4) and 2 regional cross-sections from the Corinth Rift (fig. 6.6 and 6.7) The majority of seismic modelling of the Stylia VOM was done on a base case, namely Stylia 1A (fig 5.4a). When producing synthetic seismic images for the different geological variation models (Stylia 2 & 3), Stylia 1B was modelled as a comparative model. Standard input parameters in seismic modelling are defined in Table 6.1. For easy comparison and to resemble realistic conventional seismic, a standard frequency of 20 Hz was used. A maximum illumination angle of 45º was also used, as it corresponds to standard seismic illumination (Rabbel et al., 2018). Incident angles of conventional seismic typically range from about 5 to 40-50º (below critical angle), which is why an intermediate incident angle of 20º was used as a standard, following Faleide et al. (2021). The elastic properties are derived from well 6406/12-3B in the Fenja field offshore Norway.

Table 6.1: Standard input parameters for seismic modelling.

Wavelet	20 Hz Ricker-wavelet
Maximum illumination angle	45º
Incident angle	20º
Average P-wave velocity in models	4 km/s

6.3.1 Changing the dominant frequency

The frequency band of a seismic wavelet is one of the geophysical parameters with the most impact on seismic resolution. This section will present the results of changing the dominant frequency for 3 of the geological models, i.e., Stylia 1A, Cross-section B and Cross-section C. In this study, synthetic seismic images were modelled using both a conventional seismic frequency (20 Hz) and high-resolution frequencies (40, 60 and 140 Hz). For simplicity, only Ricker-wavelets were used. Ricker-wavelets are often favoured because of their simple relation between dominant frequency and wavelet width (Ryan, 1994). A constant incident angle of 20º and maximum illumination angle of 45º were kept constant in the present section. The corresponding PSFs are presented in Fig 6.8, a PSF being the PSDM point-scatterer response, i.e., showing the seismic-imaging footprint of each reflectivity spike, including resolution and illumination effects.

Figure. 6.9 shows Stylia 1A (Fig 6.9a) modelled with a range of dominant frequencies. The high contrast in elastic impedance between mudstones and conglomerates produces a strong reflectivity (Fig 6.9b) which enables the clear detection of the Stylia channel complex in all seismic images with increasing level of detail for higher frequencies. Similarly, the laterally extensive conglomerate sheets below the channel complex are highly detectable in contrast to the surrounding mudstones due to the same strong reflectivity.

At conventional seismic frequency (20 Hz, Fig. 6.9c), only the top and base surface of the channel complex can be distinguished as a positive high amplitude reflection and negative high amplitude reflection, respectively, as well as the extensive conglomerate sheets below the channel complex. The lenticular, concave shape of the channel complex is not well imaged and appears more horizontal than in reality.

The rather low frequency causes interferences between closely spaced reflectors, making the internal thinner layers and geometries of the channel complex impossible to resolve as they fall under seismic resolution. Along the top of the seismic image, a horizontal weakly positive reflection stems from model-truncation effects (thus artefact) due to the rectangular frame of the image and should not be interpreted here; if the model had been extended, that effect would have been removed.

When the frequency is increased to 40 and 60 Hz, seismic resolution and detectability also increase (Fig 6.9d & 6.9e). Two medium-amplitude reflections can be observed between the upper and lower channel complex boundaries, indicating the existence of some internal stratigraphy within the channel complex. However, not all reflectors are illuminated, and individual layers require higher resolution frequencies to be resolved. The isolated conglomerate lobes below the channel can be detected first at 40 Hz, as one laterally inextensive strong positive reflection. At a frequency of 60 Hz, the heterogeneity of the surrounding lithologies, i.e., mudstones interbedded with thin sandstones can be imaged as low amplitude, continuous reflections.

At 140 Hz, a significantly increased amount of detail can be imaged within the channel complex. Some of the sandstone beds can be detected as medium amplitude reflections, but not all individual reflectors are illuminated. The contrast in elastic impedance between sandstones and conglomerates is lower than that of mudstones and conglomerates, explaining the weaker seismic amplitudes of the sandstone layers due to low reflectivity. Even with the highest frequency tested, the channel complex cannot be fully resolved in seismic images.

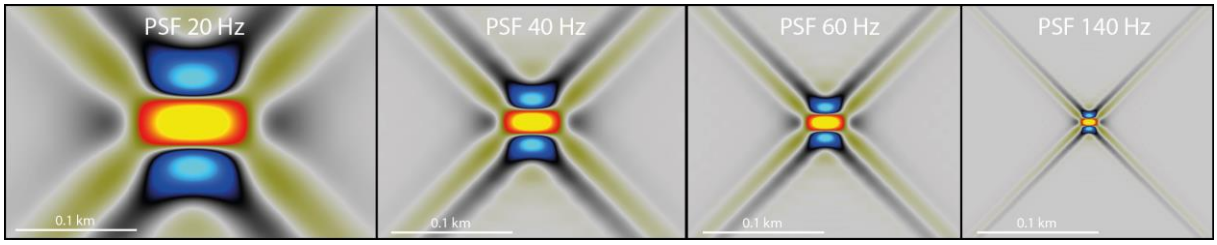

Figure 6.8: PSFs for the synthetic seismic images in fig. 6.9, indicating the 2D seismic resolution of the seismic images.

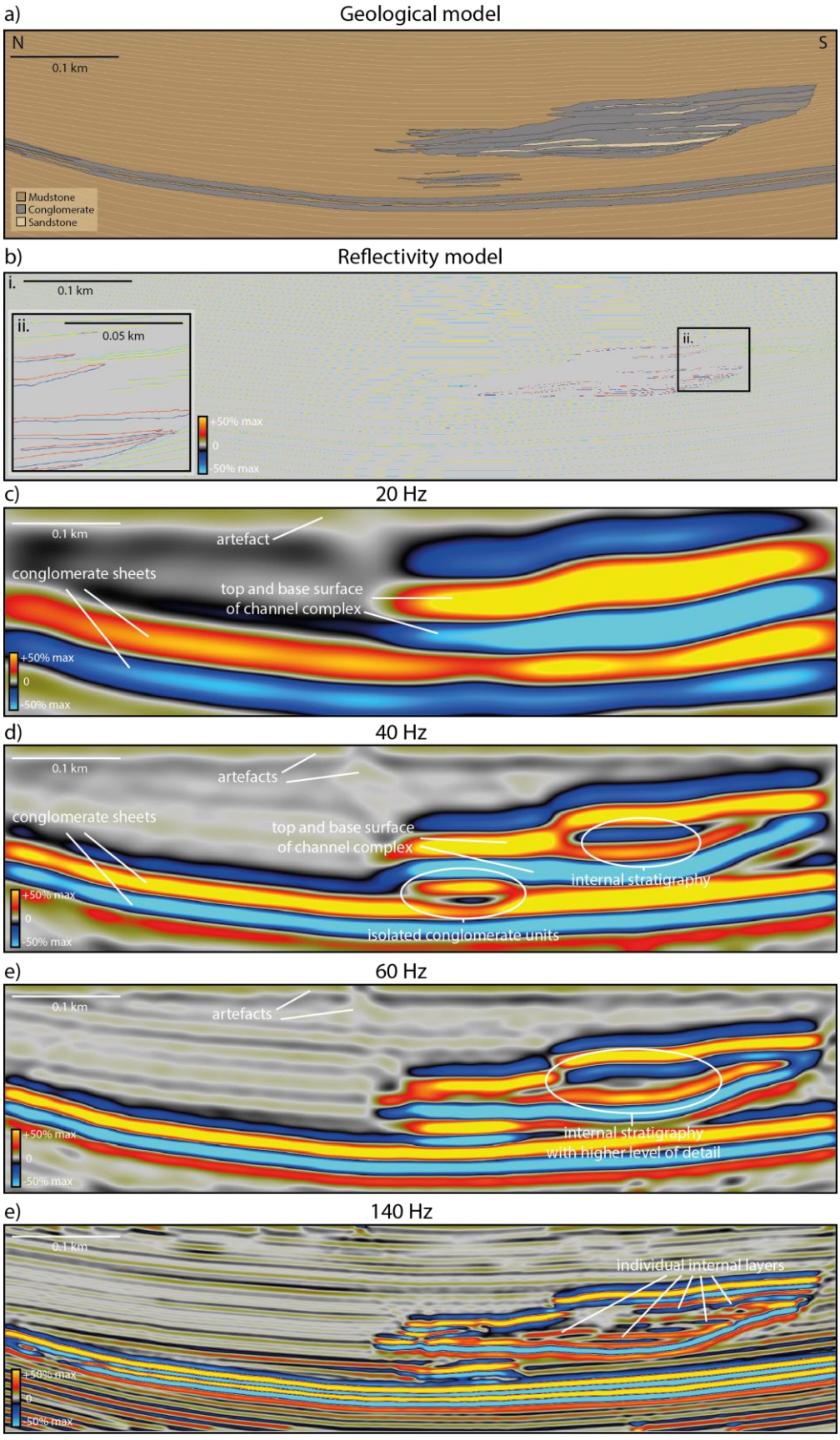

Figure 6.9: Synthetic seismic images of Stylia 1A with different dominating frequencies ranging from 20 – 140 Hz. The colour bar illustrates the relative colour scale of amplitudes, with maximum amplitudes of + and – 50%.

Figure 6.10 and 6.11 show cross-section B and cross-section C modelled with varying frequencies, still with a maximum illumination angle of 45º and an incident angle of 20º. These models illustrate a syn-rift deep-water channel system in the Rethi-Dendro formation of a significantly larger scale compared to that of the Stylia model. The models also contain a lower level of detail. The external shape of the channel system can be detected with high confidence in all the synthetic seismic images. The internal 10-20 m thick conglomerate channel belts near the base of the channel system produce medium amplitude reflectors (Fig 6.10b and 6.11c). At 20 Hz and 40 Hz, these are detected as weak reflections but one does not fully resolve individual layers. From 60 Hz to 140 Hz however, these channel belts are close to fully resolved.

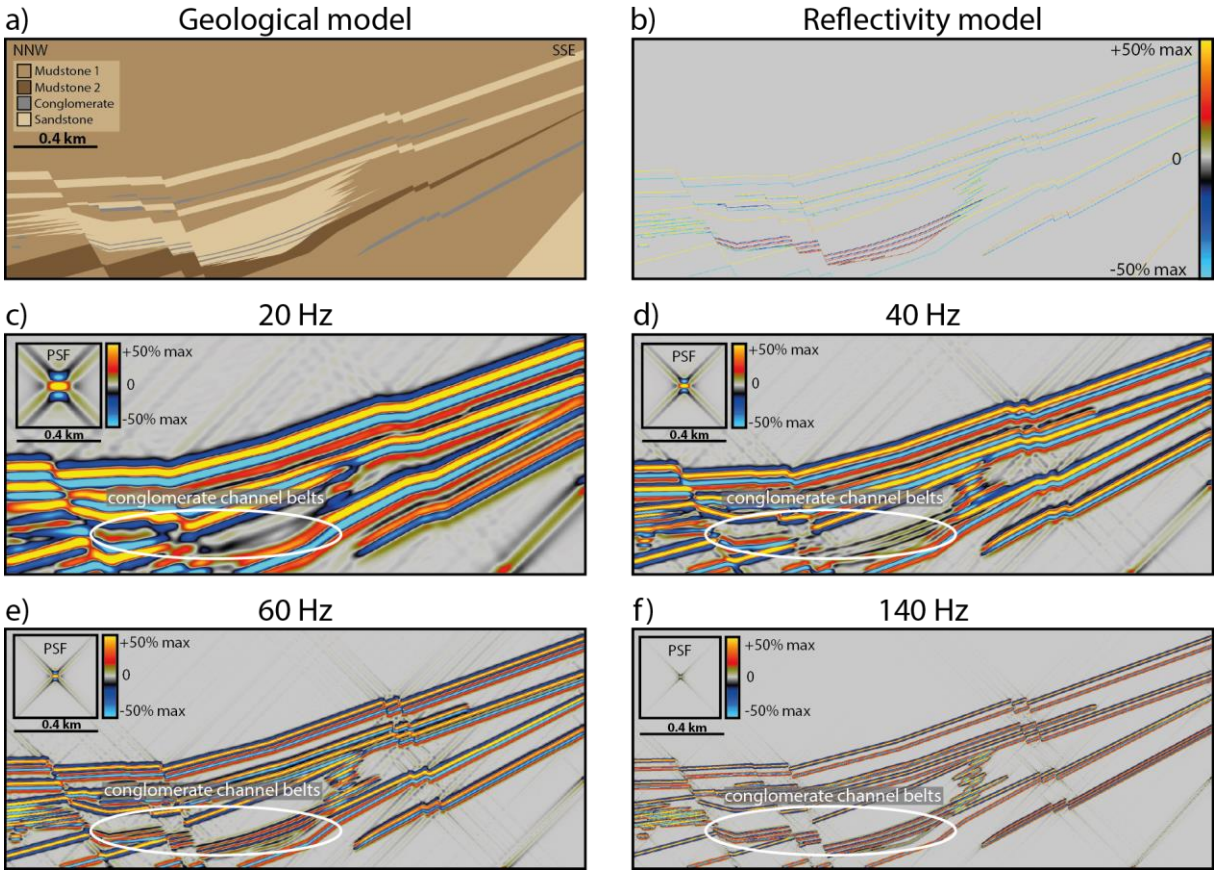

Figure 6.10: Synthetic seismic images of Cross-section C with varying frequencies ranging from 20 – 140 Hz.

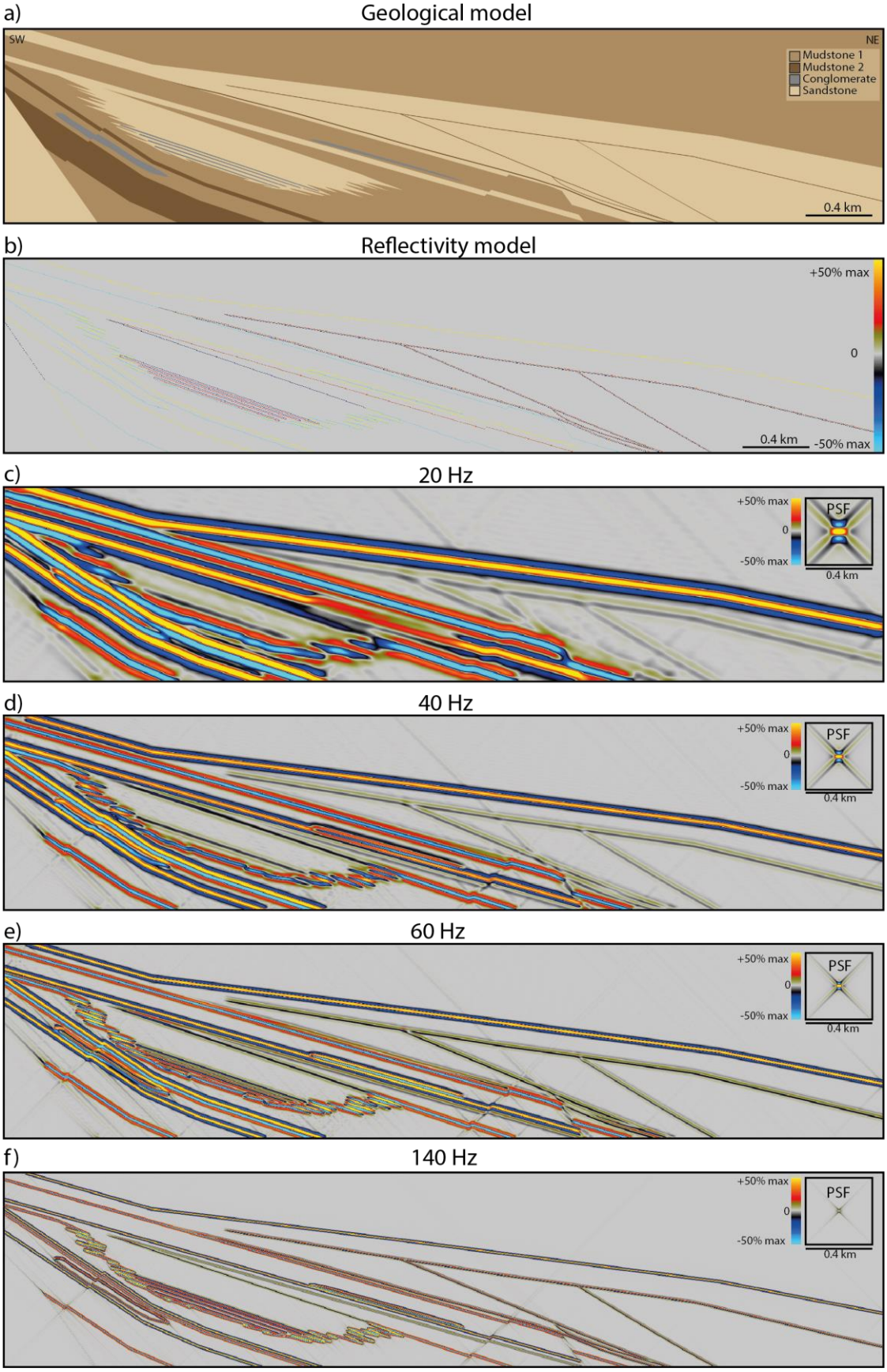

Figure 6.11: Synthetic seismic images of Cross-section B with varying frequencies ranging from 20 – 140 Hz.

6.3.2 Adding noise

The synthetic seismic images become more realistic by applying random noise (white noise in input but PSDM-coloured before being added to the modelled seismic; (Lubranol-Lavadera et al., 2019), as real seismic data comprises a combination of noise and signal. To investigate the impact of noise on deep-water channel complexes, four levels were tested, including 0%, 25%, 50% and 100% noise. The results from the Stylia 1A and 1B model as well as cross-section B will be presented in the following.

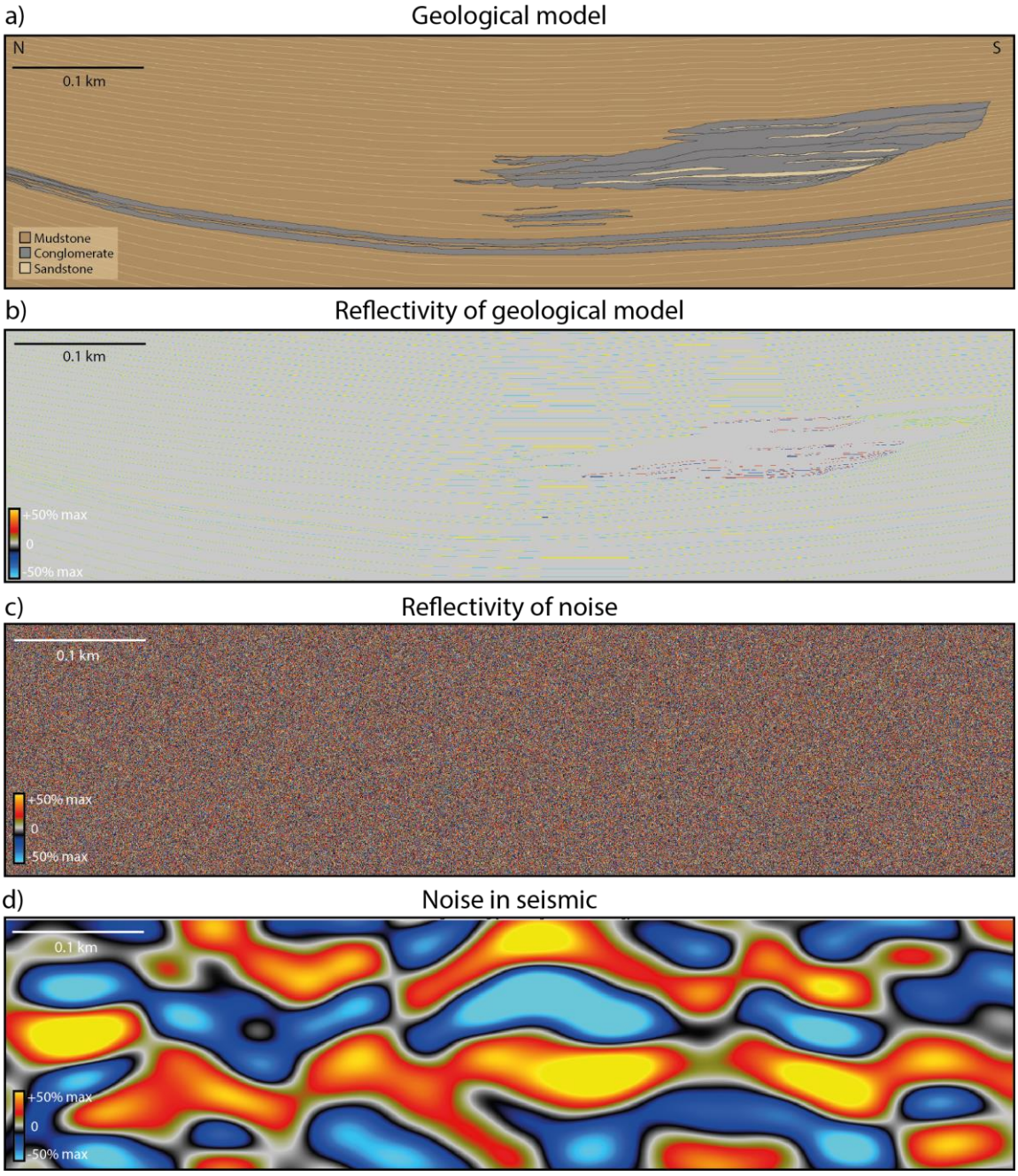

Figure 6.12: a) Stylia 1A geological model, b) reflectivity model of Stylia 1A, c) reflectivity model of coloured random noise, d) seismic image of noise, corresponding to reflectivity model c)

Figure 6.12 illustrates the reflectivity and seismic (PSDM) signature of the noise model for Stylia 1A. The effect of different noise levels corresponding to the seismic image in fig. 6.12 is displayed in fig. 6.13. All cases are modelled with a frequency of 20 Hz, maximum illumination angle of 45 º and an incident angle of 20º. At 0% noise, the seismic image is equal to that of fig. 6.9c. The key observation is that increasing the level of noise results in a more chaotic seismic signature, as expected. The top and base of the channel complex can still be detected, but the shape of the reflection is distorted at 100% noise. From 25% to 50% noise, the sheet-like conglomerates are still detectable, but progressively get less continuous. At 100% noise, the surrounding stratigraphy is almost entirely masked by the noise, resulting in low to medium amplitude discontinuous reflections.

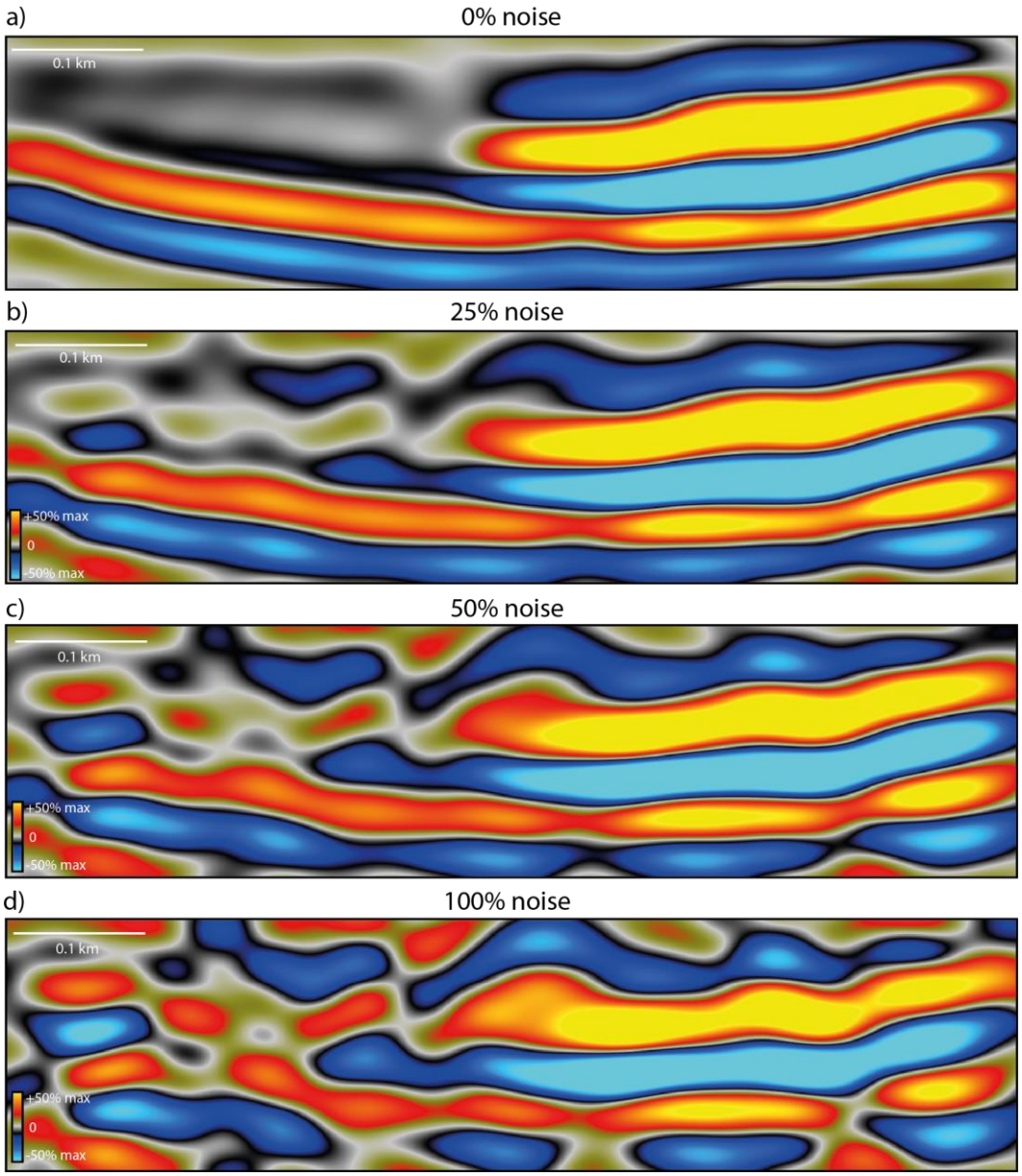

Figure 6.13: Stylia 1A modelled with an increasing level of random coloured noise (0%, 25%, 50% and 100%).

Fig 6.14 explores the effect of noise on the channel complex model with a higher frequency (40 Hz). It shows that the channel is easily detectable at all noise levels, and the same applies for the internal stratigraphy reflections and the conglomerate lobes reflections. The surrounding stratigraphy gets progressively more chaotic, just like in the lower frequency model. In fig. 6.16, the impact of noise on cross-section B shows the same trend as previously observed, where the low amplitude reflectors get masked by progressively increasing noise levels.

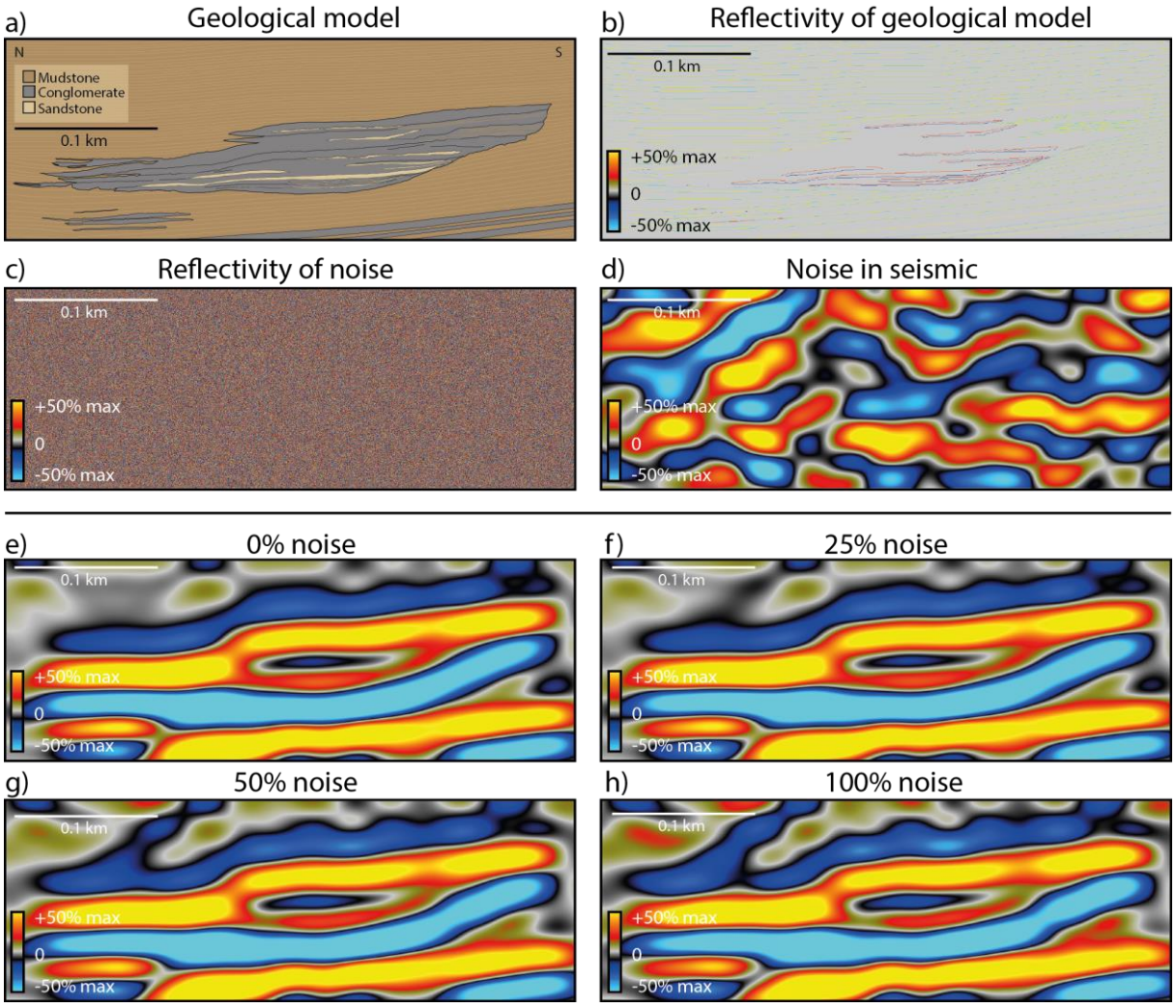

Figure 6.14: Stylia 1B modelled with increasing levels of noise, with a constant dominating frequency of 40 Hz.

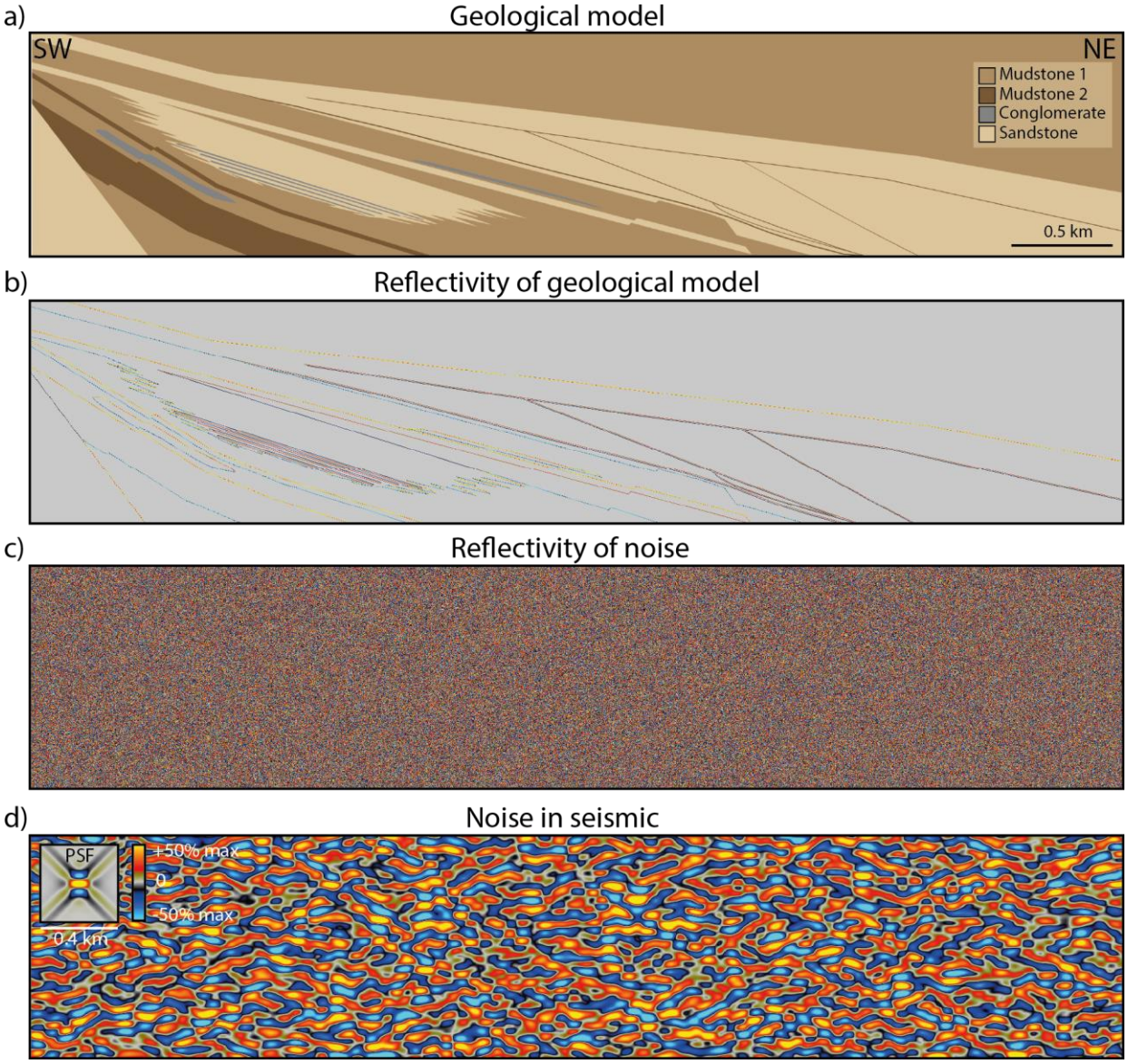

Figure 6.15: a) Cross-section B geological model, b) reflectivity model for Cross-section B, c) reflectivity model of coloured random noise, d) seismic image of noise, corresponding to reflectivity model c)

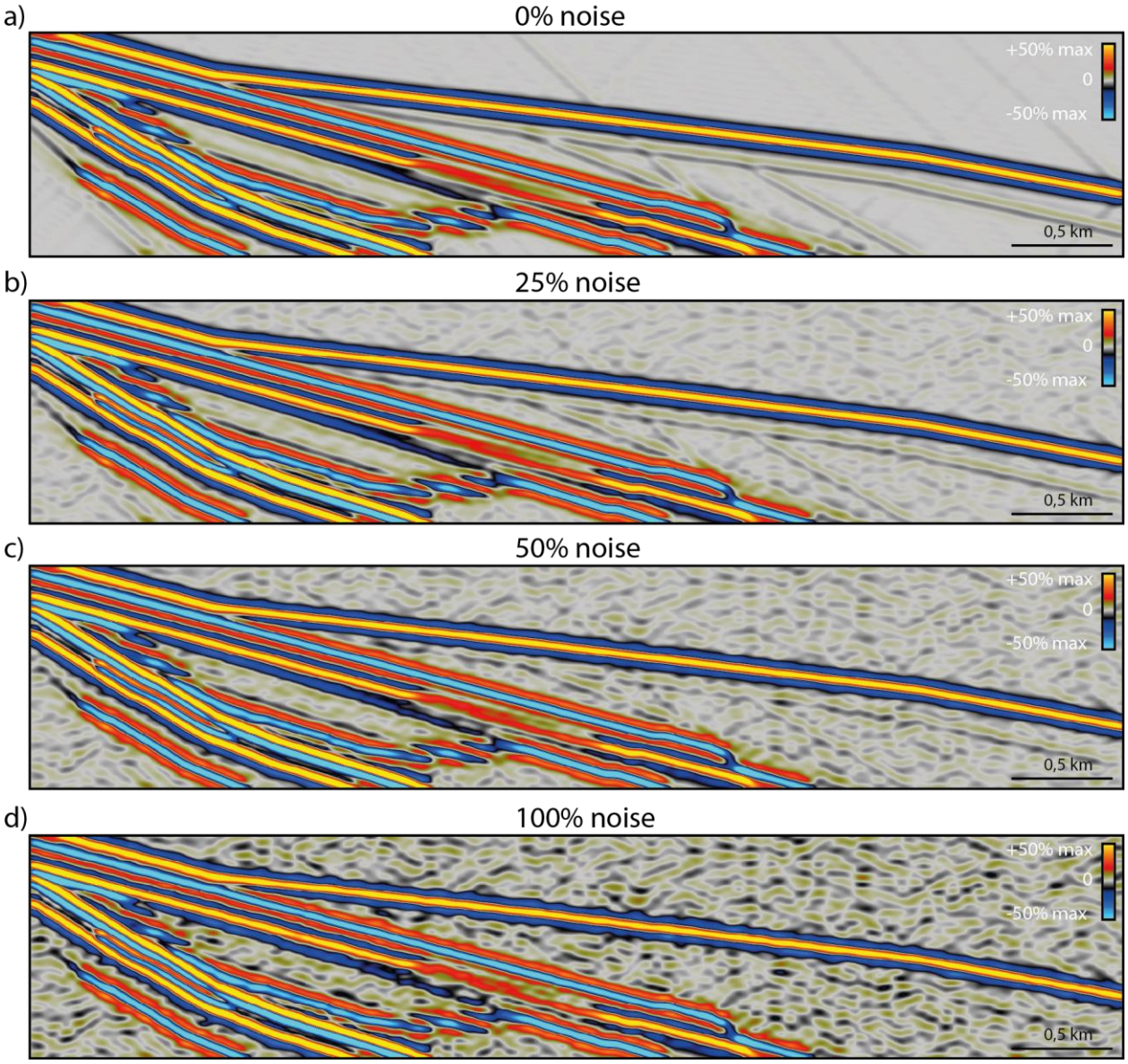

Figure 6.16: Synthetic seismic images of Cross-section B modelled with an increasing level of random coloured noise (0%, 25%, 50% and 100%).

6.3.3 Changing the maximum illumination angle

The stratigraphy of both the Stylia outcrop and the cross-sections is mostly non-horizontal, and they comprise both gently dipping and steeply dipping strata. The angle of maximum illumination is therefore a significant parameter to explore because it impacts the seismic signature, determining how well the dipping reflectors are illuminated as well as affecting lateral resolution. A constant frequency of 20 Hz and incident angle of 20º was applied for all cases. To explore the impact of illumination, three maximum illumination angles were tested, i.e., 10º, 20º and 45º. In this section, results from the Stylia 1A and cross-section C models will be presented.

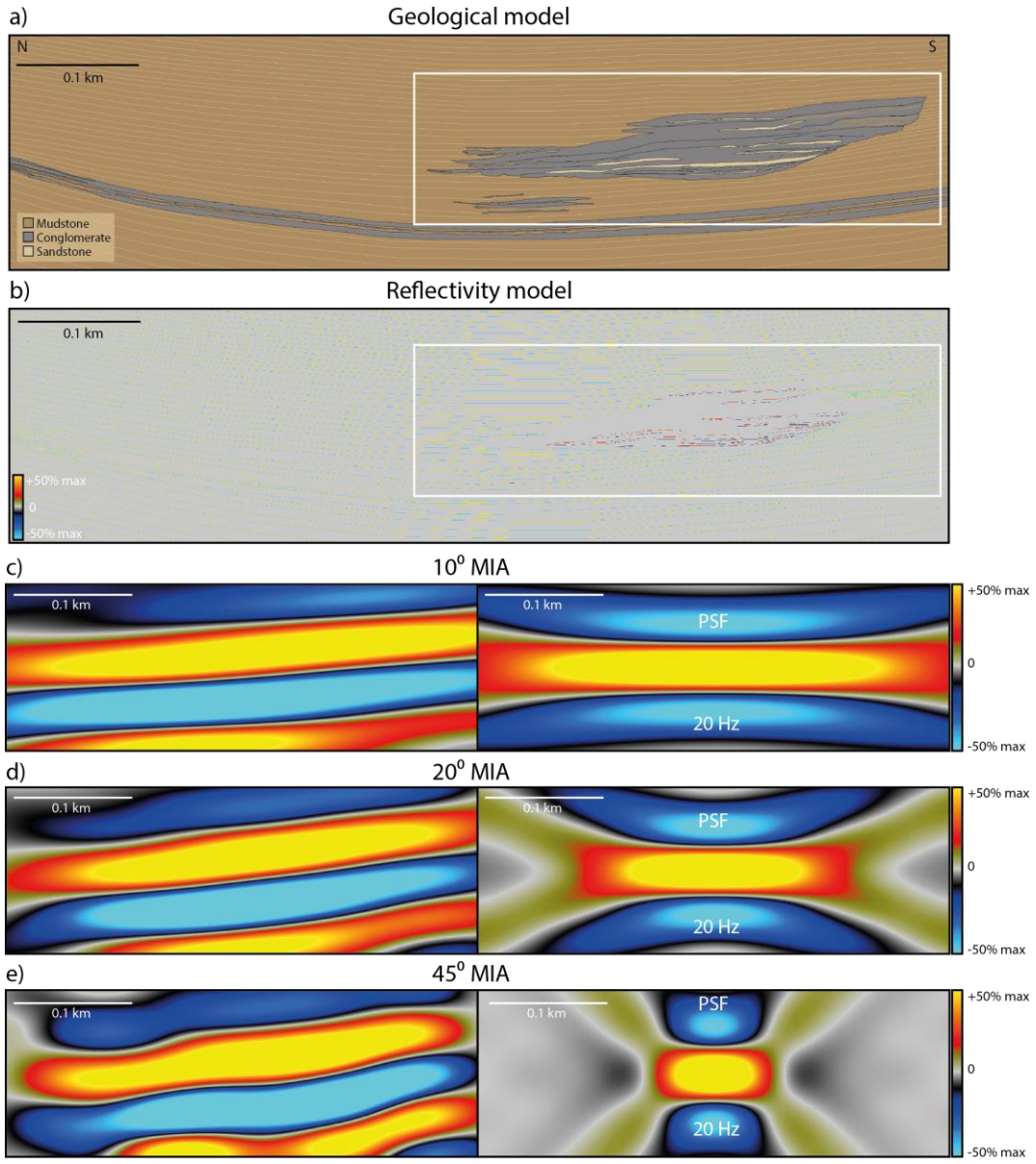

Figure 6.17: Synthetic seismic of Stylia 1A, showing the effects of different angles of maximum illumination from 10 to 45 degrees.

Figure 6.17 presents the results for Stylia 1A, focused on the channel complex. At 10º maximum illumination, the reflections of the top and base boundaries of the channel complex appear flat and more laterally extensive than in reality. The same applies when increasing the illumination angle to 20º. At 45º, the external shape of the channel complex is more detectable as the average apparent dip of the strata is less than 45º. However, the steep apparent dip of the southern channel margin cannot be detected in the seismic images and requires a higher maximum illumination angle to be interpretable.

Cross-section C comprises generally steeper dipping strata than the Stylia model, making the maximum illumination angle parameter even more impactful when it comes to seismic detectability (fig. 6.18). The channel system is close to undetectable in seismic images for illumination angles below of 10º and 20º. The seismic signature at these illumination angles is characterized by distorted and stretched reflections of lower amplitudes than at higher illumination angles.

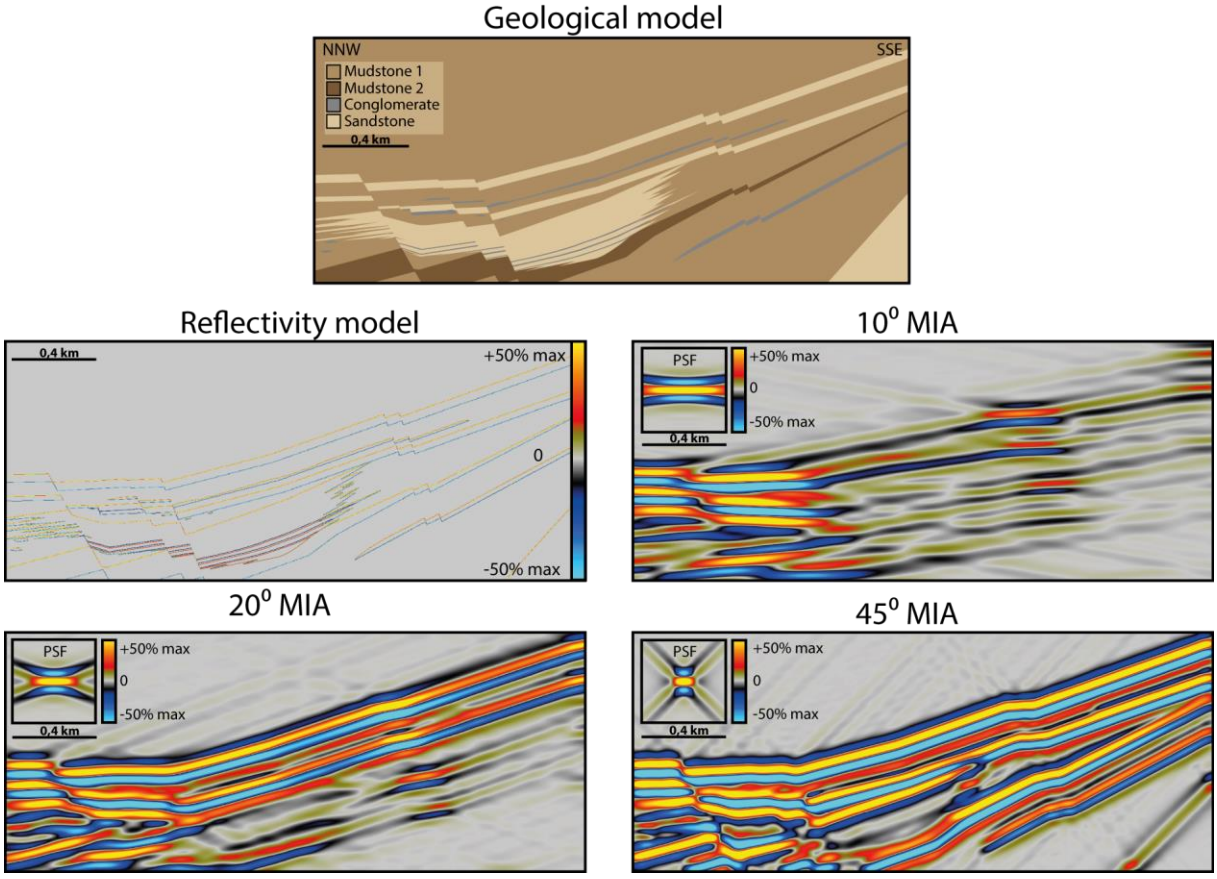

Figure 6.18: Synthetic seismic of Cross-section C, showing the effects of different angles of maximum illumination from 10 to 45 degrees.

6.3.4 Changing the incident angle

The angle of incidence is a geophysical parameter that affects both the reflectivity and the resolution of the seismic signal, both horizontally and vertically. In the seismic modelling experiment, incident angles of 0º, 10º, 20º and 30º were tested. A constant frequency of 20 Hz and a 45º maximum illumination angle were applied for all cases in this section, i.e., from Stylia 1A and Cross-section C.

Fig. 6.19 illustrates the effects on varying incident angles on Stylia 1A focused on the channel complex. The reflectivity models show little to no variation from 0º to 20º incidence, whereas at 30º a decrease in amplitude is observed. A decrease in lateral resolution can also be observed, which can be confirmed by the widening of the PSFs (fig 6.19f). All four of the corresponding seismic models show very little variation, indicating a low significance of the incident angle parameter on seismic imaging of the Stylia model. Cross-section C shows the same trend in the reflectivity models, but the seismic models reveal more variation (Fig. 6.20). The seismic response of the reflectors shows a progressively decreasing reflection amplitude, affecting the detectability of stratigraphic units. The positive reflections corresponding to the conglomerate channel belts are detectable at 0º and 10º but fall under seismic resolution at 20º and 30º. The negative reflections from the channel belts become undetectable first at 30º incidence.

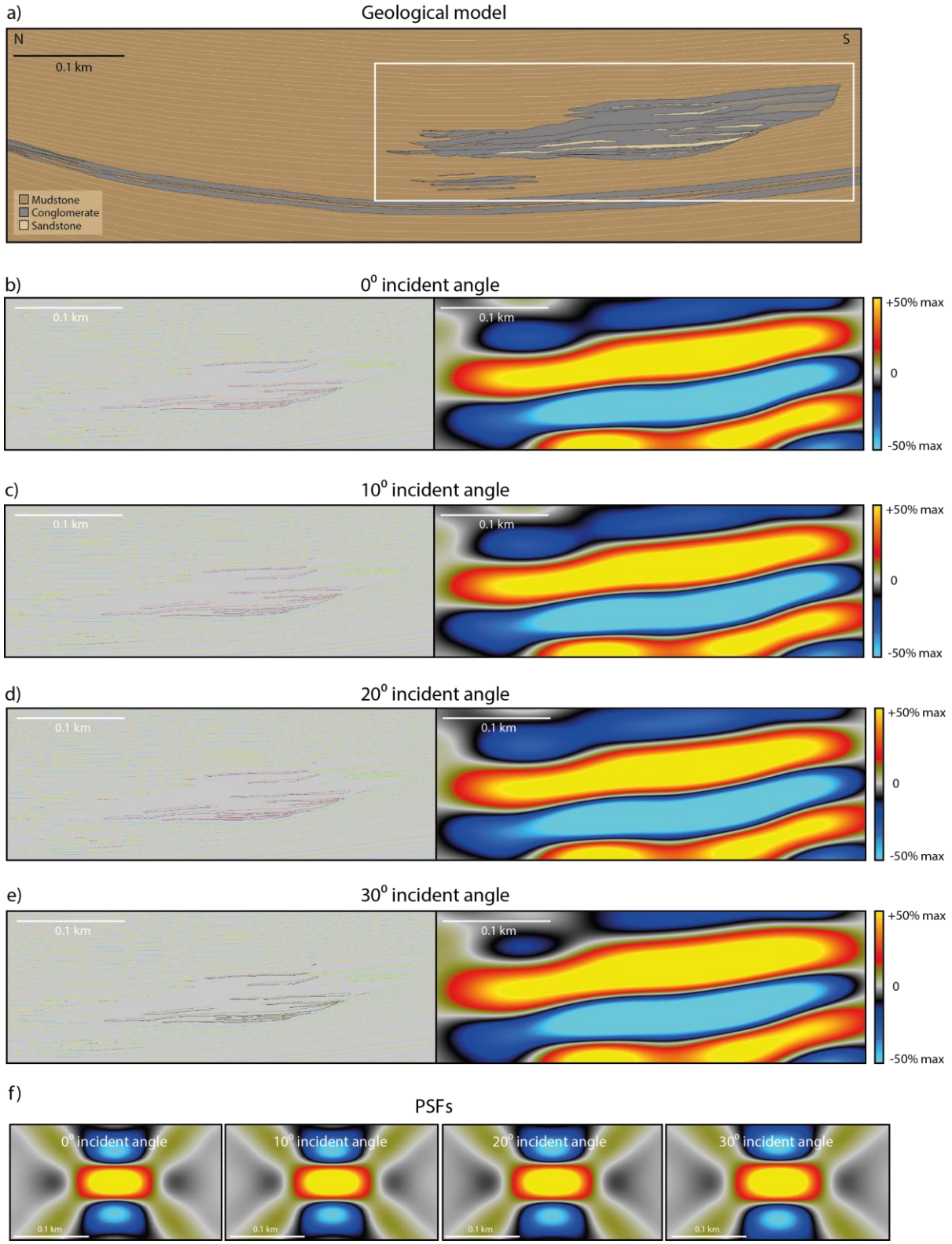

Figure 6.19: a) geological model of Stylia 1A, b-e) reflectivity models and corresponding synthetic seismic of Stylia 1A, showing the effects of varying the angle of incidence. f) corresponding PSFs.

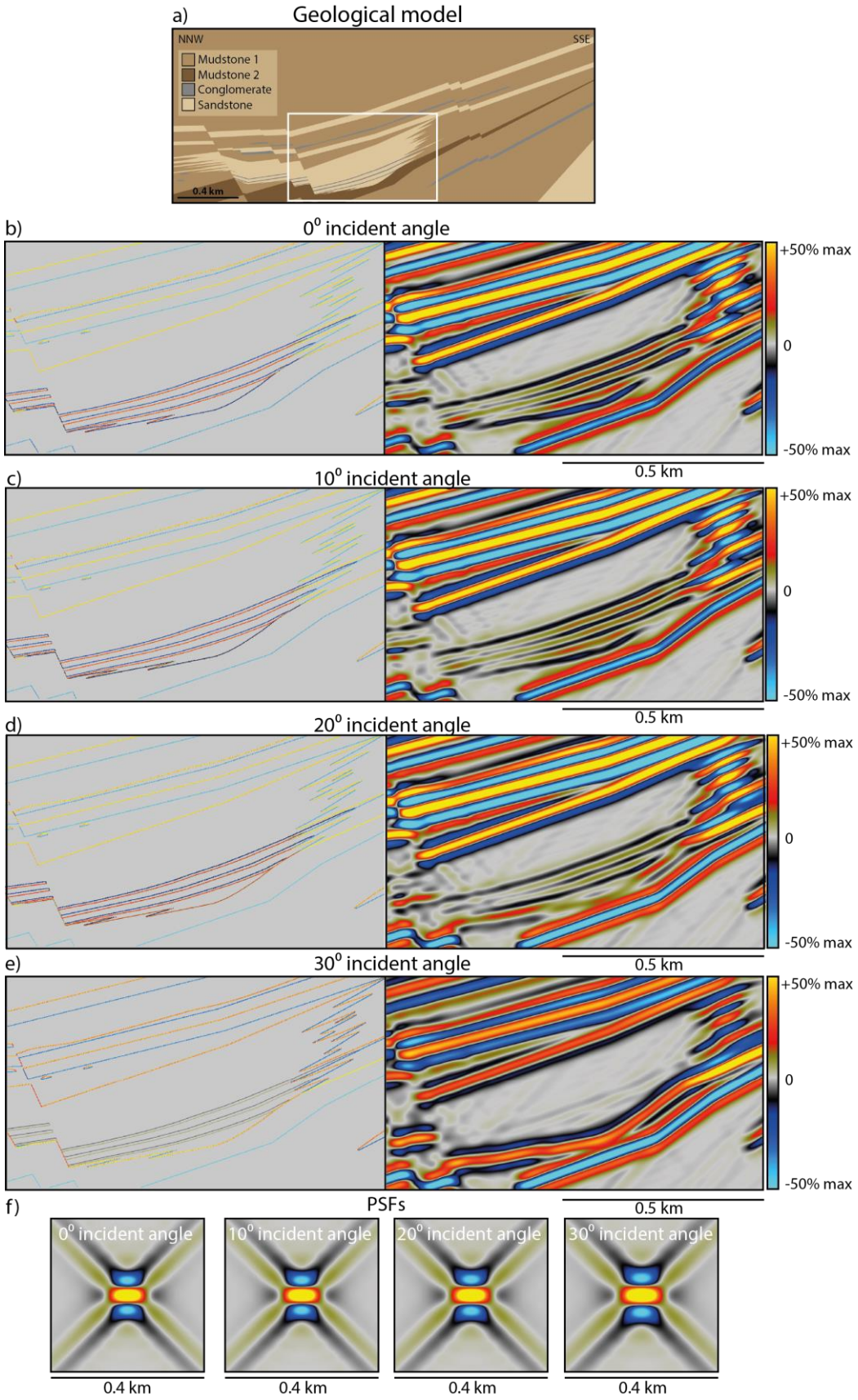

Figure 6.20: a) geological model of Cross-section C, b-e) reflectivity models and corresponding synthetic seismic of Cross-section C, showing the effects of varying the angle of incidence. f) corresponding PSFs.

6.3.5 Changing the set of elastic properties from different wells

In the data preparation for seismic modelling, two sets of elastic properties were determined, corresponding to two separate wells in the Fenja field, offshore Norway. The selected intervals with corresponding Vp, Vs and density values as well as calculated acoustic impedance for each lithology are listed in table 6.2. To test the impact of using elastic properties from different well locations and depths on seismic imaging of a channel complex, the Stylia 1B model was used (fig. 6.21). Fixed parameters of 45º maximum illumination angle and 20º incident angle were applied for both cases, and a variety of frequencies (20, 40, 60 & 140 Hz) were tested to better illustrate the effect.

Tabell 6.2: Elastic properties from wells 6406/12-3S and 6406/12-3B.

Well	Lithology	Interval (m-MD)	Vp (km/s)	Vs (km/s)	Den (g/cm^3)	AI (km/s g/cm^3)
6406/12-3S	Mudstone	3794.7-3797.1	3.8	2.3	2.5	9.6
	Sandstone	3709.1-3710.9	4.1	2.5	2.4	9.8
	Conglomerate	3712.1-3713.1	3.9	2.3	2.4	9.4
6406/12-3B	Mudstone	4253.3-4254.7	3.7	2.2	2.6	9.6
	Sandstone	3862.0-3865.0	4.3	2.6	2.4	10.3
	Conglomerate	3844.5-3845.5	4.2	2.5	2.4	10.0

Fig. 6.21b shows the same frequency analysis as conducted in chapter 6.3.1, using elastic properties from well 6406/12-3B (hereafter referred to as 3B), and figure 6.21c illustrates the equivalent input model and frequency variations using elastic properties from well 6406/12-3S (hereafter referred to as 3S). The results show two significantly different seismic signatures. The seismic images generated using properties from well 3B show high amplitude reflections corresponding to the top and base of the channel complex and other conglomerate units. The internal stratigraphy of the channel complex is detected as low to medium amplitude reflections. The seismic images generated using properties from well 3S show the opposite trend, where the sandstones and mudstones generate higher amplitude reflectivities than the conglomerates. This has to do with the varying contrast in acoustic impedance from on well to the other. Well 3B corresponds to a high contrast in acoustic impedance between mudstones and conglomerates, and a lower contrast between sandstones and conglomerates. Well 3S shows a higher contrast between sandstones and conglomerates than between mudstones and

conglomerates. A change in polarity is also observed between the two wells, where, e.g., the top channel boundary is detected as a positive reflection using properties from well 3B but as a negative reflection using properties from well 3S. The key results show that the external shape of the channel complex is better detected using properties from well 3B, whereas the internal stratigraphic architecture is better detected using properties from well 3S.

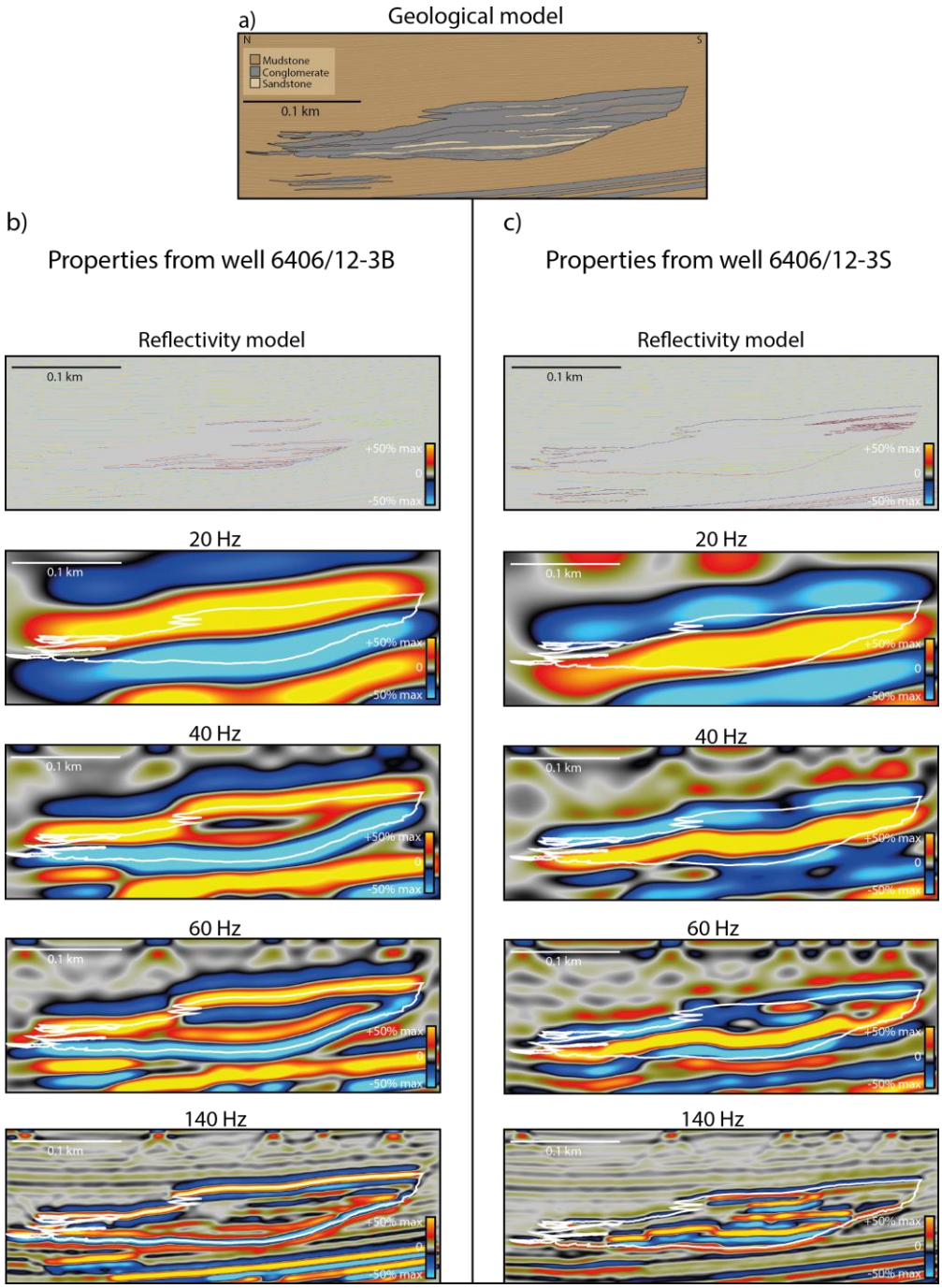

Figure 6.21: a) Geological model of Stylia 1B, b and c) synthetic seismic images with frequency variations from 20 – 140 Hz based on elastic properties from well 6406/12-3B (b) and 6406/12-3S (c). Outline of channel complex is superimposed on the seismic images to illustrate the difference.

6.3.6 Geological variations

According to the main interpretation of the Stylia VOM, the channel complex is overlain by a >100 m thick mudstone dominated unit, making the channel complex easily detectable in seismic images. In other cases, channel complexes may be surrounded by more complicated stratigraphy. To investigate the effect of a more complex surrounding stratigraphy on seismic images, the Stylia 2 geological model was constructed with extensive conglomerate sheets present above the channel complex (6.22b). Figure 6.22 compares the synthetic seismic images based on Stylia 1B with the synthetic seismic images based on Stylia 2, using frequencies of both 20 Hz and 40 Hz, a constant maximum illumination angle of 45º and incident angle of 20º. The results generally show a close to identical seismic signature of the channel complex itself between the two geological models. However, the seismic reflections of the overlying conglomerate sheets (fig 6.22f & h) make the channel complex more difficult to detect vertically, especially at lower frequencies where only the lateral amplitude contrast is imageable.

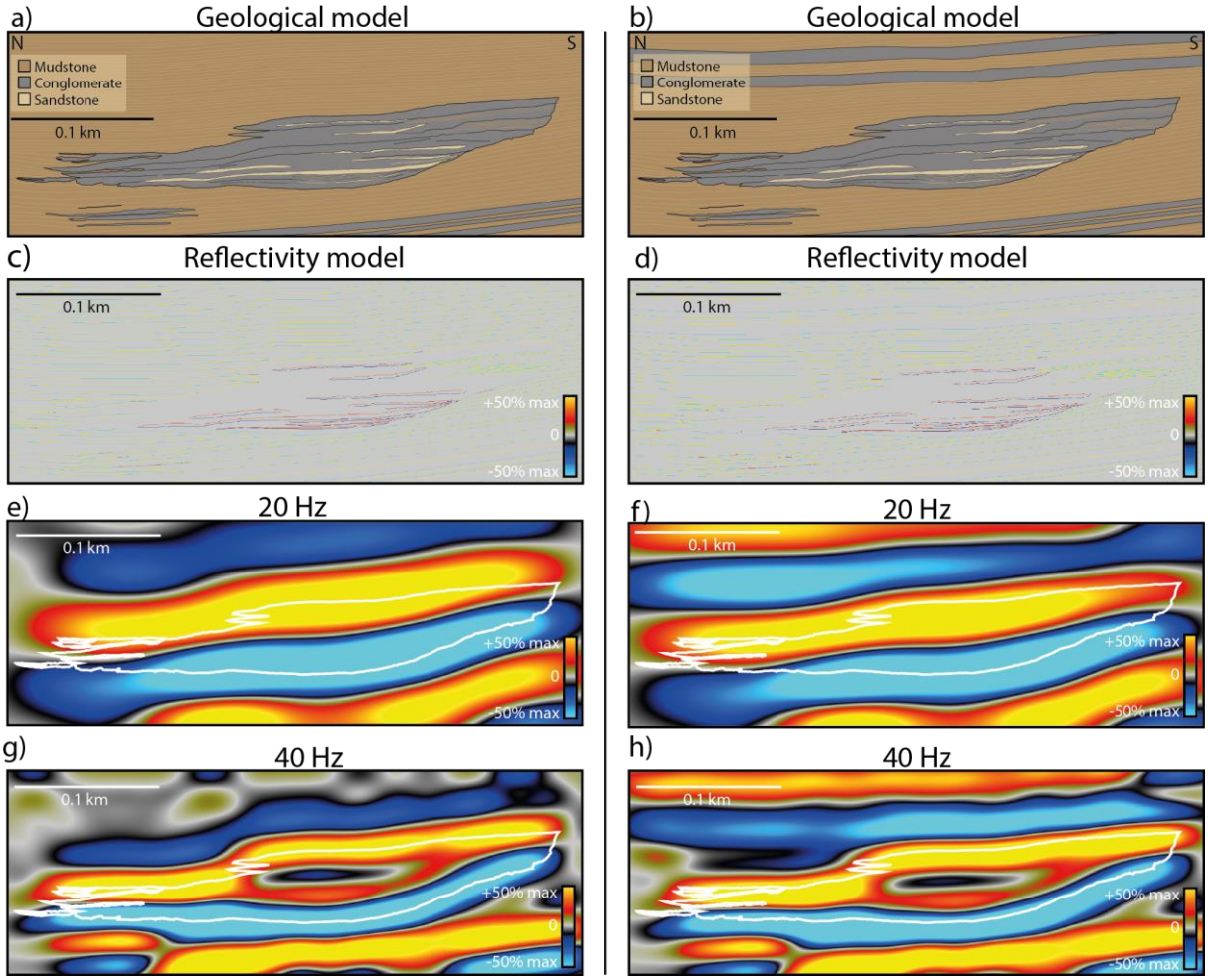

Figure 6.22: Comparison of Stylia 1B (a) and Stylia 2 (b) with varying frequencies (20-40 Hz).

During geological interpretation of the Stylia VOM, the rock-body geometry of the two upper conglomerate units was uncertain due to extensive vegetation coverage in the centre of the outcrop. Two possible interpretations were suggested, one comprising conglomerate units pinching out the towards north similar to those of the northern channel margin (Stylia 1B, fig 6.23a), and the other illustrating a gradual transition from conglomerates in the south to mudstones in the north (Stylia 3, fig 6.23b). To test the impact of such a minor difference in stratigraphic architecture within the same geological model, both versions were modelled and compared. The results showed that the gradual transition from conglomerates to mudstones produced a more discontinuous reflection of the top channel boundary, which could appear on the 40 Hz seismic image as a normal-fault feature.

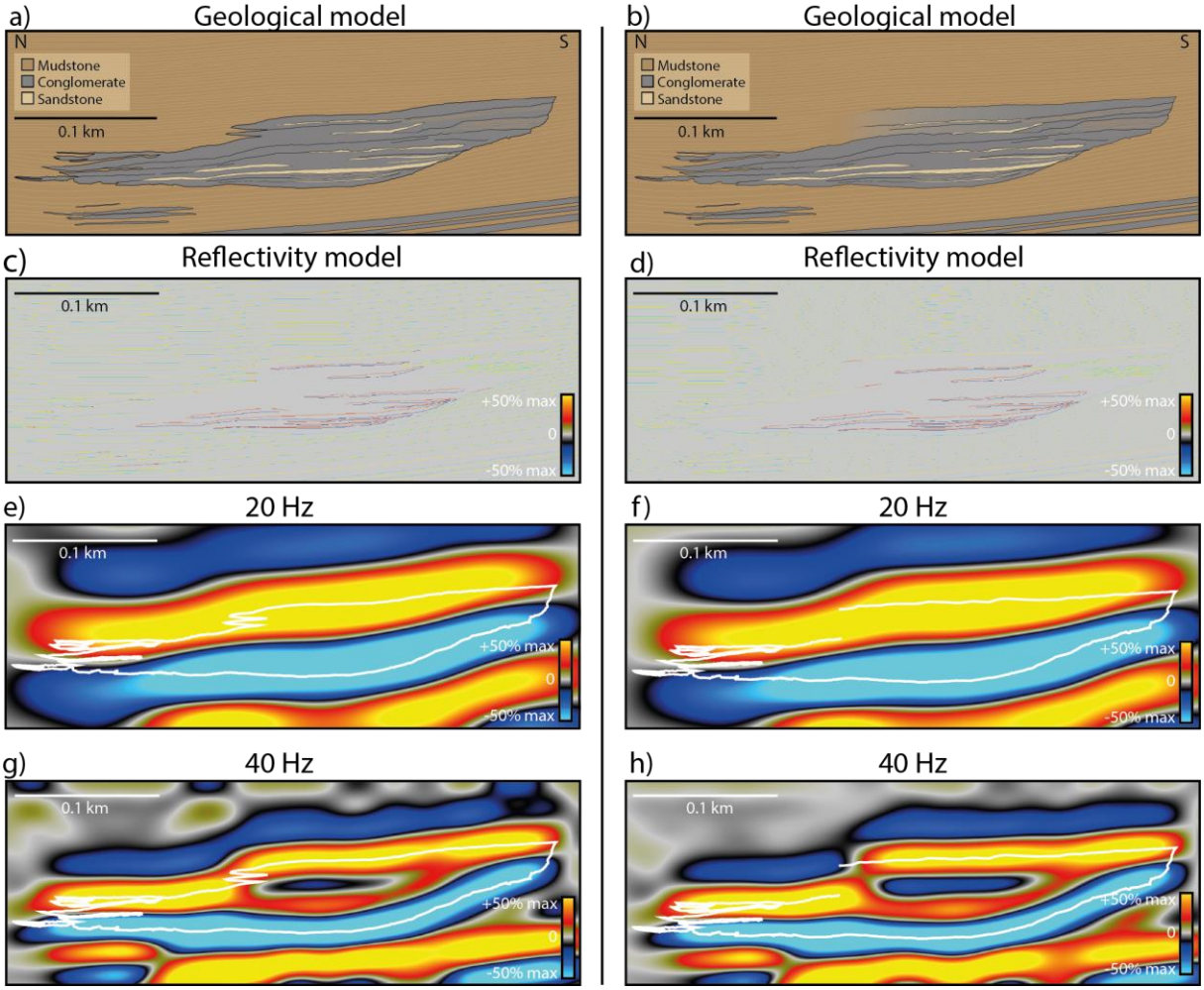

Figure 6.23: Comparison of Stylia 1B (a) and Stylia 3 (b) with varying frequencies (20-40 Hz)

7. Discussion

7.1 Insights from seismic modelling

7.1.1 Seismic expression of the Stylia deep-water channel complex

The synthetic seismic images generated using standard input parameters (table 6.1) and elastic properties from well 6406/12-3B on the base case (Stylia 1A) revealed the following seismic characteristics for the Stylia channel complex (fig. 6.9c):

i. The external shape of the ~45 m thick conglomerate dominated channel complex is recognized by a high amplitude peak reflection (top) and high amplitude trough reflection (base), mainly detected in seismic images as an abrupt lateral contrast in amplitude.
ii. Weak parallel reflections representing the surrounding mudstone dominated lithology with thin sandstone turbidites.
iii. High amplitude continuous reflections representing laterally extensive conglomerate sheets.
iv. Chaotic seismic reflections where surrounding mudstones and sandstones onlap/truncate the channel complex

Some features were undetectable using standard input parameters resembling conventional seismic at 20-60 Hz but could be imaged using higher frequencies (140 Hz). For example, individual sandstone beds interbedded with conglomerates within the channel complex, were recognized at higher frequencies (140 Hz) as medium amplitude, laterally pervasive reflections. The conglomerate lobes below the channel complex were also unresolvable at the standard frequency of 20 Hz but could be imaged at >40 Hz as high amplitude reflections.

Apart from the detectable features of the channel complex, certain stratigraphic elements and features proved to be undetectable on most synthetic seismic images. The channel complex was described having two different channel margins. The southern margin is characterized by a sharp, steep-sided unconformable margin with truncations of surrounding stratigraphy, whereas the northern margin shows a more transitional trend with individual conglomerate units pinching out towards north. However, these differences in margin architecture were poorly imaged on the synthetic seismic, likely due to the steeper dip of the southern margin being

greater than the maximum illumination angle of 45º. The steep-sided margin was visible only as a lateral amplitude contrast of the onlapping reflections, the same seismic expression as the northern margin.

Scales of architectural elements within the channel complex (e.g., lenticular vs lobate sandstones, winged channel forms, amalgamated/stacked conglomerates) were also observed to be unresolvable at frequencies between 20 Hz and 60 Hz, but produced subtle amplitude anomaly effects at the high frequency scenario of 140 Hz.

7.1.2 Seismic expression of regional cross-sections in the Amphithea fault block

The regional cross-sections contain a deep-water channel complex within a larger scale setting, which compared to the Stylia channel complex is more sandstone dominated containing conglomerate channel forms near the base of the system. The key seismic expression of these cross-sections based on standard input parameters revealed the following features (fig. 6.10c and 6.11c):

i. High amplitude, laterally continuous reflections imaging vertical changes in stratigraphic depositional units from sandstone-dominated to mudstone-dominated and conglomerate-dominated. Stratigraphic units down to ~10 m thickness produced reflections in the seismic images.
ii. Normal faults with an offset of >10 m were detectable
iii. Truncations of reflections up against the angular unconformity were detectable
iv. 10-20 m thick conglomerate-dominated channel forms within the sandstone-dominated channel complex were detected as low/medium amplitude reflections
v. Isolated conglomerate-dominated lobes of 10-20 m thickness intercalated in mudstone-dominated units above the channel complex were detected as medium amplitude reflections. Thinning and thickening of the lobate deposits were detected as subtle lateral amplitude variations (thin sections produced lower amplitudes and thicker sections produced higher amplitudes)

Overall, the seismic expression of the cross-sections was more complex than the Stylia model's, likely due to the larger scale and more heterogenous stratigraphy surrounding the channel complex. The detectability of the channel complex was affected by both the surrounding

stratigraphy as well as the normal faults. The external concave up shape of the channel complex was poorly imaged, likely due to the low contrast in elastic impedance between conglomerates and the mudstone 2 variation (table 5.1). In addition, normal faulting caused a break in continuity of the reflections, which combined with the low resolution of 20 Hz frequency made the architecture of the channel complex hard to resolve.

7.1.3 Effects of varying the geophysical parameters

Based on the results from the sensitivity analysis, key observations were made in terms of which geophysical parameters made the most impact on the Stylia channel complex and regional cross-sections. The most significant effects on seismic resolution and detectability were caused by varying dominant frequencies, angle of maximum illumination and level of noise. The angle of incidence made a minor impact on amplitudes, but not enough to severely affect the detectability of stratigraphic architectures. Ideal detection and imaging of a channel complex like in the Stylia model would therefore consist of the following parameters:

1. Frequency of at least 20 Hz for detection of the channel complex, higher frequencies of 40-60 Hz needed to image internal stratigraphic architecture.
2. A maximum illumination angle of >45º to resolve steeply dipping surfaces
3. Incident angle between 0-20º
4. Noise level of <50%

Variability in elastic properties from different wells also made a considerable impact on the synthetic seismic expression of the different lithologies. In real seismic surveys, these properties are fixed in the subsurface lithologies and are not determined by the conductors of the survey. The elastic properties of a rock (velocity and density) are dependent on factors like mineral composition, cementation, porosity, fluid content, environmental pressure, burial depth and compaction (e.g. Gardner et al., 1974). The general observation was that properties from well 3B included slightly higher velocities than in well 3S, but the density remained more or less the same. The contrast in elastic impedance between conglomerates and mudstones was greatest in well 3B, whereas the contrast between conglomerates and sandstones was greatest in well 3S, resulting in two significantly different seismic expressions (figure 6.21). The great variability may be caused by several influential factors. The rock properties extracted from well 3B were collected several hundreds of meters deeper and approximately 700 m more distally into the

basin than the properties from well 3S (figure 2.5). Increasing burial depth is often accompanied by increased compaction and cementation, which typically results in higher velocities and densities with depth (Gardner et al., 1974). However, while there is an existing depth difference between the two sets of rock properties, it might not be large enough to produce a significant difference and is likely not the only influencing factor. Because the wells are located around 700 m apart from each other, a natural spatial variability of subsurface lithology and stratigraphy could be a probable factor influencing the seismic expression. Based on the available core photos, conglomerates and sandstones do not look identical in the two wells, with intervals from well 3B looking slightly more fine-grained than in 3S which could cause the rock properties of similar lithologies to vary spatially. The combination of these factors indicates that a coarse-grained channel complex within a mudstone-dominated region may be detected differently in various part of a depocenter, and is comparable to analogues in the subsurface with similar contrasts in elastic impedance between lithologies.

7.2 Applications of seismic modelling of deep-water depositional systems

During this study, observations have been made that may assist future seismic interpreters in detecting features of syn-rift deep-water stratigraphy in industry-focused seismic observations in the subsurface. Most importantly, the scales of imageable features at different frequencies and illumination angles need to be considered. A 400-m wide and 50-m high channel complex may only be detectable in conventional seismic as a subtle or abrupt lateral amplitude contrast, dependent on the surrounding lithologies. Subtle amplitude variabilities in continuous reflections may also signify thinning or thickening of isolated lobate deposits, as observed in the regional cross-sections where conglomerate-dominated lobes of 10-20 m thickness produced reflections varying laterally in amplitude where thinning and thickening of the beds occurred. Internal architectural elements are thus not necessarily undetectable because they fail to produce distinct reflections, so being aware of subtle amplitude variabilities and what they may represent is significant to be able to reduce uncertainty of internal stratigraphic architecture as an interpreter. However, the information obtained from seismic images is ultimately limited and some features that are central in understanding the full complexity of a system remain unresolvable. To avoid overlooking significant features under seismic interpretation, seismic data should preferably be used in correlation to e.g., wireline logs, cores and other types of well data to support interpretation.

7.3 Limitations and uncertainties

7.3.1 Limitations of virtual outcrop modelling and geological interpretation

The process of generating synthetic seismic images from an outcrop starts with development of a geological input model. The reliability and accuracy of the seismic images are therefore highly dependent on the quality of the geological model. Virtual outcrop modelling by photogrammetry and subsequent geological interpretation is an efficient way of producing this input model as it enables detailed mapping of areas that are normally out of reach or at very large scales in the field. However, some limitations and uncertainties must be considered during this process. Primarily, data acquisition in the form of still photos and videos lays the foundation of the final VOM. Weather and light conditions are therefore important to consider when preparing for obtaining data. In the case of the Stylia model, still photos and video frames from various days and light conditions were used to build the VOM. This resulted in variable-coloured surfaces, making it more challenging to conduct accurate interpretations. Using data from a single session of data acquisition would make the model more consistent in terms of colours and textures, which would again improve the reliability of interpretation based on e.g., colour changes. The geological interpretation is also dependent on factors like the aerial extent of the outcrop and vegetation coverage. Producing a complete geological model of the Stylia outcrop required both extrapolation and interpolation, to which there is attached some uncertainty.

7.3.2 Limitations of elastic properties

P- and S-wave velocities along with density values were calculated based on well data extracted from Late Jurassic stratigraphy in two wells in the Fenja field, Halten Terrace, Norwegian Sea. For both wells, finding long intervals of a single lithology proved to be challenging, and some shorter intervals of <2 m therefore had to be used. Short intervals may lower the accuracy of the velocity and density values as a result of sampling resolution of wireline tools.

Field and subsurface studies (e.g. Muravchik et al., 2020 and Jones et al., 2021) highlight that substantial variability of facies exists within these broader lithological divisions (e.g. clay-matrix supported conglomerates, boulder breccias, gravelly sandstones). The geological reality may be significantly more complex. The impact of this smaller scale facies variability on

physical properties is relatively unexplored and cannot be accurately constrained within the exposure and as a result the more confident 3-part lithological model with the strongest lithological contrasts is used. A natural spatial variability in cementation, deformation and overburden stratigraphy is also not accounted for in this study, which may impact resultant seismic imaging.

7.4 Comparative studies

Comparisons to other outcrop based seismic modelling studies

Bakke et al. (2008) and Falivene et al. (2010) conducted outcrop based seismic modelling studies of the deep-marine Ainsa turbidite system in the Southern Pyrenees, Spain. Bakke et al. (2008) performed a full-wavefield PSF convolution modelling study Ainsa II turbidite system, whereas Falivene et al. (2010) used 1D convolution modelling of the Ainsa system. The Ainsa II channel system comprises five different amalgamated clastic sand bodies bounded by erosional surfaces. Unlike the Stylia channel complex, the Ainsa II system is strongly laterally migrating, and the sand bodies are situated adjacent to one another. The thickness of the Ainsa II channel complex is comparable to that of Stylia (40- 50 m). Similar to observations here, internal, often highly amalgamated stratigraphic architecture was not able to be resolved inside the channel complex. Steep-sided margins in both studies provide subtle lateral amplitude contrasts, but struggle to resolve with great accuracy the geometry of channel margins. Bakke et al. (2008) similarly propose that lateral dimming of amplitudes may reflect more gradual reductions of lithological contrast in less erosional channel margins also observed in the northern margin of the Stylia models.

The base of the Ainsa turbidite system is described as an angular unconformity, whereas the top gradually moves into finer grained units. One of the key observations from the study conducted by Falivene et al. (2010) was that the erosive bases of the channel complexes were clearly detectable as a high amplitude reflections, but the positions of channel complex tops and margins were uncertain. The same trend was observed for the Stylia models where both the base and top of the channel complex were unconformable and produced high amplitude reflections. Falivene et al. (2010) also concluded that precise detection of individual architectural elements and facies distribution within channel complexes was impossible even at the highest frequency of 75 Hz, which also proved to be the case in this study. These similarities

in results may help improve seismic interpretation of deep-water channel complexes in real seismic data.

Comparisons to subsurface studies

Offshore Norway conventional seismic data

Jones et al. (2020) present a subsurface case of a small, confined, syn-tectonic basin sourced from a local basement high with a catchment size, and depocenter dimension similar to those observed in the Corinth Rift and allows for greater control on the analogue potential of these systems. Comparing the seismic sections of the Fenja field to the conventional synthetic seismic images of both the Stylia channel complex and the regional larger scale cross-sections reveals certain similarities, as it comprises approximately the same seismic resolution imaging reflectivity at scales of ~50 m. The three-fold stratigraphic framework of the Fenja field comprising an early-rift, peak-rift and late-rift succession is detectable at conventional frequency, and it is possible to distinguish the seismic expression within different depositional units as well as reflection truncations and structural elements like the basin bounding Vingleia fault. The same was recognized on the synthetic seismic images of the cross-sections, where the heterogenic stratigraphy of stratigraphic units as well as normal faults (although having significantly smaller displacement than the Vingleia fault) were well imaged. At 20 Hz frequency, the Stylia channel complex could only be detected in the synthetic seismic images by an abrupt increase in amplitude of the reflections corresponding to the top and base of the external channel form. Similar lateral contrasts in amplitudes within single continuous reflections can be observed on several occasions within the industry seismic section from the Fenja field. Based on observations from the synthetic seismic images, this may indicate a higher complexity in stratigraphic architecture than resolved in the industry seismic data.

Koch et al. (2018) presents the Skarfjell oil- and gas-discovery, which is located 50 km north of the Troll Field in the NE North Sea. The reservoir sits within a structural/stratigraphic trap formed along the edge of a submarine canyon, comprising deep-water turbidites and gravity-flow deposits. Compared to the Fenja field which mainly contains submarine fan deposits, the Skarfjell discovery comprises more channelized elements, which is more like the geological setting of the Stylia model and regional cross-sections of the Corinth Rift studied in this thesis. The seismic section across the Skarfjell field contains approximately the same seismic resolution as the conventional seismic frequencies of the Stylia model, imaging reflectivity at

scales of ~50 m. The seismic signature of the turbidite and gravity-flow system reveals high amplitude reflections that onlap and truncates faults, similar to what can be observed in the cross-sections. Between the base of the turbidites and the top Volgian unconformity, bright events with lateral amplitude contrasts can also be observed, which might indicate the presence of channelised elements. Like in the conventional seismic images of the Stylia model and cross-section, no high level of detail can be resolved for internal stratigraphic architecture.

High frequency shallow seismic

Zhang and Scholz (2015) conducted a study of Holocene and Pliocene turbidite rift systems of lacustrine rift basins in East Africa using high frequency 2D and 3D seismic reflection data. In this thesis, modelling synthetic seismic images with a 140 Hz frequency was done for both the Stylia model and the cross-section to test investigate the seismic signature of the cases resembling high resolution shallow seismic data. As expected, significantly more details of stratigraphic architecture were detected, although not all individual layers were completely resolved. In the high frequency study of Zhang and Scholz (2015), several depositional and architectural elements were detectable, including individual channels, overbank levees with sediment waves and depositional lobes.

8. Conclusions

In this thesis, synthetic 2D seismic images generated from geological models of syn-rift deep-water complexes based on virtual outcrop models and cross-sections have been presented. Sensitivity analyses of various geophysical parameters, geological models and elastic properties have been conducted to investigate the level of impact on the seismic signature. The presented results and discussion have led to the following conclusions of this thesis:

1. The final interpretations of the Stylia channel comprises an aggrading, multi-episode coarse-grained 45-m thick channel complex dominated by gravity flow deposited sandy-matrix conglomerates that are either vertically stacked, amalgamated, or interlayered with finer grained units of sandstone or mudstone. The surrounding stratigraphy is dominated by hemipelagic mudstones interbedded with thin (10-30 cm) sandy turbidites dominate, with occasional narrow (~3.7 m thick) conglomerate lobes and laterally extensive tabular conglomerate sheets (~6 m thick).
2. The seismic signature of the Stylia VOM based on standard input properties include: (1) a high amplitude positive reflection (top of channel complex) and high amplitude negative reflection (base of channel complex) representing the channel complex, (2) weak parallel reflections representing the dominant fine-grained stratigraphy, (3) high amplitude continuous reflections representing laterally extensive conglomerate sheets, (4) Chaotic seismic reflections where surrounding mudstones and sandstones onlap/truncate the channel complex
3. The generated synthetic seismic images revealed a vertical resolution of ~50m for conventional seismic frequencies of 20-40 Hz, but architectural elements and rock body geometries down to ~10 m thickness can be detected in seismic models if reflectivity is strong enough.
4. The geophysical parameter sensitivity analyses revealed that the dominant frequency, maximum illumination angle and level of noise made the most impact on seismic images.
5. Outcrop-based seismic modelling can help bridge the gap between seismic-scale images and detailed sub-seismic scale stratigraphic heterogeneity. However, significant details in stratigraphic architecture may be undetectable, so seismic data should preferably be used in correlation to e.g., wireline logs, cores and other types of well data.

References

ANELL, I., LECOMTE, I., BRAATHEN, A. & BUCKLEY, S. 2016. Synthetic seismic illumination of small-scale growth faults, paralic deposits and low-angle clinoforms: A case study of the Triassic successions on Edgeøya, NW Barents Shelf. *Marine and Petroleum Geology,* 77**,** 625-639.

BAKKE, K., GJELBERG, J. & PETERSEN, S. A. 2008. Compound seismic modelling of the Ainsa II turbidite system, Spain: Application to deep-water channel systems offshore Angola. *Marine and Petroleum Geology,* 25**,** 1058-1073.

BARNES, N. E. & NORMARK, W. R. 1985. Diagnostic parameters for comparing modern submarine fans and ancient turbidite systems. *Submarine fans and related turbidite systems.* Springer.

BELDERSON, R., KENYON, N., STRIDE, A. & PELTON, C. 1984. A 'braided'distributary system on the Orinoco deep-sea fan. *Marine Geology,* 56**,** 195-206.

BOUMA, A. 1964. Turbidites. *Developments in sedimentology.* Elsevier.

BRUNNER, C. A. & LEDBETTER, M. T. 1987. Sedimentological and micropaleontological detection of turbidite muds in hemipelagic sequences: an example from the late Pleistocene levee of Monterey Fan, central California continental margin. *Marine micropaleontology,* 12**,** 223-239.

BULL, S., CARTWRIGHT, J. & HUUSE, M. 2009. A review of kinematic indicators from mass-transport complexes using 3D seismic data. *Marine and Petroleum Geology,* 26**,** 1132-1151.

BAAS, J. H., BEST, J. L. & PEAKALL, J. 2011. Depositional processes, bedform development and hybrid bed formation in rapidly decelerated cohesive (mud–sand) sediment flows. *Sedimentology,* 58**,** 1953-1987.

COLLIER, R. L. & DART, C. 1991. Neogene to Quaternary rifting, sedimentation and uplift in the Corinth Basin, Greece. *Journal of the Geological Society,* 148**,** 1049-1065.

CULLEN, T. M., COLLIER, R. E. L., GAWTHORPE, R. L., HODGSON, D. M. & BARRETT, B. J. 2020. Axial and transverse deep-water sediment supply to syn-rift fault terraces: Insights from the West Xylokastro Fault Block, Gulf of Corinth, Greece. *Basin Research,* 32**,** 1115-1149.

CULLIS, S., COLOMBERA, L., PATACCI, M. & MCCAFFREY, W. D. 2018. Hierarchical classifications of the sedimentary architecture of deep-marine depositional systems. *Earth-Science Reviews,* 179**,** 38-71.

DAMUTH, J. E., FLOOD, R. D., KOWSMANN, R. O., BELDERSON, R. H. & GORINI, M. A. 1988. Anatomy and growth pattern of Amazon deep-sea fan as revealed by long-range side-scan sonar (GLORIA) and high-resolution seismic studies. *AAPG bulletin,* 72**,** 885-911.

FALEIDE, T. S., BRAATHEN, A., LECOMTE, I., MULROONEY, M. J., MIDTKANDAL, I., BUGGE, A. J. & PLANKE, S. 2021. Impacts of seismic resolution on fault interpretation: Insights from seismic modelling. *Tectonophysics,* 816**,** 229008.

FALIVENE, O., ARBUÉS, P., LEDO, J., BENJUMEA, B., MUÑOZ, J. A., FERNÁNDEZ, O. & MARTÍNEZ, S. 2010. Synthetic seismic models from outcrop-derived reservoir-scale three-dimensional facies models: The Eocene Ainsa turbidite system (southern Pyrenees). *AAPG bulletin,* 94**,** 317-343.

FISHER, W. L., GALLOWAY, W. E., STEEL, R. J., OLARIU, C., KERANS, C. & MOHRIG, D. 2021. Deep-water depositional systems supplied by shelf-incising submarine canyons: Recognition and significance in the geologic record. *Earth-Science Reviews,* 214**,** 103531.

FORD, M., ROHAIS, S., WILLIAMS, E. A., BOURLANGE, S., JOUSSELIN, D., BACKERT, N. & MALARTRE, F. 2013. Tectono-sedimentary evolution of the western Corinth rift (Central Greece). *Basin Research,* 25**,** 3-25.

GANI, M. R. 2004. From turbid to lucid: a straightforward approach to sediment gravity flows and their deposits. *The Sedimentary Record,* 2**,** 4-8.

GARDNER, G., GARDNER, L. & GREGORY, A. 1974. Formation velocity and density—The diagnostic basics for stratigraphic traps. *Geophysics,* 39**,** 770-780.

GAWTHORPE, R. L., LEEDER, M. R., KRANIS, H., SKOURTSOS, E., ANDREWS, J. E., HENSTRA, G. A., MACK, G. H., MURAVCHIK, M., TURNER, J. A. & STAMATAKIS, M. 2018. Tectono-sedimentary evolution of the Plio-Pleistocene Corinth rift, Greece. *Basin Research,* 30**,** 448-479.

HARRIS, P. T. & WHITEWAY, T. 2011. Global distribution of large submarine canyons: Geomorphic differences between active and passive continental margins. *Marine Geology,* 285**,** 69-86.

HESSE, R. 1975. Turbiditic and non-turbiditic mudstone of Cretaceous flysch sections of the East Alps and other basins. *Sedimentology,* 22**,** 387-416.

HESSE, R. 1989. " Drainage systems" associated with mid-ocean channels and submarine yazoos: Alternative to submarine fan depositional systems. *Geology,* 17**,** 1148-1151.

HUANG, Y. 2018. Sedimentary characteristics of turbidite fan and its implication for hydrocarbon exploration in Lower Congo Basin. *Petroleum Research,* 3**,** 189-196.

IVERSON, R. M. 1997. The physics of debris flows. *Reviews of geophysics,* 35**,** 245-296.

IVERSON, R. M., LOGAN, M., LAHUSEN, R. G. & BERTI, M. 2010. The perfect debris flow? Aggregated results from 28 large-scale experiments. *Journal of Geophysical Research: Earth Surface,* 115.

IVERSON, R. M. & VALLANCE, J. W. 2001. New views of granular mass flows. *Geology,* 29**,** 115-118.

JONES, G. E., WELBON, A. I., MOHAMMADLOU, H., SAKHAROV, A., FORD, J., NEEDHAM, T. & OTTESEN, C. 2020. Complex stratigraphic fill of a small, confined syn-rift basins: an Upper Jurassic example from offshore mid-Norway. *Geological Society, London, Special Publications,* 495.

KANE, I. A., KNELLER, B. C., DYKSTRA, M., KASSEM, A. & MCCAFFREY, W. D. 2007. Anatomy of a submarine channel–levee: an example from Upper Cretaceous slope sediments, Rosario Formation, Baja California, Mexico. *Marine and Petroleum Geology,* 24**,** 540-563.

KEAREY, P., BROOKS, M. & HILL, I. 2002. *An introduction to geophysical exploration,* John Wiley & Sons.

KNELLER, B. C. & BRANNEY, M. J. 1995. Sustained high-density turbidity currents and the deposition of thick massive sands. *Sedimentology,* 42**,** 607-616.

KOCH, J.-O., FRISCHBUTTER, A., ØYGARD, K. & CATER, J. The 35/9-7 Skarfjell discovery: a genuine stratigraphic trap, NE North Sea, Norway. Geological Society, London, Petroleum Geology Conference series, 2018. Geological Society of London, 339-354.

KOLLA, V., POSAMENTIER, H. & WOOD, L. 2007. Deep-water and fluvial sinuous channels—Characteristics, similarities and dissimilarities, and modes of formation. *Marine and Petroleum Geology,* 24**,** 388-405.

KUENEN, P. H. 1951. Properties of turbidity currents of high density.

KUENEN, P. H. & SENGUPTA, S. 1970. Experimental marine suspension currents, competency and capacity. *Geologie en Mijnbouw,* 49**,** 89-118.

LECOMTE, I., LAVADERA, P. L., BOTTER, C., ANELL, I., BUCKLEY, S. J., EIDE, C. H., GRIPPA, A., MASCOLO, V. & KJOBERG, S. 2016. 2 (3) D convolution modelling of complex geological targets beyond–1D convolution. *First Break,* 34.

LECOMTE, I., LUBRANO-LAVADERA, P. & SCHMID, D. Understanding and Analysing Seismic Images-Insight through Appropriate Modelling. 77th EAGE Conference and Exhibition-Workshops, 2015. European Association of Geoscientists & Engineers, 1-5.

LEEDER, M., MACK, G., BRASIER, A., PARRISH, R., MCINTOSH, W., ANDREWS, J. & DUERMEIJER, C. 2008. Late-Pliocene timing of Corinth (Greece) rift-margin fault migration. *Earth and Planetary Science Letters,* 274**,** 132-141.

LINDSEY, J. 1989. The Fresnel zone and its interpetive significance. *The Leading Edge,* 8**,** 33-39.

LOWE, D. R. 1982. Sediment gravity flows; II, Depositional models with special reference to the deposits of high-density turbidity currents. *Journal of sedimentary research,* 52**,** 279-297.

LUBRANO-LAVADERA, P., SENGER, K., LECOMTE, I., MULROONEY, M. J. & KÜHN, D. 2019. Seismic modelling of metre-scale normal faults at a reservoir-cap rock interface in Central Spitsbergen, Svalbard: implications for CO2 storage. *Norwegian Journal of Geology*, 99**,** 329-347.

MCHARGUE, T., PYRCZ, M. J., SULLIVAN, M. D., CLARK, J., FILDANI, A., ROMANS, B., COVAULT, J., LEVY, M., POSAMENTIER, H. & DRINKWATER, N. 2011. Architecture of turbidite channel systems on the continental slope: patterns and predictions. *Marine and petroleum geology,* 28**,** 728-743.

MENARD JR, H. W. 1955. Deep-sea channels, topography, and sedimentation. *AAPG Bulletin,* 39**,** 236-255.

MIDDLETON, G. V. 1967. Experiments on density and turbidity currents: III. Deposition of sediment. *Canadian Journal of Earth Sciences,* 4**,** 475-505.

MIDDLETON, G. V. & HAMPTON, M. A. 1973. Part I. Sediment gravity flows: mechanics of flow and deposition.

MULDER, T. & ALEXANDER, J. 2001. The physical character of subaqueous sedimentary density flows and their deposits. *Sedimentology,* 48**,** 269-299.

MURAVCHIK, M., HENSTRA, G. A., ELIASSEN, G. T., GAWTHORPE, R. L., LEEDER, M., KRANIS, H., SKOURTSOS, E. & ANDREWS, J. 2020. Deep-water sediment

transport patterns and basin floor topography in early rift basins: Plio-Pleistocene syn-rift of the Corinth Rift, Greece. *Basin Research,* 32**,** 1194-1222.

MUTTI, E. & NORMARK, W. R. 1987. Comparing examples of modern and ancient turbidite systems: problems and concepts. *Marine clastic sedimentology.* Springer.

MUTTI, E. & RICCI LUCCHI, F. 1978. Turbidites of the northern Apennines: introduction to facies analysis. *International geology review,* 20**,** 125-166.

NEMEC, W. 1990. Aspects of sediment movement on steep delta slopes. *Coarse-grained deltas,* 10**,** 29-73.

NIXON, C. W., MCNEILL, L. C., BULL, J. M., BELL, R. E., GAWTHORPE, R. L., HENSTOCK, T. J., CHRISTODOULOU, D., FORD, M., TAYLOR, B. & SAKELLARIOU, D. 2016. Rapid spatiotemporal variations in rift structure during development of the Corinth Rift, central Greece. *Tectonics,* 35**,** 1225-1248.

NORMARK, W. R. 1970. Growth patterns of deep-sea fans. *AAPG bulletin,* 54**,** 2170-2195.

NORMARK, W. R. 1978. Fan valleys, channels, and depositional lobes on modern submarine fans: characters for recognition of sandy turbidite environments. *AAPG Bulletin,* 62**,** 912-931.

PIPER, D. W. 1978. Turbidite muds and silts on deepsea fans and abyssal plains. *Sedimentation in submarine canyons, fans, and trenches*.

POSTMA, G. 1984. Mass-flow conglomerates in a submarine canyon: Abrioja fan-delta, Pliocene, southeast Spain.

PRÉLAT, A., HODGSON, D. & FLINT, S. 2009. Evolution, architecture and hierarchy of distributary deep-water deposits: a high-resolution outcrop investigation from the Permian Karoo Basin, South Africa. *Sedimentology,* 56**,** 2132-2154.

RABBEL, O., GALLAND, O., MAIR, K., LECOMTE, I., SENGER, K., SPACAPAN, J. B. & MANCEDA, R. 2018. From field analogues to realistic seismic modelling: a case study of an oil-producing andesitic sill complex in the Neuquén Basin, Argentina. *Journal of the Geological Society,* 175**,** 580-593.

RYAN, H. 1994. Ricker, ormsby, klauder. *Butterworth—A choice of wavelets: CSEG Recorder,* 19**,** 8-9.

SAVAGE, S. B. 1979. Gravity flow of cohesionless granular materials in chutes and channels. *Journal of Fluid Mechanics,* 92**,** 53-96.

SCHLAF, J., RANDEN, T. & SØNNELAND, L. 2005. Introduction to seismic texture. *Mathematical methods and modelling in hydrocarbon exploration and production.* Springer.

SHANMUGAM, G. 2016. Submarine fans: a critical retrospective (1950–2015). *Journal of Palaeogeography,* 5**,** 110-184.

SHANMUGAM, G. & MOIOLA, R. 1988. Submarine fans: characteristics, models, classification, and reservoir potential. *Earth-Science Reviews,* 24**,** 383-428.

SIMM, R. & BACON, M. 2014. *Seismic Amplitude: An interpreter's handbook*, Cambridge University Press.

SOHN, Y. 1997. On traction-carpet sedimentation. *Journal of Sedimentary Research,* 67**,** 502-509.

SOUTTER, E. L., KANE, I. A., HODGSON, D. M. & FLINT, S. 2021. The concavity of submarine canyon longitudinal profiles. *Journal of Geophysical Research: Earth Surface,* 126**,** e2021JF006185.

SPYCHALA, Y. T., HODGSON, D. M., PRÉLAT, A., KANE, I. A., FLINT, S. S. & MOUNTNEY, N. P. 2017. Frontal and lateral submarine lobe fringes: comparing sedimentary facies, architecture and flow processes. *Journal of Sedimentary Research,* 87**,** 75-96.

STOW, D. A. & MAYALL, M. 2000. Deep-water sedimentary systems: New models for the 21st century. *Marine and Petroleum Geology,* 17**,** 125-135.

STRACHAN, L. J. 2008. Flow transformations in slumps: a case study from the Waitemata Basin, New Zealand. *Sedimentology,* 55**,** 1311-1332.

STRACHAN, L. J., RARITY, F., GAWTHORPE, R. L., WILSON, P., SHARP, I. & HODGETTS, D. 2013. Submarine slope processes in rift-margin basins, Miocene Suez Rift, Egypt. *Bulletin,* 125**,** 109-127.

TALLING, P. J., MASSON, D. G., SUMNER, E. J. & MALGESINI, G. 2012. Subaqueous sediment density flows: Depositional processes and deposit types. *Sedimentology,* 59**,** 1937-2003.

TEK, D. E., MCARTHUR, A. D., POYATOS-MORÉ, M., COLOMBERA, L., ALLEN, C., PATACCI, M. & MCCAFFREY, W. D. 2022. Controls on the architectural evolution of deep-water channel overbank sediment wave fields: insights from the Hikurangi Channel, offshore New Zealand. *New Zealand Journal of Geology and Geophysics,* 65**,** 141-178.

WALKER, R. G. 1978. Deep-water sandstone facies and ancient submarine fans: models for exploration for stratigraphic traps. *AAPG Bulletin,* 62**,** 932-966.

WALKER, R. G. 1992. Turbidites and submarine fans. *Facies Models, response to sea level change***,** 239-263.

WIDESS, M. 1973. How thin is a thin bed? *Geophysics,* 38**,** 1176-1180.